Sister Rod Destructive Examinations (FY23)

Appendix B: Segmentation, Defueling, Metallographic Data and Total Cladding Hydrogen

Spent Fuel and Waste Disposition

Prepared for
US Department of Energy

Spent Fuel and Waste Science and Technology

Oak Ridge National Laboratory
Rose Montgomery, Muhammet Ayanoglu, Tyson Jordan, Yadukrishnan Sasikumar, James T. Dixon, Stephanie M. Curlin, Jason Harp

January 31, 2024
M2SF-24OR010201024
ORNL/SPR-2023/3190

SUMMARY

This report documents work performed under the Spent Fuel and Waste Disposition's Spent Fuel and Waste Science and Technology program for the US Department of Energy (DOE) Office of Nuclear Energy (NE). This work was performed to fulfill Level 2 Milestone M2SF-24OR010201024, "FY23 ORNL Testing on Sibling Pins," within work package SF-24OR01020102 and is an update to the work reported in M2SF-23OR010201024, M2SF-22OR010201047, M2SF-21OR010201032, M2SF-19ORO010201026, and M2SF-19OR010201028.

As a part of the DOE-NE High Burnup Spent Fuel Data Project, Oak Ridge National Laboratory (ORNL) is performing destructive examinations (DEs) of high burnup (HBU) (>45 GWd/MTU) spent nuclear fuel (SNF) rods from the North Anna Nuclear Power Station operated by Dominion Energy. The SNF rods, called *sister rods* or *sibling rods* are all HBU and include four different kinds of fuel rod cladding: standard Zircaloy-4 (Zirc-4), low-tin (LT) Zirc-4, ZIRLO®, and M5®. The DEs are being conducted to obtain a baseline of the HBU rod's condition before dry storage and are focused on understanding overall SNF rod strength and durability. Both composite fuel and defueled cladding will be tested to derive material properties. Although the data generated can be used for multiple purposes, one primary goal for obtaining the post-irradiation examination data and associated measured mechanical properties is to support SNF dry storage licensing and relicensing activities by (1) addressing identified knowledge gaps and (2) enhancing the technical basis for post-storage transportation, handling, and subsequent disposition of the SNF.

This report documents the status of the ORNL Phase 1 DE activities related to:

- Rough segmentation (RS),
- Defueling (DEF)
- DE.02 optical microscopy (MET)
- DE.03, cladding total hydrogen measurements

for seven Phase 1 sister rods. This report also outlines the DE tasks performed and the data collected to date, as guided by the sister rod test plans.

Appendix B provides detailed information regarding defueling activities, metallographic imaging and measurements, and total cladding hydrogen measurements.

Table SB-1 provides the status of the DE activities discussed in this appendix.

Table SB-1. DE status.

Planned DE		Status	ORNL lead	Comments
RS	Rough segmentation	Complete	Morris / Burns	All rough segmentation is complete for Phase 1 rods
DEF	Defueling	In progress	Montgomery	The majority of the defueling is complete. Additional defueling of DE.02 and DE.03 specimens is being performed as needed.
DE.02	Optical microscopy (MET)	In progress	Sasikumar / Ayanoglu as supported by Jordan (fueled); Dixon / Curlin (defueled)	(FY21) Fueled and defueled specimens were prepared for MET views. The Phase 1 priority 1 specimens were cut, and specimen preparation / polishing began. Initial Cladding/pellet views and measurements were available for all Phase 1 rods. Specific features, including waterside oxide thickness, remaining cladding wall thickness, pellet-side oxide thickness, HBU rim, and cladding inner and outer diameters were measured. Where applicable, comparisons with nondestructive examinations were provided. Section views were inspected for hydride orientation, and radial hydrides are visible in the heat-treated M5-clad specimen and the ZIRLO-clad heat-treated specimen. There is a high hydride density in the heat-treated Zirc-4 specimen. The few radial hydrides are short. The baseline ZIRLO-clad specimen includes short radial hydrides. The other baseline specimens did not have radial hydrides. An axial MET was created at a pellet–pellet gap. Axial and radial METs do not show a change in the hydride precipitation density through the gap. A section of the cladding will be analyzed for total hydrogen content to determine whether the total cladding hydrogen content varies between the pelleted region and the pellet–pellet gap. (FY22) The remaining Phase 1 priority 1 elevations were imaged and measured. The use of an etchant on fueled specimens has been demonstrated and awaits approval by the facility. Previously mounted and polished METs will be etched and reimaged when the etchant is approved for use. **(FY23)** The use of an etchant on fueled specimens was approved by the IFEL, and several specimens have been repolished and etched. Discussions of these specimens have been integrated to Appendix B. The nucleation of cladding hydrides on pellet cracks was observed on several additional views, confirming the FY19 finding. This is an important

Planned DE		Status	ORNL lead	Comments
				detail to understand in the context of the overall effect of reoriented hydrides because much of the previous data are from specimens that were empty cladding.
DE.03	Cladding total hydrogen measurements	Complete	Sasikumar/ Ayanoglu / Harp	(FY21) Specimens were defueled and the equipment was set up. Out-of-cell verification testing of the oxygen nitrogen hydrogen analyzer is complete, and it has been installed in the Irradiated Fuels Examination Laboratory (IFEL) greenhouse in a separate enclosure. Of the 20 Phase 1 priority 1 planned measurements, 14 have been completed to date. (FY22) Except for 1, the remaining Phase 1 priority 1 cladding hydrogen measurements have been completed. **FY23**: A specimen from a rod location where a pellet-pellet gap had been observed was analyzed, with one specimen taken from the gap area, and three other specimens taken from locations where the pellet was present. Theory indicates that hydrogen in the cladding should migrate to the gap location because it was colder during operation in the reactor. MET views from the longitudinal specimen did not identify a higher density of hydride precipitates in the gap region. Cladding hydrogen measurements indicate a higher concentration just below the gap location.

This page is intentionally left blank.

ACKNOWLEDGMENTS

Many thanks to our US Department of Energy Office of Nuclear Energy sponsor Ned Larson, along with the Spent Fuel and Waste Science and Technology (SFWST) storage and transportation program leadership for their continued support. The sister rod project would not be possible without the vision and support of the Electric Power Research Institute, Westinghouse, Framatome, and Dominion Energy.

This work would not be possible without the support and expertise provided by the leadership and staff members of the Oak Ridge National Laboratory (ORNL) Irradiated Fuel Examination Laboratory (IFEL). Special thanks go to John Hinds and Brian Woody, the Building 3525 operators, and Tracy Binger and Mark Walls for their assistance with the defueling, cleaning, and irradiated material handling. Rick Henry has the unenviable task of tracking the bits and pieces of sister rods and their moves around the hot cell and to other facilities, and we very much appreciate his patience and continued support.

Many thanks to Tyler Smith and Lindsey Aloisi for their support on defueling the many small specimens required for total cladding hydrogen and metallographic studies. We also appreciate Tracy Binger's efforts measuring and tracking the defueled cladding radiation levels in support of releasing the specimens to ORNL's Low Activation Materials Development and Analysis (LAMDA) lab. Our appreciation and thanks are extended to the LAMDA lab staff for their continuing support on the sister rod metallography. We appreciate Martino Hooghkirk for his patience tracking the specimens, and for their wise advice and support deploying new equipment and processes at IFEL, we appreciate Jim Miller and Mark Delph.

This page is intentionally left blank.

CONTENTS

This page is intentionally left blank.

LIST OF FIGURES

This page is intentionally left blank.

LIST OF TABLES

This page is intentionally left blank.

REVISION HISTORY

Date	Changes
3/29/2019	Initial release
9/27/2019	Revised to include additional data and incorporate comments from the previously released report.
10/30/2020	Initial release of this appendix.
11/30/2020	The document numbering was revised to reflect its 2020 M2 status and the date was changed.
10/29/2021	Section B-4 was added.
3/31/2022	Comments received on the 10/29/2021 manuscript were incorporated throughout. The document numbering was revised to reflect its 2021 M2 status, and the date was changed.
10/28/2022 (internal draft not for public release)	Work completed in FY22 was included in the report, with additional data and revised figures included in Sections B-2, B-3, and B-4, including all their subsections.
1/13/2023	Comments received from the team were incorporated throughout and the document ID number was revised to reflect its M2 status and the issue date was changed.
10/31/2023 (internal draft not for public release)	Additional sections were imaged after etching and remeasured. The new images and measurements have been added in the appropriate sections.
1/31/2024	Comments received from the team were incorporated throughout and the document ID number was revised to reflect its M2 status and the issue date was changed.

This page is intentionally left blank.

ACRONYMS

CIRFT	Cyclic Integral Reversible Fatigue Tester
DE	destructive examination
DEF	defueling
DOE	US Department of Energy
EPRI	Electric Power Research Institute
FHT	full-length fuel rod heat treatment
FY	fiscal year
GTRF	grid-to-rod fretting
HBU	high burnup
HPU	hydrogen pickup
HPU	hydrogen pickup fraction
ID	inner diameter
IFEL	Irradiated Fuels Examination Laboratory
LAMDA	Low Activation Materials Development and Analysis
LT	low tin
LVDT	linear variable differential transducer
MET	metallography
NE	Office of Nuclear Energy
NDE	nondestructive examination
OD	outer diameter
ONH	oxygen nitrogen hydrogen
ORNL	Oak Ridge National Laboratory
PWR	pressurized water reactor
RPC	Research Project Cask
RS	rough segmentation
SFWST	Spent Fuel and Waste Science and Technology
SEM	scanning electron microscope
SNF	spent nuclear fuel
TEM	transmission electron microscope

This page is intentionally left blank

B-1. ROUGH SEGMENTATION (RS)

Seven Phase 1 rods [B-1,B-2,B-3] were segmented:

- 30AD05 (M5 clad)
- 30AE14 (M5 clad, heat-treated)
- 3D8E14 (ZIRLO clad)
- 3F9N05 (ZIRLO clad, heat-treated)
- F35P17 (Zirc-4 clad, heat-treated)
- 3A1F05 (LT Zirc-4 clad)
- 6U3K09 (ZIRLO clad)

A detailed cutting plan was developed [B-3], with test specimens allocated for the destructive examinations (DEs) as guided by the test plans [B-2,B-3] and the results of the nondestructive examination (NDE) [B-4]. Each segment was marked to indicate the upper elevation and was placed into a labeled storage capsule as it was being cut. The capsules are not backfilled with inert gas because these Phase 1 rod segments are expected to be used in testing within a few years. The rough segments are being further subdivided as needed for the slated DE.

This page is intentionally left blank.

B-2. DEFUELING (DEF)

Many segments will be defueled in the process of specimen preparation for DE. For example, all DE.03 specimens must be defueled before testing. DE.10 includes fueled and defueled specimens. In some cases, the removed fuel is the target of the test (e.g., DE.01 includes burnup measurements). The defueling processes vary depending on the follow-on tests to be performed. This section briefly describes defueling activities.

B-2.1 Defueling Cladding Segments for Argonne National Laboratory Shipment

Twelve rod cladding segments were selected from the Phase 1 sister rods for ring compression testing as listed in Table B-1. The segments were defueled by boiling them individually in an acid bath, and each piece of defueled cladding was weighed and packaged individually in an aluminum container. The dose rate was measured at contact and at 1 ft. The dose rates represent the hottest spots on the container. The exterior surfaces of the aluminum containers were decontaminated before they were loaded into the shipping container. The dose rate of a decontaminated empty aluminum container is expected to be <20 mR/hr. Figure B-1 shows the cladding segments in their aluminum containers awaiting shipment to Argonne National Laboratory and a dose rate measurement being taken on one sample in its aluminum container using a Ludlum 9-4 ion chamber.

To determine the isotopic inventory of any pellet materials that might have still been adhered to the interior wall of the cladding following this defueling process, one 18 mm rod segment was defueled using the same process, and then the resulting defueled cladding segment was dissolved and analyzed. The results of the analysis, tabulated in Table B-2, were used to determine the residual pellet material isotopic content of each cladding segment based on the segment's weight.

Shipment of the segments was completed in April 2019.

Table B-1. Defueled cladding specimens for shipment to Argonne National Laboratory.

Sister rod and elevation of segment	Aluminum canister weight (g)	Canister + clad weight (g)	Clad weight (g)	Gamma dose on contact (mR/h)	Gamma dose @ 30cm (mR/h)
30AD05-2429-2519-DE.10	10.18	19.20	9.02	1,800	70
30AD05-3259-3349-DE.10	9.97	19.04	9.07	1,800	70
30AE14-2694-2784-DE.10	10.19	19.55	9.36	2,300	100
30AE14-3309-3399-DE.10	10.39	19.76	9.37	1,800	70
3A1F05-2555-2645-DE.10	10.22	19.74	9.52	1,200	50
3A1F05-3015-3105-DE.10	10.41	19.79	9.38	1,000	40
3D8E14-2213-2303-DE.10	10.17	19.68	9.51	1,400	60
3D8E14-2565-2655-DE.10	10.16	19.74	9.58	1,400	60
3F9N05-2572-2662-DE.10	10.22	19.78	9.56	1,400	70
3F9N05-3241-3331-DE.10	10.02	19.60	9.58	1,200	50
F35P17-2555-2645-DE.10	10.16	19.42	9.26	1,200	40
F35P17-3069-3159-DE.10	10.14	19.91	9.77	1,000	40

Table B-2. Residual pellet materials after defueling on an activity per gram of cladding basis.

Isotope	Ci/g	Isotope	Ci/g	Isotope	Ci/g
^{60}Co	7.20E-06	^{237}Np	2.14E-10	^{242}Pu	4.81E-09
^{95}Zr	4.15E-06	^{234}U	3.70E-10	^{241}Am	2.85E-06
^{106}Ru	2.08E-05	^{235}U	3.87E-12	^{242m}Am	2.44E-08
^{125}Sb	1.27E-05	^{236}U	1.07E-10	^{243}Am	6.47E-08
^{134}Cs	1.58E-04	^{238}U	7.19E-11	^{244}Cm	1.04E-05
^{137}Cs	1.27E-03	^{238}Pu	3.53E-06	^{245}Cm	2.41E-09
^{144}Ce	4.15E-06	^{239}Pu	3.75E-07	^{246}Cm	9.61E-10
^{154}Eu	5.53E-05	^{240}Pu	5.33E-07	Beta *	3.708E-03
^{155}Eu	1.94E-05	^{241}Pu	0.000147		

* "Beta" is the remaining beta activity after subtracting known beta emitters and G-Alpha results from the liquid scintillation result. It is assumed to represent ^{90}Sr/^{90}Y.

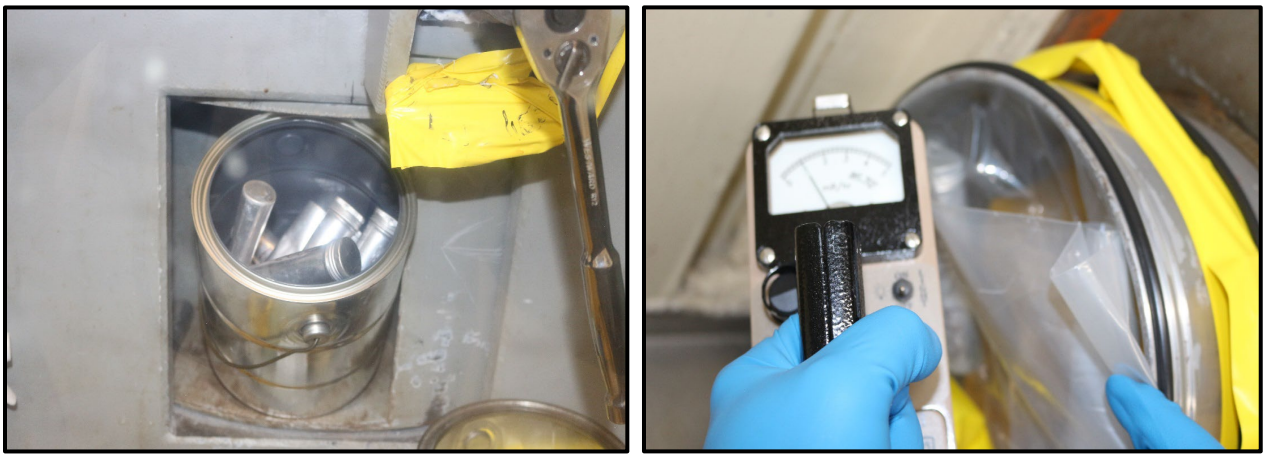

Figure B-1. Defueled cladding segments in aluminum containers awaiting shipment to Argonne (left) and contact dose rate measurement on a single container (right).

B-2.2 Defueling Cladding Segments to Prepare Total Cladding Hydrogen and Metallographic Specimens

To prepare specimens for total cladding hydrogen measurements (DE.03), the fuel is removed from the cladding. Also, some cladding-only metallographic (DE.02) specimens were produced. To remove the fuel from the cladding for these examinations, a dissolution column was constructed and installed in the IFEL hot cell in March 2019. The column, shown in Figure B-2, incorporates a recirculating acid loop to reduce the volume of waste generated and to reduce acid vapor released to the hot cell atmosphere. The design also includes a Soxhlet extractor that periodically flushes the dissolution acid bath from the chamber in which the cladding is held. This provides a supply of clean acid to remove as much fuel as possible. Figure B-2(a) shows a defueled specimen planned for metallographic imaging, and Figure B-2(b) shows the dissolution column in the ORNL hot cell. To date, 13 specimens have been defueled using the dissolution column.

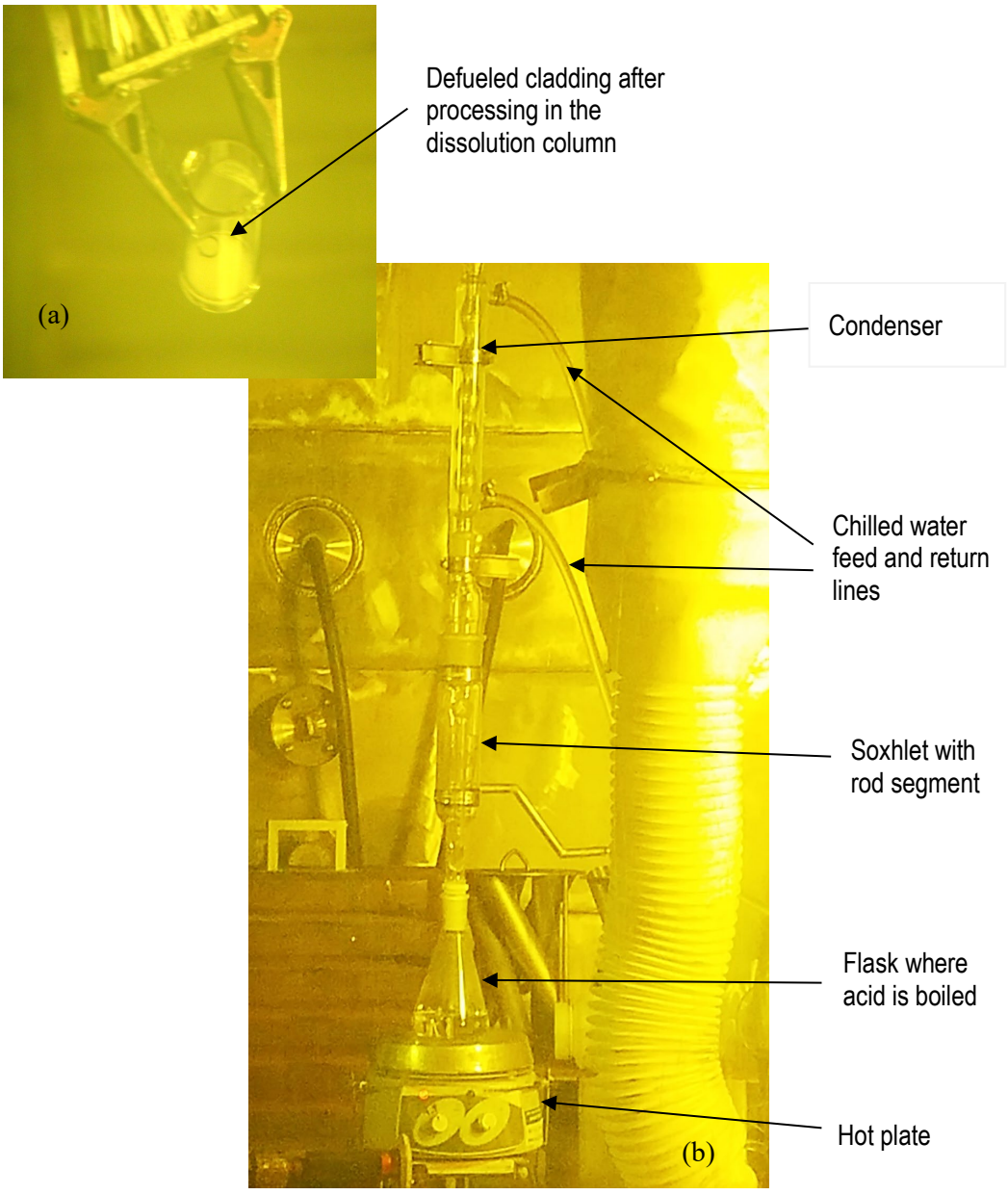

Figure B-2. (a) A Defueled specimen ready for DE.02 or DE.03 after several passes in (b) the dissolution column installed in the ORNL IFEL hot cell.

This page is intentionally left blank.

B-3. METALLOGRAPHY (DE.02)

The rough-cut DE.02 segments provide source material for several exams, including metallographic mounts (METs), total cladding hydrogen analysis, microhardness, scanning electron microscope (SEM) imaging, and transmission electron microscope (TEM) imaging. The first step in the DE.02 process is to cut appropriate specimens from the segments for each exam.

For METs, defueled and fueled views were prepared. The fueled views allow pellet features such as cracks and the high burnup (HBU) rim to be inspected, whereas the defueled views typically provide much cleaner, clearer views of the cladding with its hydrides and oxide layers. Figure B-3 provides examples of the typical features discussed within the METs. Not all features are visible in all views. For example, pellet cracks are only visible in fueled full-section METs, as shown in the upper right of Figure B-3. If a feature in the image is straight, then it is likely a polishing artifact or scratch. The waterside and pellet-side can usually be identified by the curvature of the cladding when the pellet is not present. The waterside oxide usually appears flat in cross-sectional METs, and the pellet-side oxide appears wavy in areas where the oxide has grown into the pellet. Cladding hydride precipitates are indicated either by dark lines (when defueled and etched) or white lines (in the fueled METs) and either follow the curvature of the cladding or are perpendicular to it. In fueled MET views, pellet porosity is visible as dark spots in the pellet region. For clarity, these typical features are not labeled in every MET: only atypical features are labeled where necessary.

Table B-3 summarizes the Phase 1 DE.02 segments and selected metallographic views, selected specimens for total cladding hydrogen measurements, and the current status of the exams. METs are available for all seven of the Phase 1 sister rods. Selected representative MET views are organized by cladding type in Sections B-3.1 through B-3.4. A summary of cladding thickness, waterside oxide thickness, pellet-side oxide thickness, and HBU rim measurements taken using the MET views is provided in Table B-4 by rod and elevation where available. The minimum remaining wall thickness measured using microscopy is 467 µm for F35P17, and the thickest waterside oxide thickness was 173 µm for the same rod, which also had extensive oxide spalling. In FY23, nine specimens were repolished and etched to obtain clearer images of the cladding hydrides. Additionally, one new specimen was polished and etched. Table B-4 has been updated, and the new images are included in the appropriate subsections.

The uncertainty of the microscopy measurements is related to the pixel resolution and to the ability of the analyst to visually select the points for measurement. For these measurements the uncertainty is estimated as ±3 µm. As noted in Table B-4, the data for each rod are taken from different elevations from the rod, and the use of burnup as a correlating parameter removes the expected differences in rod performance related to specimen elevation on the fuel rod. Most of the measured performance parameters are expected to vary azimuthally within the specimen (except for rod inner diameter [ID] and outer diameter [OD]), and the number of observations underlying the mean presented in Table B-4 range from 3 to 55 observations. For brevity, not all of the MET views and measurements are provided in this report. Although measurements are shown on some views, not all measurements taken are provided in the MET images selected for inclusion herein.

While the microscopy measurements are considered more accurate than the previously reported nondestructive measurements [B-4], a comparison of results from the two provides an independent check of the data and the NDE method uncertainty. Table B-5 provides a comparison of the NDE measurements and microscopy measurements. The rod OD was measured nondestructively using linear variable differential transducers (LVDTs), and the waterside oxide thickness and minimum remaining cladding wall thickness measurements were obtained using eddy current methods [B-4]. The LVDT-reported OD seems to be biased on the high side by ~0.5%. The eddy current measurements of remaining wall thickness seem to be biased ~4% on the high side for the M5- and ZIRLO-clad rods. For the Zirc-4 and LT-Zirc 4-clad rods, the difference ranges from -4 to +7.4%. As discussed in the NDE report [B-4], the waterside oxide

thickness varies around the circumference of the cladding. Generally, the maximum recorded MET measurements are comparable with the local average eddy current oxide thickness measurements except for the M5-clad rod measurements, which indicated oxide thickness in the lower ranges of detectability for the eddy current system used. Finally, it should also be noted that the MET measurement of the minimum oxide layer does not account for possible loss of oxide during sample preparation.

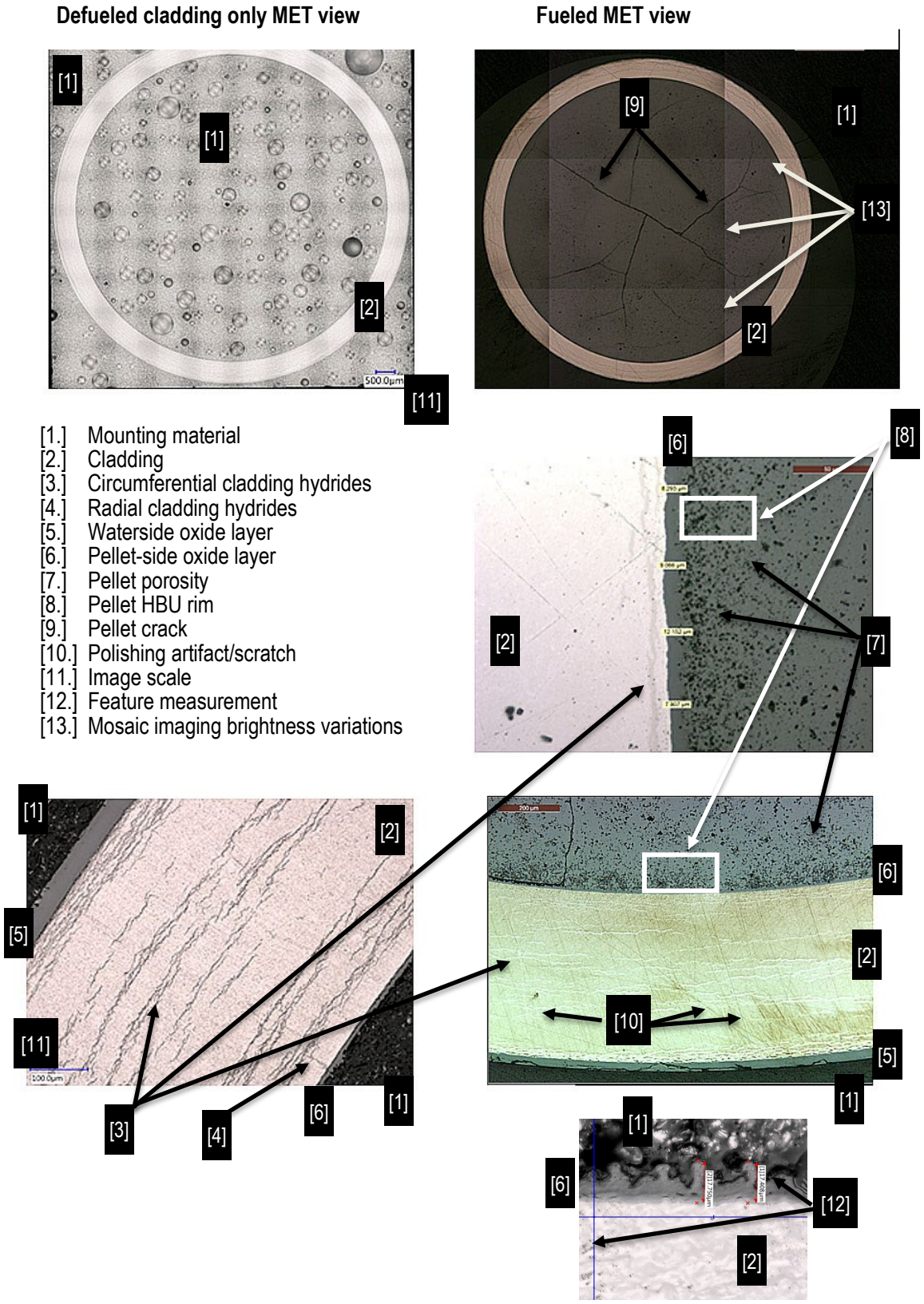

Figure B-3. Example of typical MET views and section features.

Table B-3. Phase 1 DE.02 parent segments with metallographic and total cladding hydrogen specimen selections and status.

Rod and originating segment elevation range (mm)			Fueled or defueled MET	Selection criteria	MET	Total cladding H_2
30AD05	678	697	TBD	Oxide thickness	Complete	N/A
30AD05	1,280	1,299	Fueled	Oxide thickness	Complete	Complete
30AD05	2,410	2,429	Defueled	HBU region with higher oxide	Complete	Complete
30AD05	2,783	2,802	Fueled	HBU region	✓	N/A
30AD05	3,240	3,259	Both	Highest oxide	Complete	Complete
30AE14	653	672	TBD	Oxide thickness	Complete	N/A
30AE14	1,677	1,696	Defueled	Oxide thickness	Complete	Complete
30AE14	2,203	2,222	Defueled	HBU at oxide peak	Complete	N/A
30AE14	2,675	2,694	Both	HBU at oxide peak	Complete	Complete
30AE14	3,399	3,418	Both	Highest oxide thickness	Complete	Complete
3A1F05	1,260	1,279	Fueled	Oxide thickness	Complete	N/A
3A1F05	1,585	1,604	Fueled	Oxide thickness	Complete	N/A
3A1F05	2,006	2,025	Defueled	Oxide thickness	Specimen mounted	Complete
3A1F05	2,383	2,402	Defueled	HBU with higher oxide thickness, spalling oxide, pellet banding	Complete	Complete
3A1F05	2,735	2,754	Both	High oxide thickness at HBU	Complete	Complete
3A1F05	3,105	3,124	Defueled	Peak oxide thickness	Complete	Complete
3D8E14	700	719	Fueled	Oxide thickness	Complete	N/A
3D8E14	1,178	1,331	Fueled	Fretting mark depth (post fatigue test)	✓	N/A
3D8E14	1,375	1,450	Fueled	Pellet-pellet gap and oxide thickness	Complete	Complete
3D8E14	2,303	2,322	Defueled	Oxide thickness	Complete	N/A
3D8E14	2,655	2,674	Defueled	HBU with oxide spike	Complete	Complete
3D8E14	3,206	3,225	Both	Highest oxide thickness	Fueled mounted/ defueled complete	Complete
3F9N05	700	719	Defueled	Oxide thickness	Complete	N/A
3F9N05	1,425	1,444	Defueled	Oxide thickness	Complete	Complete
3F9N05	2,300	2,329	Defueled	Oxide thickness	Complete	N/A
3F9N05	2,863	2,882	Defueled	HBU with higher oxide	Complete	Complete
3F9N05	3,331	3,350	Both	Peak oxide thickness and spalling oxide	Complete	Complete
6U3K09	2,616	2,635	Fueled	CIRFT correlating data	Complete	N/A
6U3K09	3,506	3,525	Fueled	CIRFT correlating data	Complete	N/A
F35P17	911	930	TBD	Oxide thickness	✓	N/A
F35P17	1,300	1,319	Defueled	Oxide thickness	Complete	Complete
F35P17	2,008	2,027	TBD	HBU with higher oxide thickness	✓	N/A
F35P17	2,383	2,402	Defueled	Oxide thickness, spalling oxide	Complete	N/A
F35P17	2,735	2,754	Both	Oxide thickness and spalling oxide	Complete	Complete
F35P17	3,050	3,069	Both	Peak oxide thickness and spalling oxide	Complete	Complete

✓ Planned but not yet started.

Table B-4. Summary of metallographic section measurements obtained to date.

The data provided within the table are based upon multiple measurements of the feature taken from the same metallographic image at different radial locations. Shaded cells indicate that no measurement is available for the specimen image at this time. An asterisk (*) indicates an average value based upon only 2 measurements of that feature from the image. Some features were also measured nondestructively as reported by Montgomery [B-4], and comparisons are provided in Table B-5. Some METs were imaged but not measured, and they are not included in this table.

Rod ID and original section elevations (mm)			Cladding type	Heat-treated rod?	Estimated local burnup (GWd/MTU)	Average measured cladding thickness	Maximum measured	Minimum measured	Average measured waterside oxide thickness	Maximum measured	Minimum measured	Average measured Pellet side oxide thickness	Maximum measured	Minimum measured	Average measured HBU rim thickness	Maximum measured	Minimum measured	Average measured rod Outer diameter	Maximum measured	Minimum measured	Average measured Cladding Inner diameter	Maximum measured	Minimum measured
						µm												mm					
30AD05	0678	0697	M5	no	58	545	551	540	5	8	4	9	11	6	70	87	54	9.415	9.431	9.403	8.283	8.300	8.268
30AD05	1280	1299	M5	no	59	545	549	541	4	7	2	9	12	6	84	132	51	9.470	9.488	9.446	8.358	8.368	8.339
30AD05	2410	2429	M5	no	59	558	573	546	28	41	20	11	26	6	72	111	48	9.446	9.462	9.432	8.247	8.279	8.230
30AD05	3240	3259	M5	no	55	543	558	535	11	15	3	11	16	7	62	89	43	9.389	9.416	9.374	8.279	8.288	8.273
30AE14	0653	0672	M5	yes	58	564	577	553	6	11	4	12	18	8	89	148	50						
30AE14	1677	1696	M5	yes	60	564	570	558	5	8	3	10	17	6	94	130	74	9.434	9.449	9.424	8.286	8.294	8.278
30AE14	2203	2222	M5	yes	60	561	566	551	9	14	5	8	15	4	106	145	66	9.440	9.466	9.400	8.292	8.296	8.287
30AE14	2675	2694	M5	yes	61	560	575	541	9	10	8	13	18	10				9.389	9.416	9.374	8.279*	8.288	8.273
30AE14	3399	3418	M5	yes	50	562	585	545	12	15	10	10	16	8	61	82	42	9.419	9.449	9.398	8.310	8.338	8.283
3D8E14	700	719	ZIRLO	no	62	569	584	552	7	17	2	9	19	3	90	117	60	9.507	9.521	9.499	8.342	8.359	8.329
3D8E14	1396	1403	ZIRLO	no	64	568	576	564	14	16	10	11	14	6	77	138	42	9.429	9.450	9.418	8.298	8.327	8.281
3D8E14	1403	1406	ZIRLO	no	64	568	577	557	12	12	12												
3D8E14	1406	1409	ZIRLO	no	64	569	580	559	15	16	14	11	17	7	79	110	52	9.471	9.496	9.430	8.326	8.338	8.313
3D8E14	2303	2322	ZIRLO	no	62	560	568	553	19	25	8	12	19	6	101	228	58	9.489	9.532	9.452	8.293	8.310	8.275
3D8E14	2655	2674	ZIRLO	no	64	549	564	531	34	41	31	15	18	12	70	108	52	9.466	9.495	9.424	8.330	8.344	8.306

Table B-4. Summary of metallographic section measurements obtained to date (continued).

Rod ID and original section elevations (mm)			Cladding type	Heat-treated rod?	Estimated local burnup (GWd/MTU)	µm												mm					
						Average measured cladding thickness	Maximum measured	Minimum measured	Average measured waterside oxide thickness	Maximum measured	Minimum measured	Average measured Pellet side oxide thickness	Maximum measured	Minimum measured	Average measured HBU rim thickness	Maximum measured	Minimum measured	Average measured rod Outer diameter	Maximum measured	Minimum measured	Average measured Cladding Inner diameter	Maximum measured	Minimum measured
3D8E14	3206	3225	ZIRLO	no	59	545	555	537	47	57	24	10	15	4				9.503	9.520	9.467	8.310	8.314	8.305
6U3K09	2616	2635	ZIRLO	no	58	560	571	549	21	22	19	9	12	6	59	107	36	9.440	9.455	9.425	8.276	8.302	8.249
6U3K09	3506	3525	ZIRLO	no	43	560	566	550	27	31	23	10	15	7				9.401	9.424	9.394	8.250	8.255	8.243
3F9N05	0700	0719	ZIRLO	yes	56	563	569	556	8	11	3	11	16	7	78	121	46	9.441	9.456	9.419	8.286	8.306	8.267
3F9N05	2300	2319	ZIRLO	yes	57	567	577	559	19	26	4	10	16	5	95	111	75	9.427	9.440	9.422	8.310	8.321	8.296
3F9N05	2863	2882	ZIRLO	yes	58	554	563	547	30	38	24	12	16	8				9.450*	9.450	9.449	8.277*	8.277	8.275
3F9N05	3331	3350	ZIRLO	yes	51	554	559	544	39	60	27	9	12	6	35	51	27	9.480*	9.496	9.464	8.271*	8.271	8.270
3A1F05	1260	1279	LT Zirc-4	no	56	560	565	555	15	18	14	10	12	7	54	74	43	9.436*	9.436	9.436	8.299*	8.299	8.299
3A1F05	1585	1604	LT Zirc-4	no	56	550	558	538	29	33	26	11	14	10	71	95	48	9.438	9.468	9.422	8.312	8.320	8.299
3A1F05	2383	2402	LT Zirc-4	no	55	530	547	518	70	89	52	10	16	6	74	105	46	9.461	9.483	9.435	8.290	8.300	8.285
3A1F05	2735	2754	LT Zirc-4	no	54	518	630	494	94	128	43	12	17	9	61	90	38	9.485*	9.548	9.421	8.290*	8.300	8.280
3A1F05	3105	3124	LT Zirc-4	no	53	517	523	508	75	98	27	10	16	6	85	100	70	9.489	9.532	9.452	8.293	8.310	8.275
F35P17	1300	1319	Zirc-4	yes	65	539	548	530	47	68	27	10	14	5	88	119	68	9.480	9.499	9.468	8.291	8.292	8.287
F35P17	2383	2402	Zirc-4	yes	66	492	505	479	47	146	8	11	15	7	78	95	65	9.367	9.521	9.283	8.282	8.288	8.269
F35P17	2735	2754	Zirc-4	yes	66	524	591	510	81	86	73	15	27	10	101	115	94	9.438	9.517	9.385	8.319	8.366	8.274
F35P17	3050	3069	Zirc-4	yes	65	485	503	466	93	173	8	14	29	7	165	198	137	9.391	9.631	9.304	8.335	8.360	8.316

Table B-5. Comparison of metallographic section measurements with nondestructive measurements.

Rod ID and original section elevations (mm)			NDE measured local OD using LVDT (mm)	MET measured average OD (mm)	Differential OD (LVDT – MET) (mm)	NDE measured local waterside oxide thickness (µm)	MET maximum measured oxide thickness (µm)	Differential waterside oxide thickness (NDE – MET) (µm)	NDE measured wall thickness (µm)	MET measured wall thickness (µm)	Differential wall thickness (NDE-MET) (µm)
30AD05	678	697	9.422	9.415	0.007	4	5	-1	574	545	29
30AD05	1280	1299	9.426	9.470	-0.044	3	4	-1	579	545	34
30AD05	2410	2429	9.436	9.446	-0.01	10	28	-18	582	558	24
30AD05	3,240	3,259	9.420	9.389	0.031	20	11	9	572	543	29
30AE14	1677	1696	9.460	9.434	0.026	7	5	2	581	564	17
30AE14	2203	2222	9.456	9.440	0.016	13	9	4	577	561	16
30AE14	2,675	2,694	9.459	9.389	0.07	16	9	7	576	560	16
30AE14	3,399	3,418	9.44	9.419	0.021	23	12	11	574	562	12
3D8E14	700	719	9.488	9.507	-0.019	9	7	2	576	569	7
3D8E14	1398	1403	9.482	9.429	0.053	14	16	-2	577	568	9
3D8E14	1403	1408	9.478	9.471	0.007	14	16	-2	577	569	8
3D8E14	2303	2322	9.487	9.489	-0.002	26	19	7	574	560	14
3D8E14	2,655	2,674	9.517	9.466	0.051	42	34	8	570	549	21
3D8E14	3206	3225	9.506	9.503	0.003	61	47	14	570	545	25
6U3K09	2,616	2,635	9.474	9.440	0.034	22	21	1	566	560	6
6U3K09	3506	3525	9.455	9.401	0.054	15	27	-12	560	560	0
3F9N05	700	719	9.463	9.441	0.022	3	8	-5	568	563	5
3F9N05	2300	2319	9.469	9.427	0.042	22	19	3	574	567	7
3F9N05	2,863	2,882	9.482	9.450	0.032	45	30	15	564	554	10
3F9N05	3,331	3,350	9.478	9.480	-0.002	60	39	21	560	554	6

Table B-5. Comparison of metallographic section measurements with nondestructive measurements (continued).

Rod ID and original section elevations (mm)			NDE measured local OD using LVDT (mm)	MET measured average OD (mm)	Differential OD (LVDT – MET) (mm)	NDE measured local waterside oxide thickness (µm)	MET maximum measured oxide thickness (µm)	Differential waterside oxide thickness (NDE – MET) (µm)	NDE measured wall thickness (µm)	MET measured wall thickness (µm)	Differential wall thickness (NDE-MET) (µm)
3A1F05	1,260	1,279	9.475	9.436	0.039	21	15	6	541	560	-19
3A1F05	1585	1604	9.461	9.438	0.023	39	29	10	537	550	-13
3A1F05	2383	2402	9.497	9.461	0.036	88	70	18	462	530	-68
3A1F05	2,735	2,754	9.564	9.485	0.079	137	94	43	548	518	30
3A1F05	3105	3124	9.521	9.489	0.032	133	75	58	518	517	1
F35P17	1300	1319	9.501	9.480	0.021	41	47	-6	527	539	-12
F35P17	2383	2402	9.544	9.367	0.177	115	47	68	501	492	9
F35P17	2,735	2,754	9.549	9.438	0.111	88	81	7	503	524	-21
F35P17	3050	3069	9.590	9.391	0.199	149	93	56	490	485	5

B-3.1 Fueled Specimen Etching

In order to improve the contrast of the precipitated hydrides in the fueled microscopy images, over the past 2 years, ORNL has been working to gain facility approval for the use of a hydrofluoric acid (HF) etchant. While the etchant is a standard for use with defueled cladding, there were concerns about the contamination levels of the used etchant and its route for disposal. In September 2022, the first fueled METs were etched.

Prior to etching in the hot cell, the necessary materials are prepared for the task as shown in Figure B-4. For this purpose, two glass beakers for distilled water (20 mL) and isopropyl alcohol were placed into a wide 15"×12"×3" size plastic tray which were all used for rinsing.

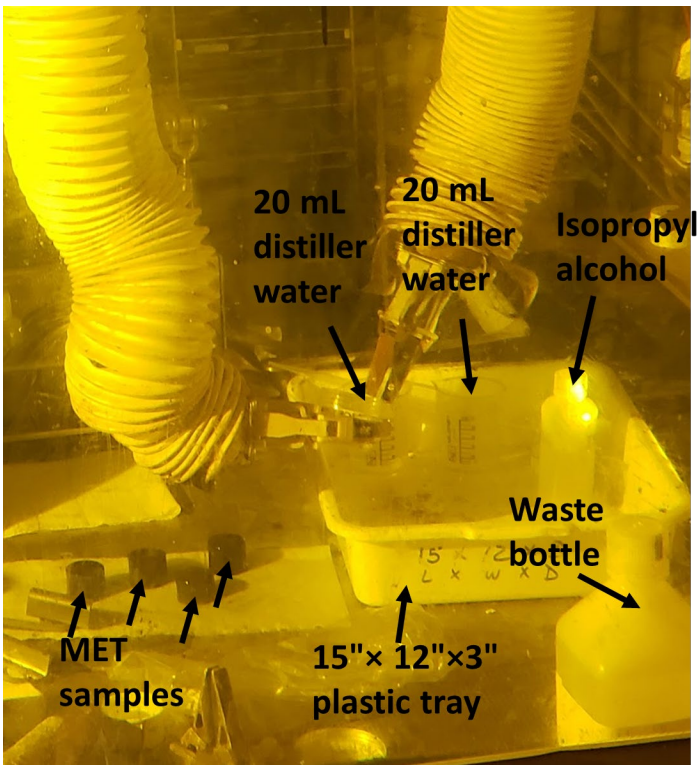

Figure B-4 Photograph showing the hot cell preparation prior to etching.

The etchant mixture containing nitric and hydrofluoric acids was prepared in a fume hood and then loaded into a pre-labeled 20 mL wide-mouth plastic bottle, which was further packaged in an aluminum can and bagged, as illustrated in Figure B-5, for transfer to the hot cell.

Prior to etching, the MET specimens were repolished for 2–4 min. to remove any stain or residue on the surface, rinsed with distilled water, and dried with a lint-free tissue paper. Then the polished face of the specimen mount was immersed into the etchant mixture for approximately 10 s; the time required for etching is dependent on the strength of the acids used and the item being etched, and it is an iterative process requiring experience with the materials. The etched surface of the specimen was then rinsed by immersion into the first and second beakers of distilled water, followed by a final rinse with alcohol. The specimen mounts were dried with a lint-free tissue paper or lens cleaning paper and transferred to the optical microscopy for inspection.

If the specimen is under-etched, which often results in a poor contrast of the hydrides, then etching is repeated. If the specimen is over-etched, then the metal surface is damaged, and an exaggerated hydride thickness is produced, so the specimen must be repolished, and the entire etching process must be repeated.

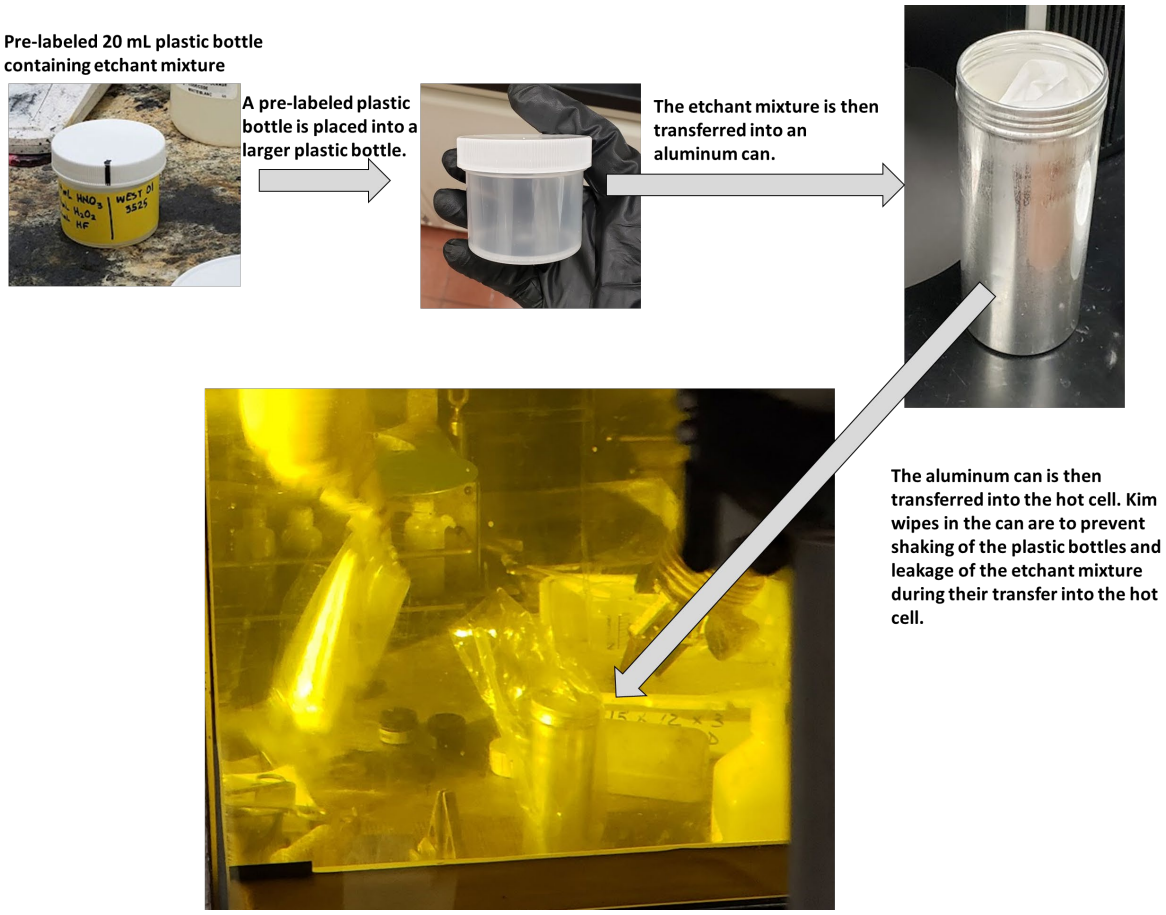

Figure B-5 Photos showing a pre-labeled plastic bottle containing etchant mixture and its transfer to the hot cell.

The etching recipe and procedure were initially demonstrated on a defueled cladding F35P17-2383-2402 in the hot cell. The purpose of etching of a defueled cladding is to collect ORNL waste stream process knowledge data from the etchant waste as a part of the data quality objectives (DQOs) to ensure that the associated waste stream is properly characterized for treatment and/or disposal.

Figure B-6 shows a series of micrographs captured from the F35P17-2383-2402 defueled cladding specimen before and after etching. Hydrides are clearly visible, with a dark contrast after etching. After etching of the defueled cladding MET specimen was completed, a liquid sample from the etchant waste was sent to ORNL's Radioactive Materials Analytical Laboratory for isotopic and activity analysis. The activity level was reported to be low enough to proceed with the fueled MET specimens etching.

Three fueled MET specimens were then etched, including baseline ZIRLO-clad specimens 3D8E14-0700-0719 and 3D8E14-2302-2322 and heat-treated Zirc-4-clad specimen F35P17-2383-2402. Optical microscope images shown in Figure B-6 through Figure B-10 show MET specimens before and after etching. Despite the nitric acid in the etchant mixture, the fuel pellets are undamaged, which is as expected when considering the short immersion time. Although a careful inspection can discern the hydrides in the

unetched images, the better contrast afforded by the etchant greatly enhances the ability to view the hydrides, and once final facility approval is granted, ORNL plans to etch and reimage all previous mounts.

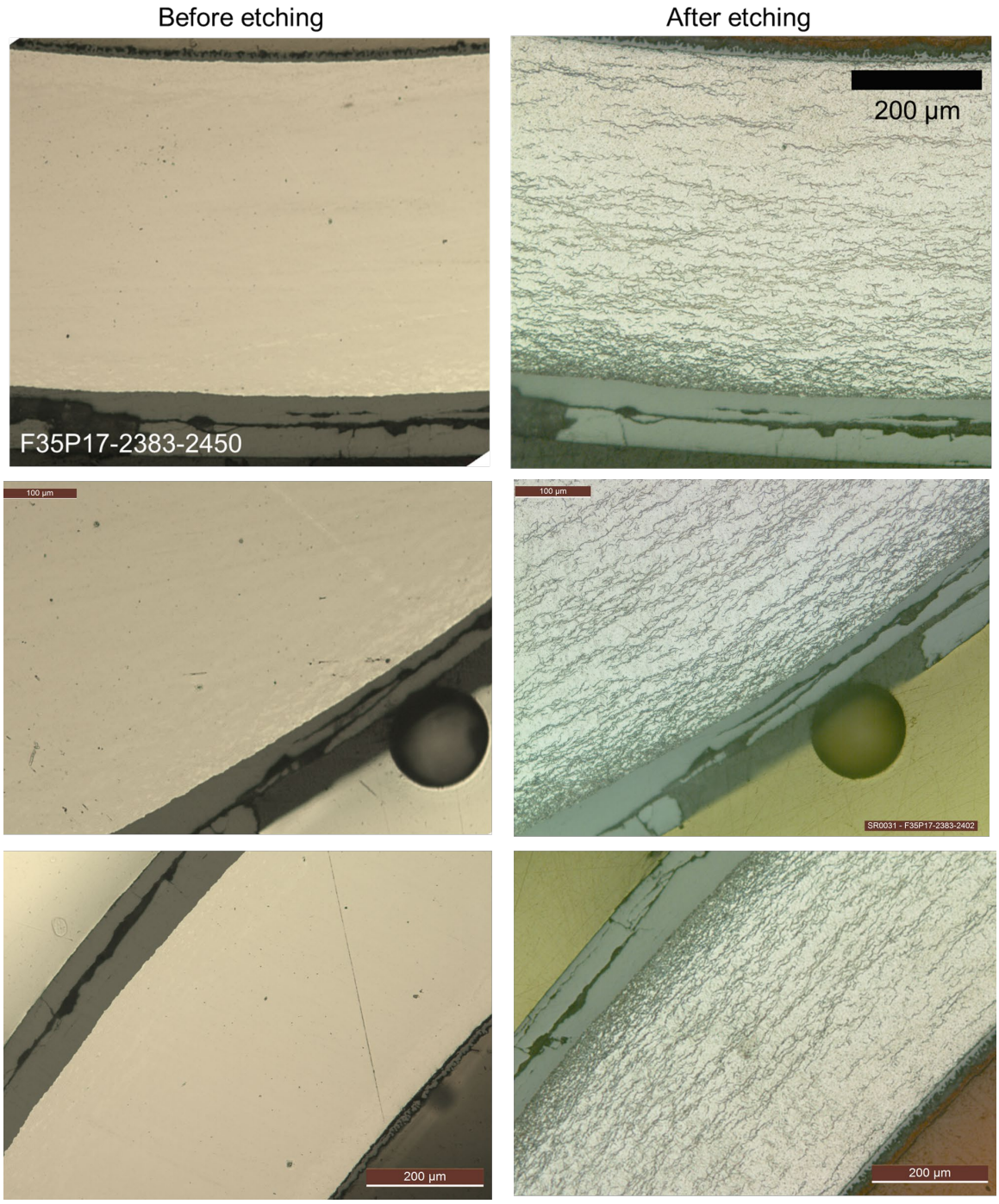

Figure B-6. Optical microscopy images showing F35P17-2383-2402 (defueled and heat-treated cladding) MET before and after etching.

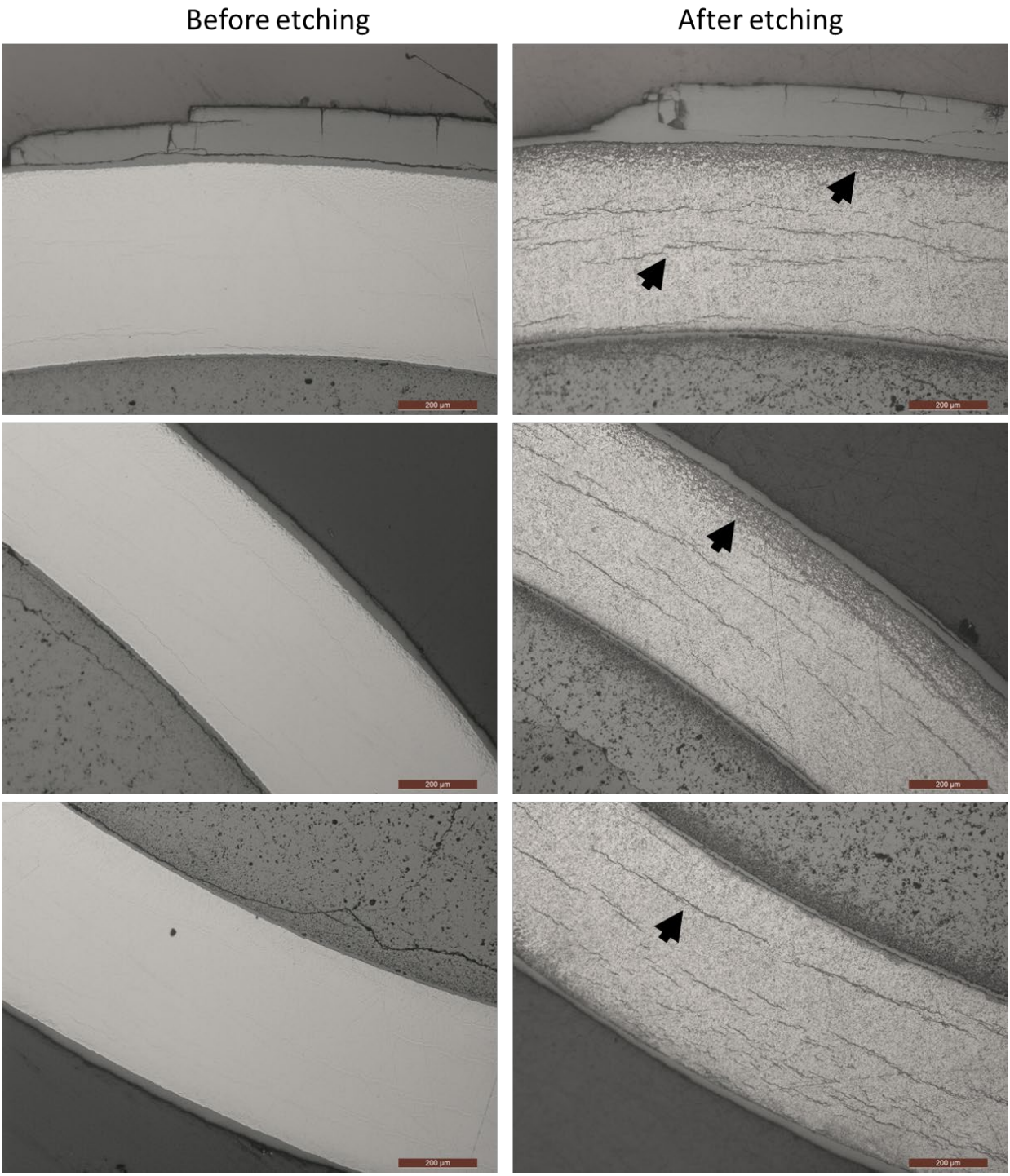

Figure B-7. Optical microscopy images showing F35P17-2383-2402 MET images (fueled and heat-treated) before and after etching (scale bar=200 µm). Some of the small hydrides that appeared after etching are highlighted with black arrows.

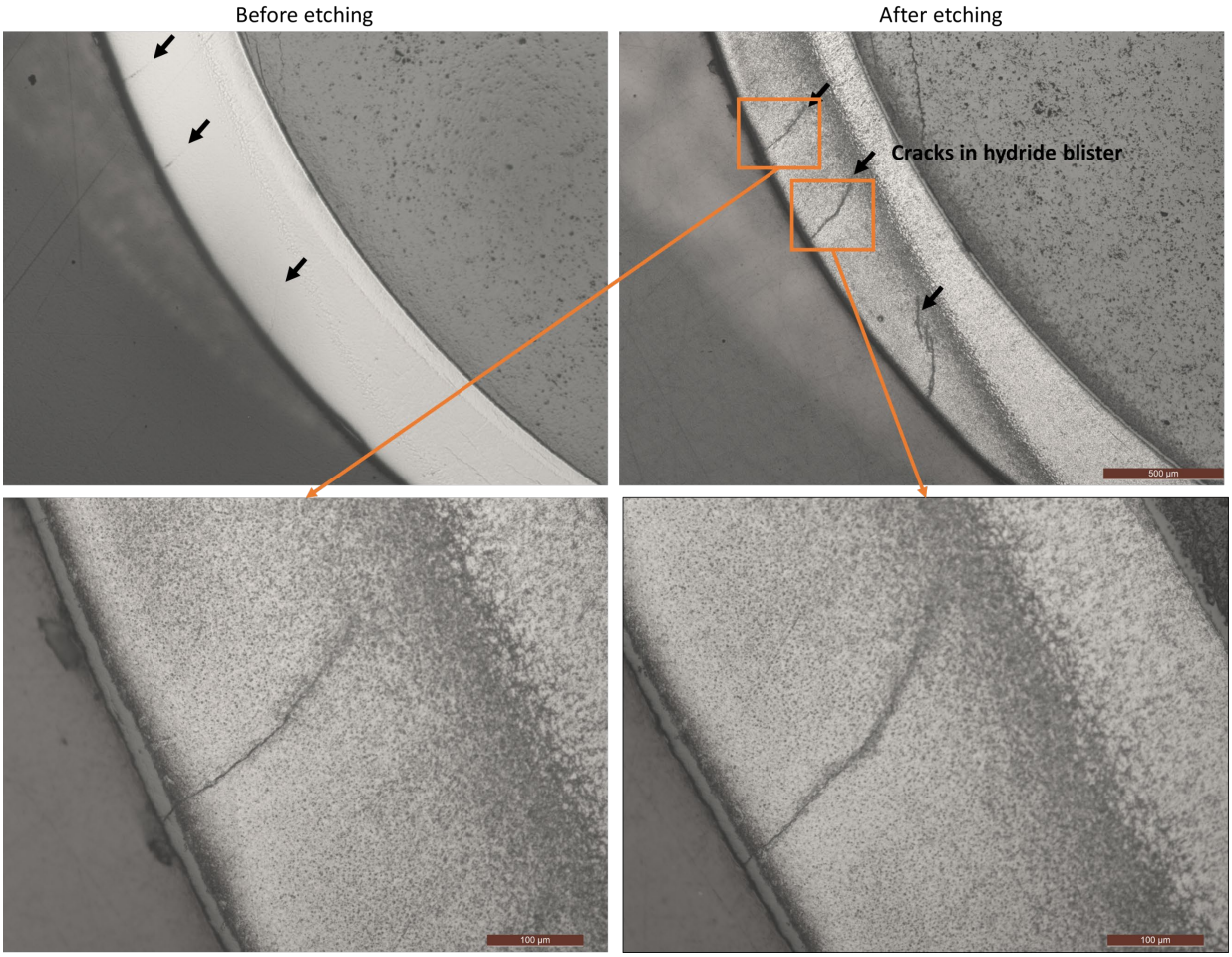

Figure B-8. Optical micrographs showing hydride blister location before and after etching. Cracks were found in the hydride blister after etching.

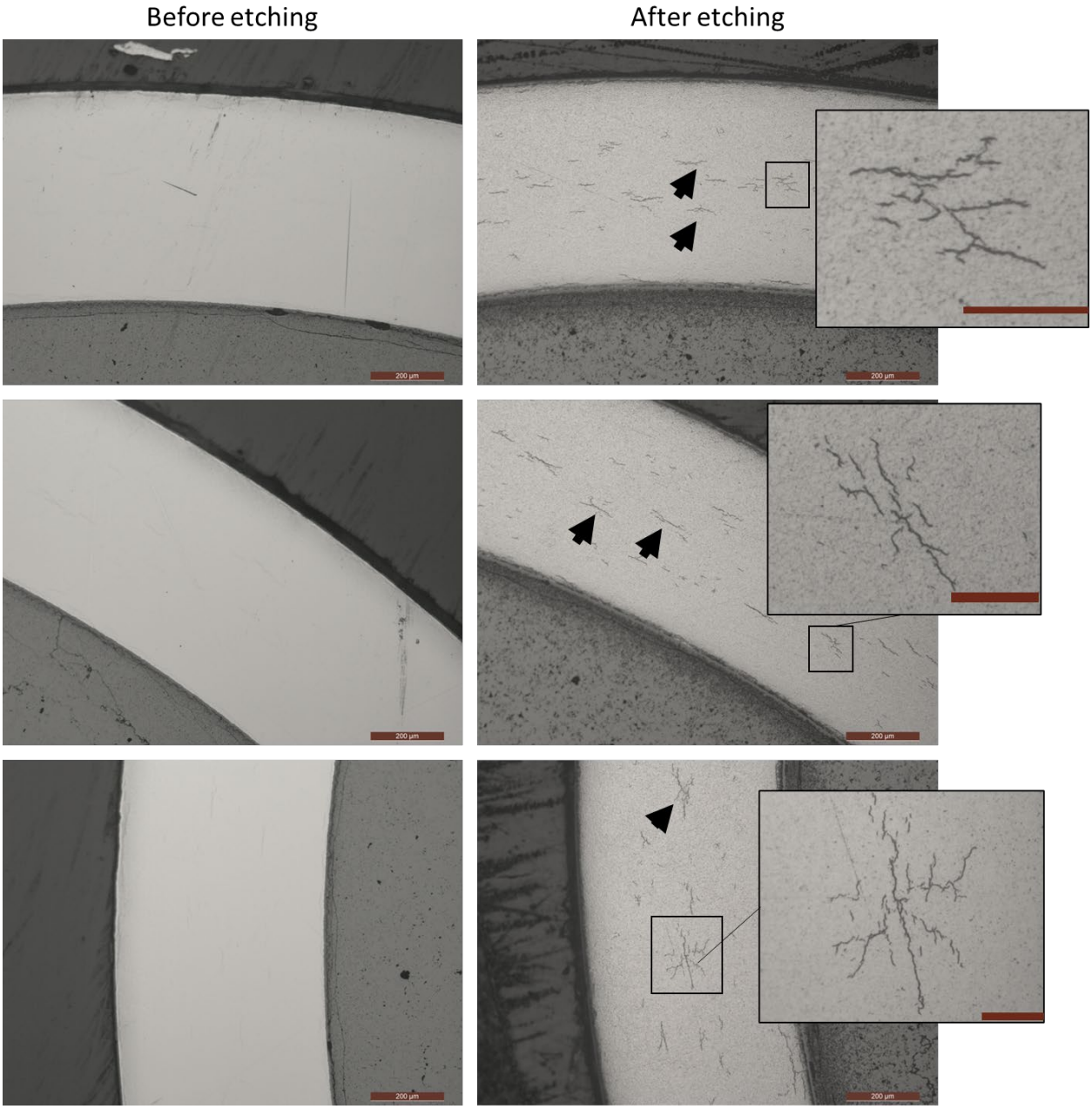

Figure B-9. Optical microscopy images showing 3D8E14-0700-0719 MET images (fueled and baseline cladding) before and after etching (scale bar=200 µm). Some of the small hydrides that appeared after etching are highlighted with the black arrows and magnified for better visibility (scale bar of the magnified images=50 µm).

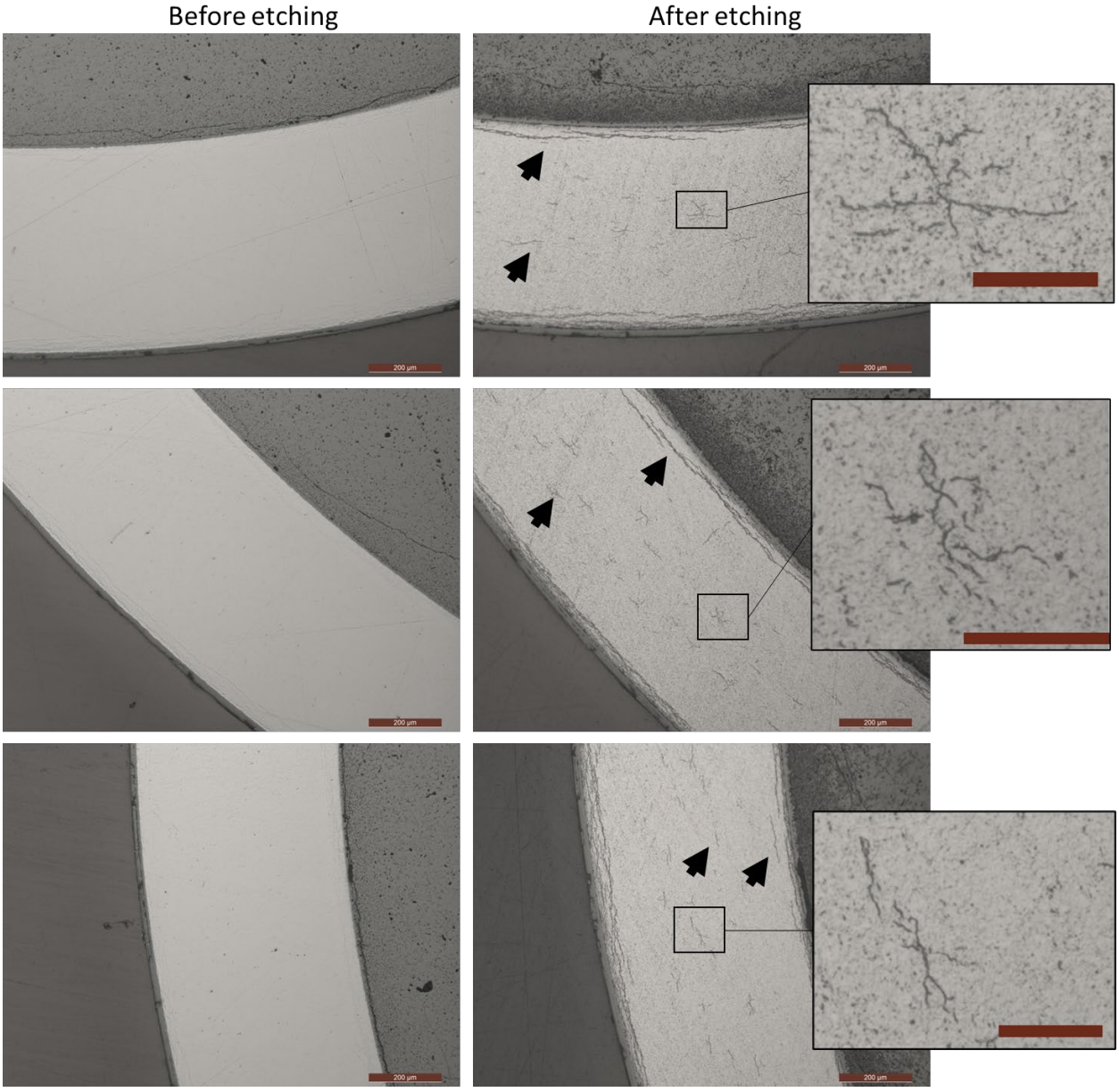

Figure B-10. Optical microscopy images showing 3D8E14-2302-2322 MET images (fueled and baseline cladding) before and after etching (scale bar=200 µm). Some of the small hydrides that appeared after etching are highlighted with the black arrows and magnified for better visibility (scale bar of the magnified images=50 µm).

B-3.2 M5-Clad Sister Rods

Several MET views from ten elevations are currently available for the two Phase 1 M5-clad sister rods—30AD05 (as received baseline condition), and 30AE14 (full-length rod heat treatment (FHT) applied), as shown in Figure B-10 through Figure B-26. Rods 30AD05 and 30AE14 provide a good comparison because (1) they were from the same fuel assembly, (2) they were manufactured at the same time by the same fuel vendor, (3) they had the same irradiation history, and (4) they are only 5 GWd/MTU different in average burnup at the elevations examined.

In both baseline and heat-treated M5-clad rods, hydride density increased with increasing axial elevation. Based on the available views, the precipitated hydrides in the baseline M5-clad rod (30AD05) are homogeneously distributed through the thickness of the cladding and are oriented circumferentially. The pellet is cracked radially (as expected) with no missing pellet surface. The depth of the pellet HBU rim is 62 μm on average for the baseline rod (3,240–3,259 mm in elevation).

For the heat-treated M5-clad rod (30AE14), many radial hydrides are visible, particularly at the ID of the cladding. The radial hydrides appear to have preferentially precipitated at locations where a pellet crack exists at the cladding ID, as illustrated in Figure B-26's colorized view. The cladding is not supported by the pellet at the pellet crack, and this results in a higher local stress concentration. The higher stress field provides a preferential location for hydride precipitation. Nucleation of a hydride near a pellet crack seems to be more likely if the ID cladding oxide layer is also cracked. The pellet cracks are as expected, with no missing pellet surface.

Neither baseline nor heat-treated M5 cladding showed any indication of gross oxide spalling or peeling at any axial location. The oxide thickness was uniform, especially at relatively low axial elevations (Figure B-11 and Figure B-20). The depth of the pellet HBU rim in the baseline and heat-treated cladding were similar and varied between ~62–84 μm on average and ~61–106 μm on average, respectively. Because the estimated local burnup of the samples is similar, the difference in the measured HBU rim thickness is likely a result of measurement uncertainty related to finding the ID of the HBU rim.

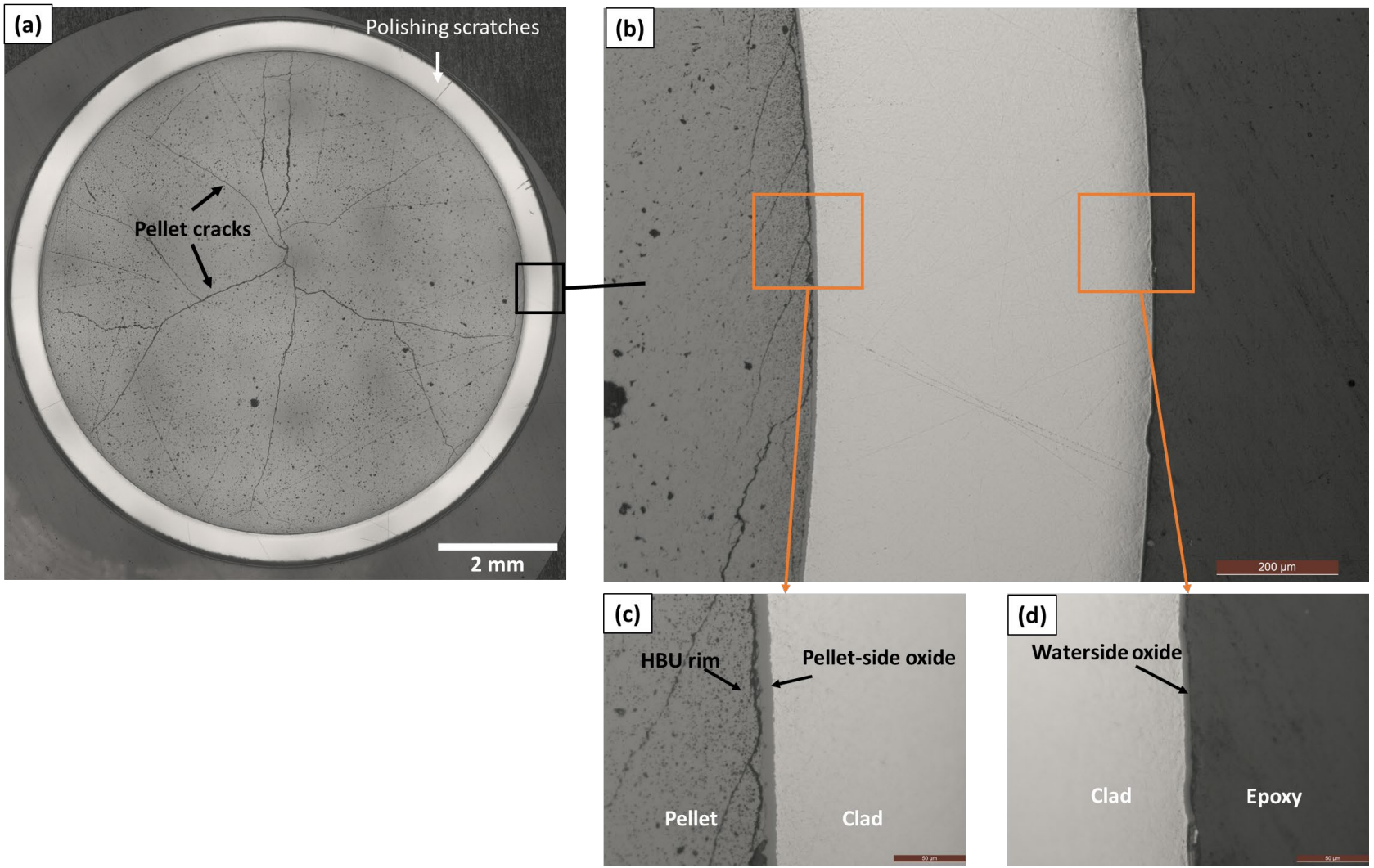

Figure B-11. Views of 30AD05-0678-0697 (fueled and unetched baseline rod): (a) overall cross-section showing pellet crack morphology, (b) magnified image of the right quarter showing small cladding circumferential hydrides (contrasted for better visibility) (scale bar=200 µm), (c)) pellet-side oxide and HBU rim (scale bar=50 µm), and (d) waterside oxide layer (scale bar=50 µm).

Figure B-12. Additional views of 30AD05-0678-0697 after etching. Almost no hydrides are visible.

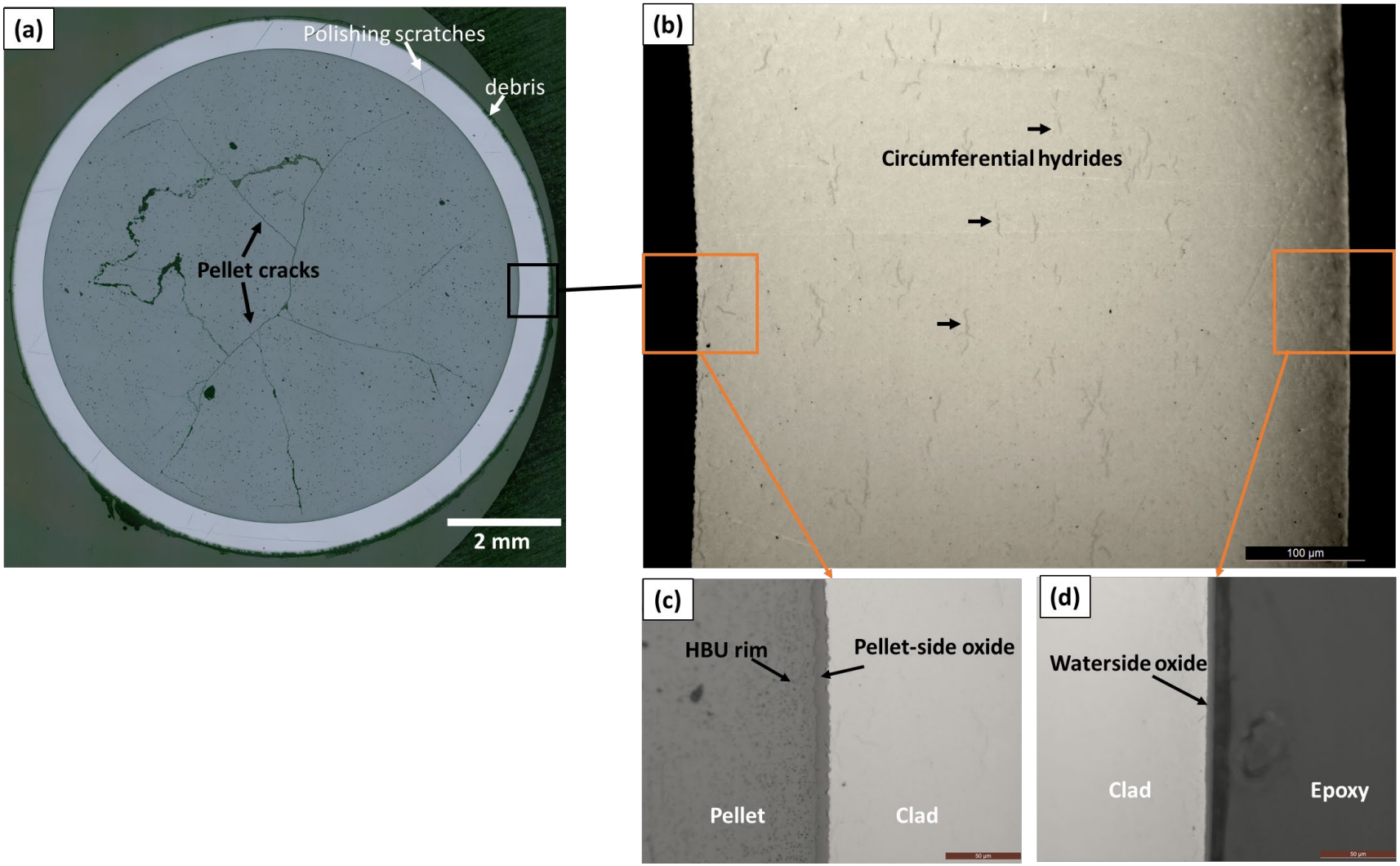

Figure B-13. Views of 30AD05-1280-1299 (fueled and unetched baseline rod): (a) overall cross-section showing pellet crack morphology, (b) magnified image of the right quarter showing small cladding circumferential hydrides (contrasted for better visibility) (scale bar=100 µm), (c)) pellet-side oxide and HBU rim (scale bar=50 µm), and (d) waterside oxide layer (scale bar=50 µm).

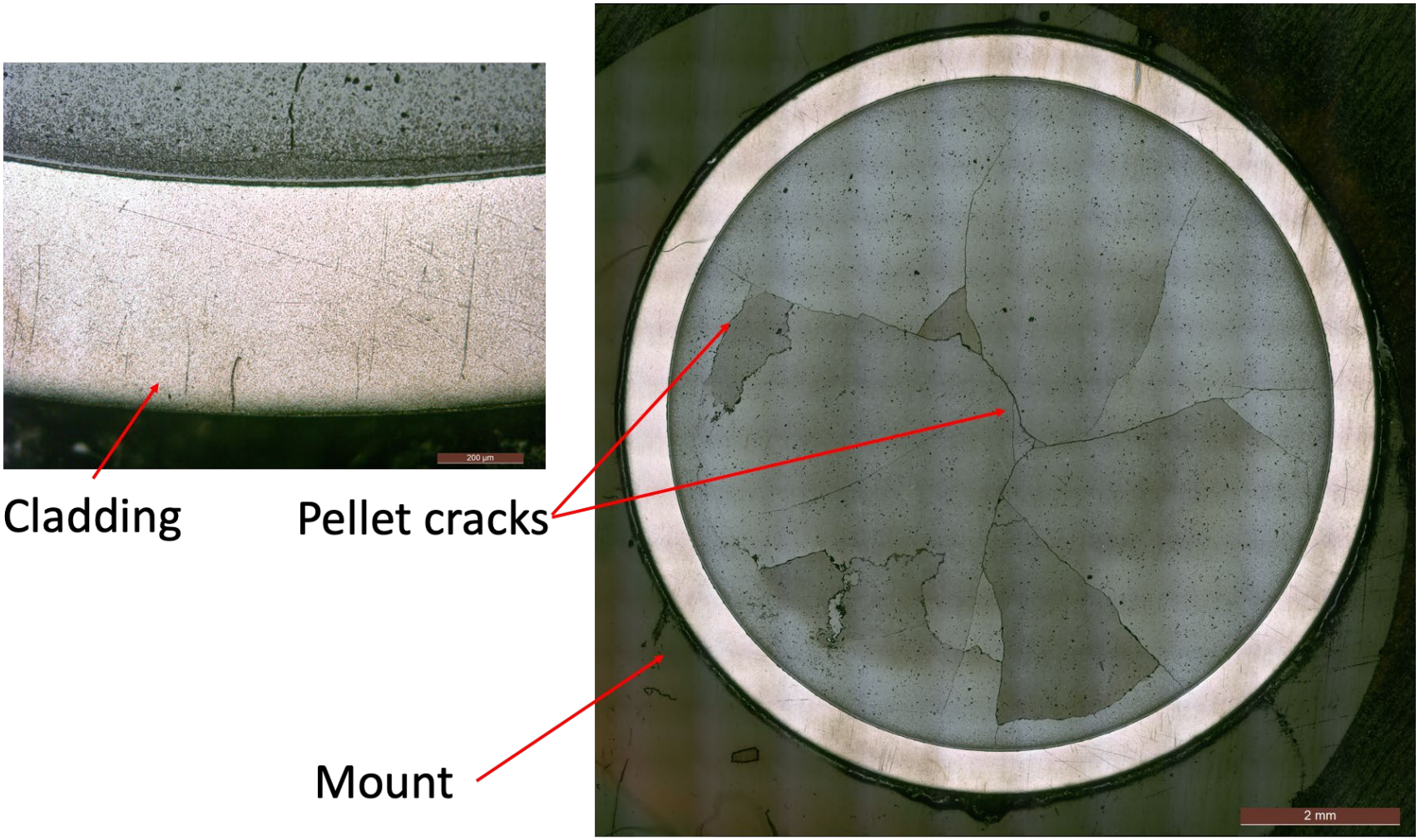

Figure B-14. 30AD05-1280-1299 after etching. Despite repeated polish and etch, no hydrides were contrasted.

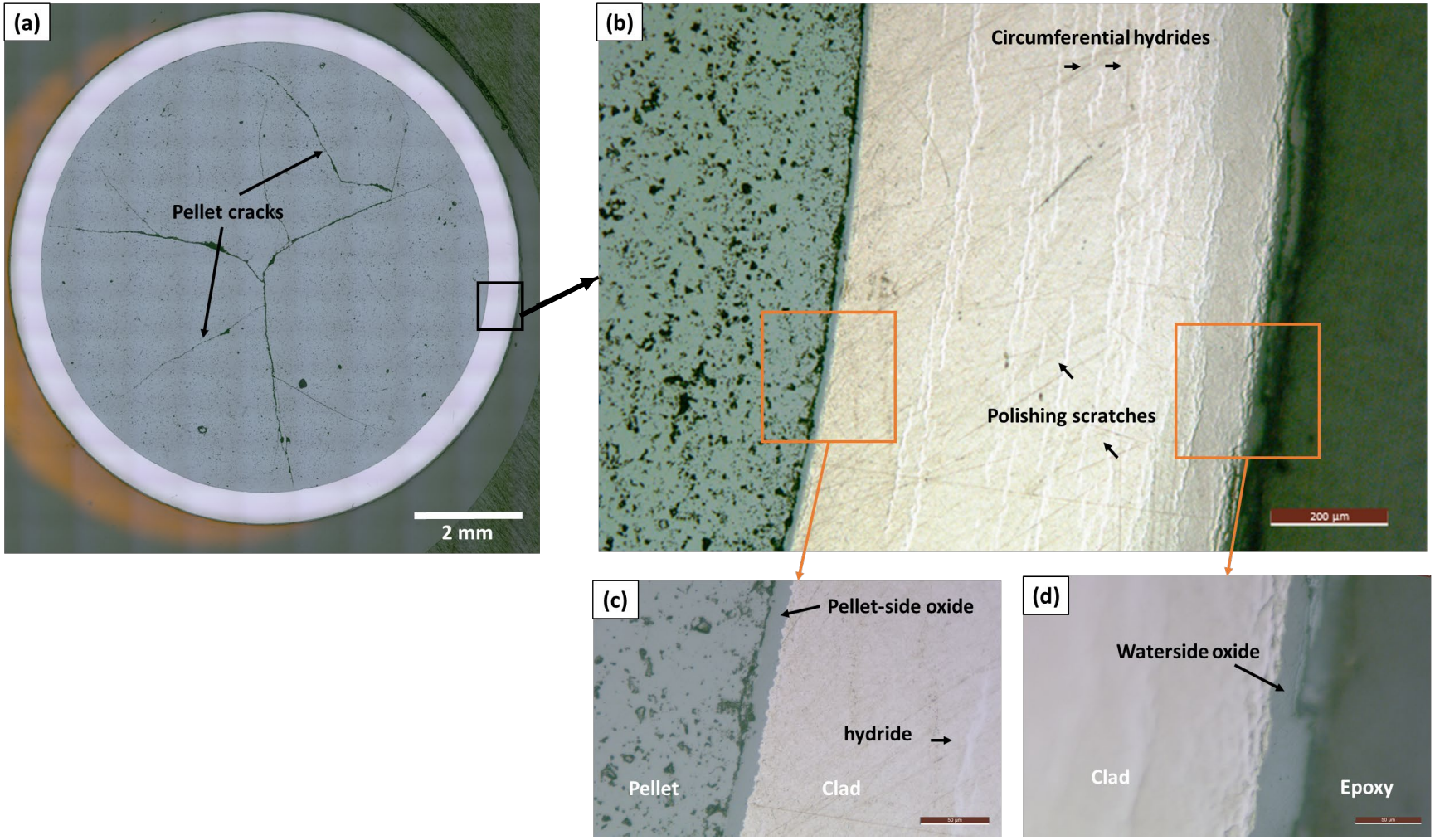

Figure B-15. Views of 30AD05-2410-2429 (fueled and unetched baseline rod): (a) overall cross-section showing pellet crack morphology, (b) magnified image of the right quarter showing circumferential hydrides (scale bar=200 µm), (c) pellet-side oxide (scale bar=50 µm), (d) and waterside oxide layer (scale bar=50 µm).

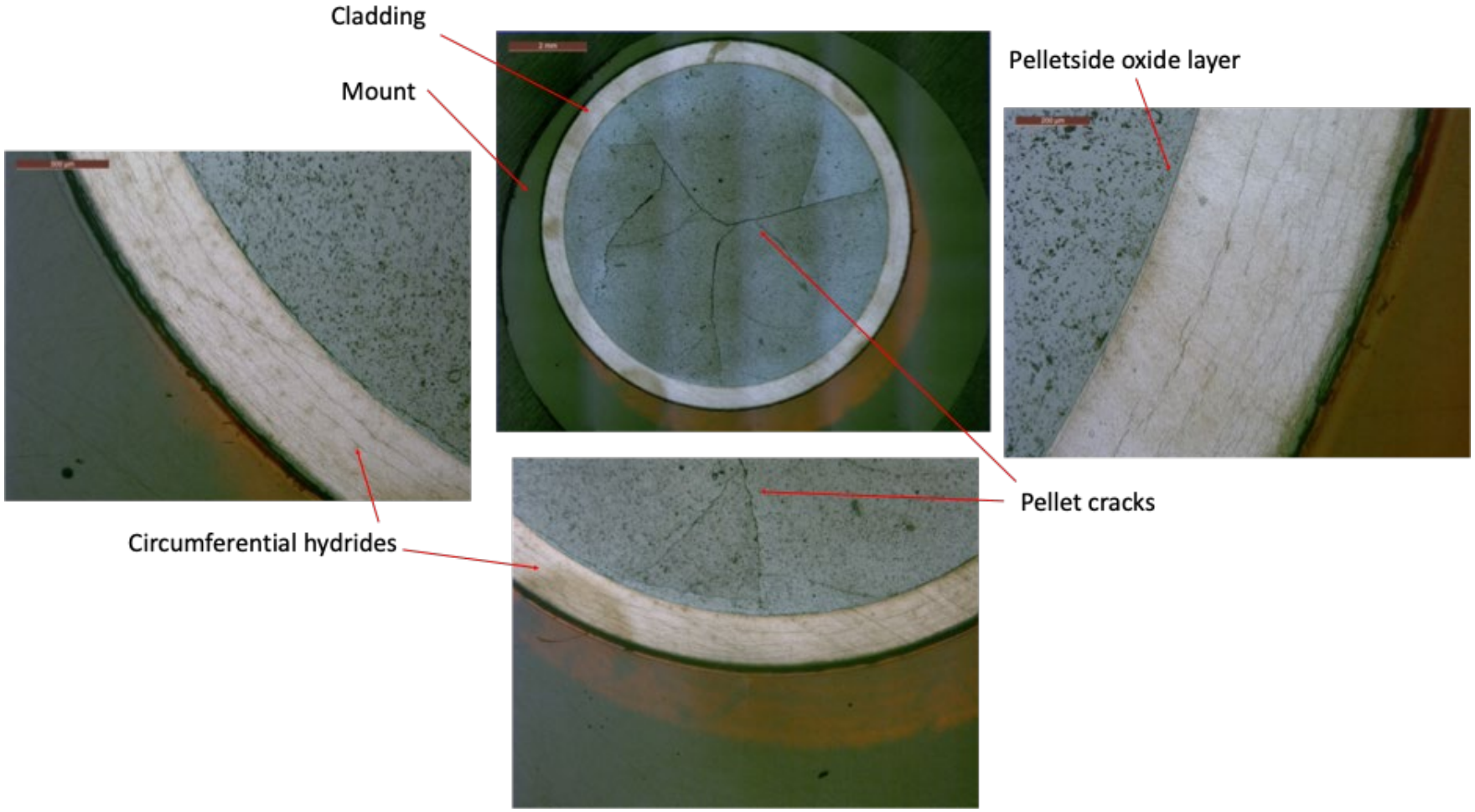

Figure B-16. Additional views of 30AD05-2410-2429 after etching.

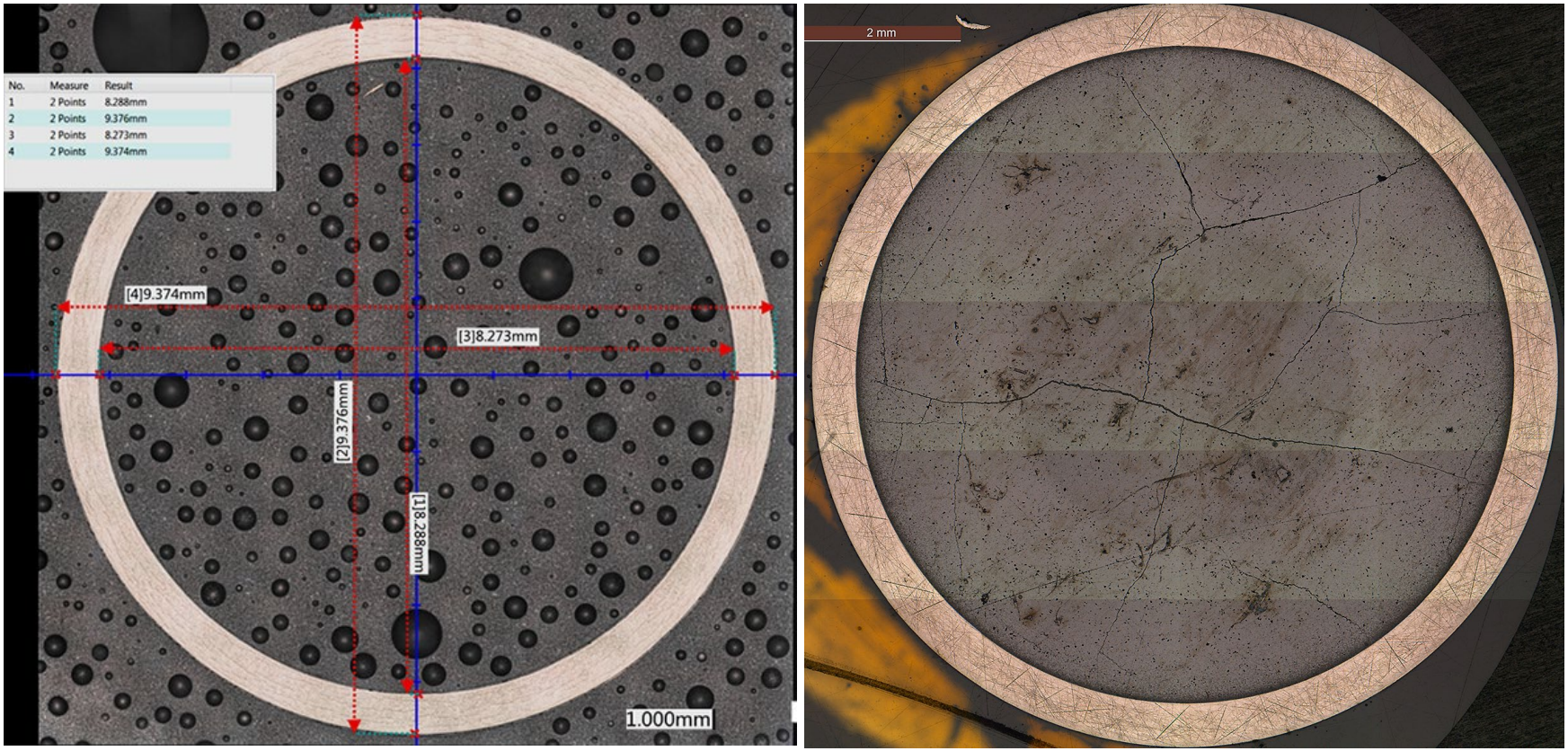

Figure B-17. Fueled (right) and defueled (left) overall section views, 30AD05-3240-3259 (baseline rod).

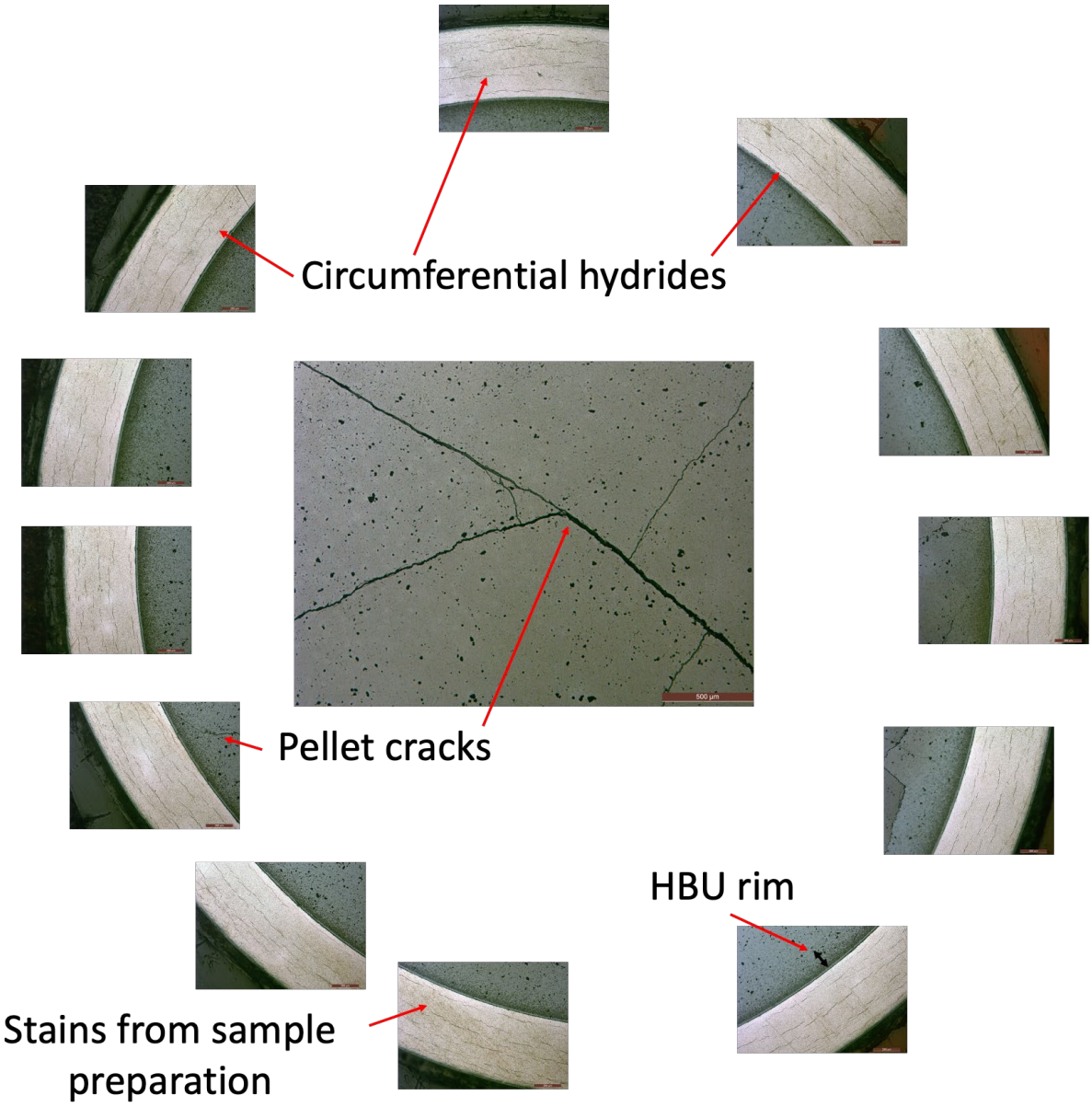

Figure B-18. Additional views of 30AD05-3240-3259 after etching (baseline rod).

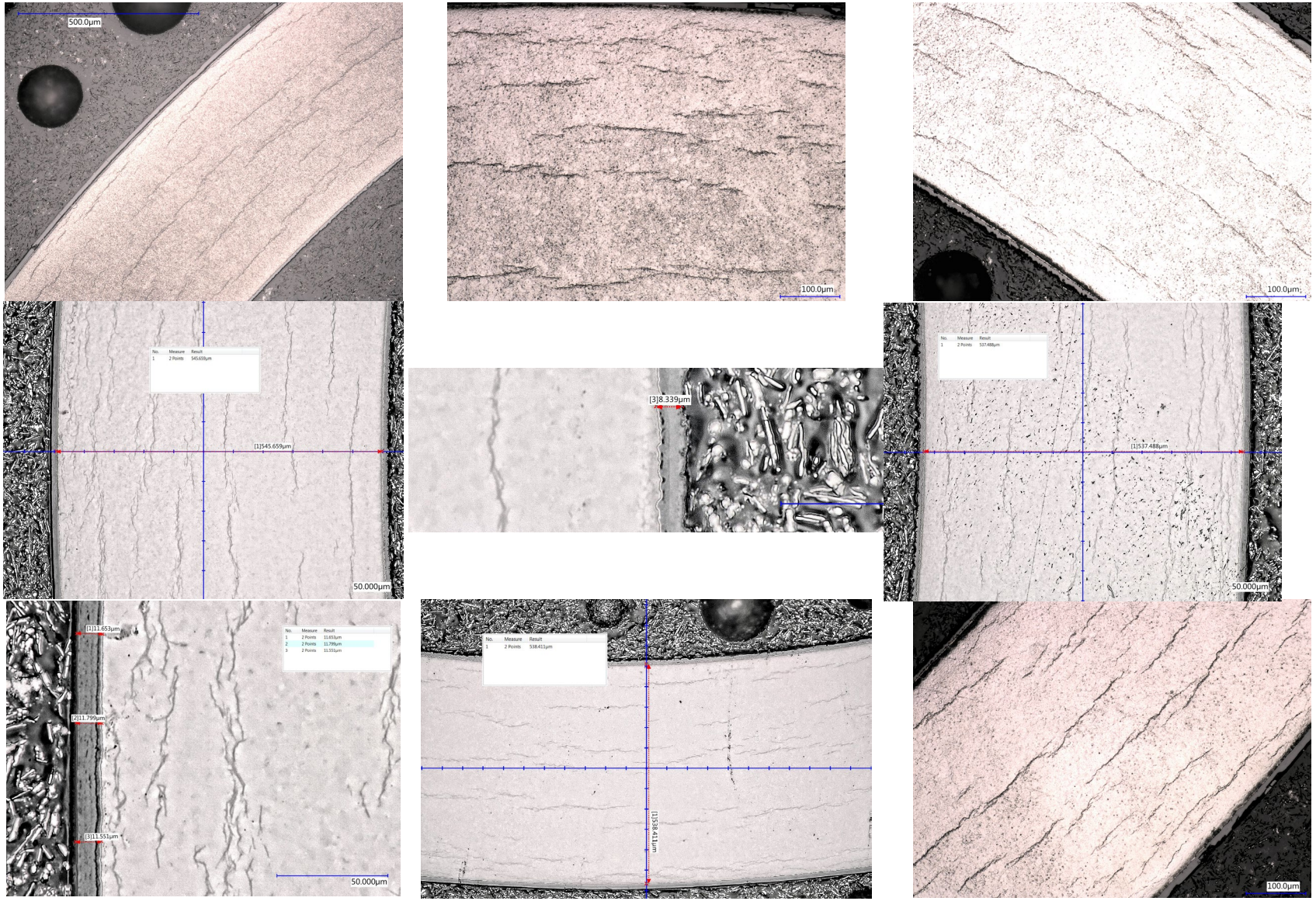

Figure B-19. Magnified areas of the cladding, 30AD05-3240-3259 (baseline rod).

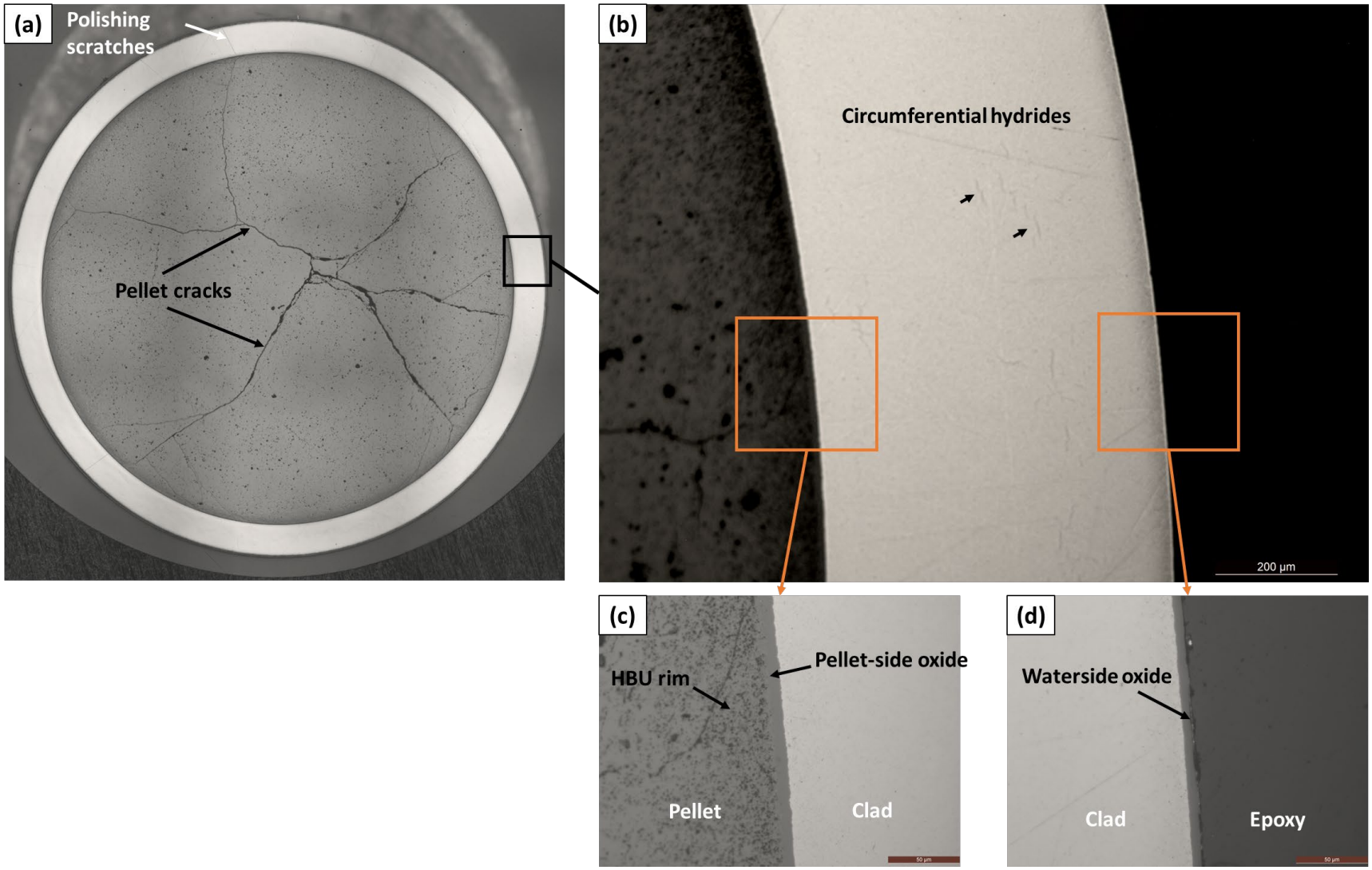

Figure B-20. Views of 30AE14-1677-1696 (fueled and unetched FHT rod): (a) overall cross-section showing pellet crack morphology, (b) magnified image of the right quarter showing small cladding circumferential hydrides (contrasted for better visibility) (scale bar=200 µm), (c) pellet-side oxide and HBU rim (scale bar=50 µm), and (d) waterside oxide layer (scale bar=50 µm).

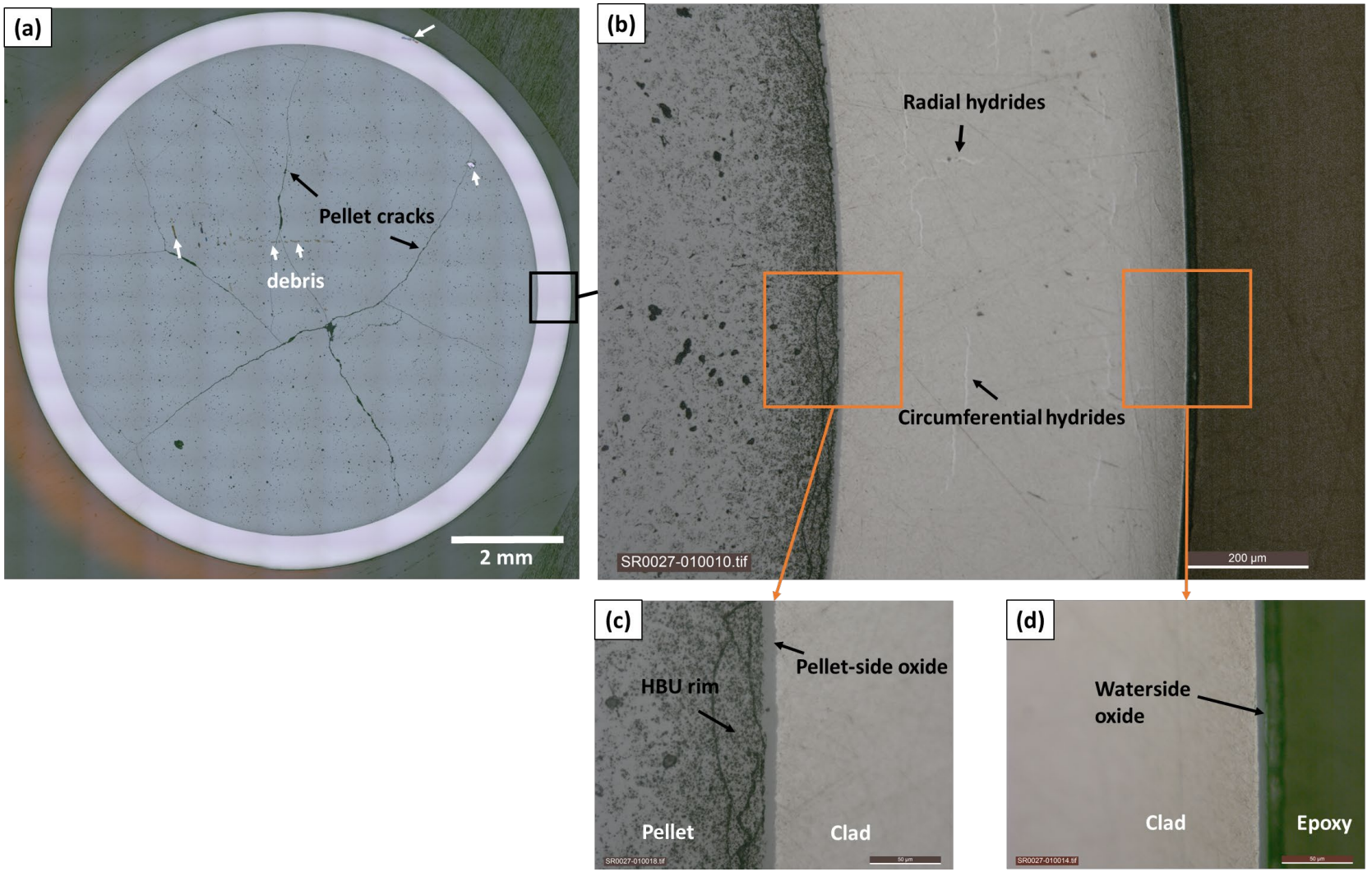

Figure B-21. Views of 30AE14-2203-2222 (fueled and unetched FHT rod): (a) overall cross-section showing pellet crack morphology, (b) magnified representative image captured from the right quarter of the sample showing circumferential and radial hydrides (scale bar=200 µm), (c) pellet-side oxide and HBU rim (scale bar=50 µm), and (d) waterside oxide layer (scale bar=50 µm).

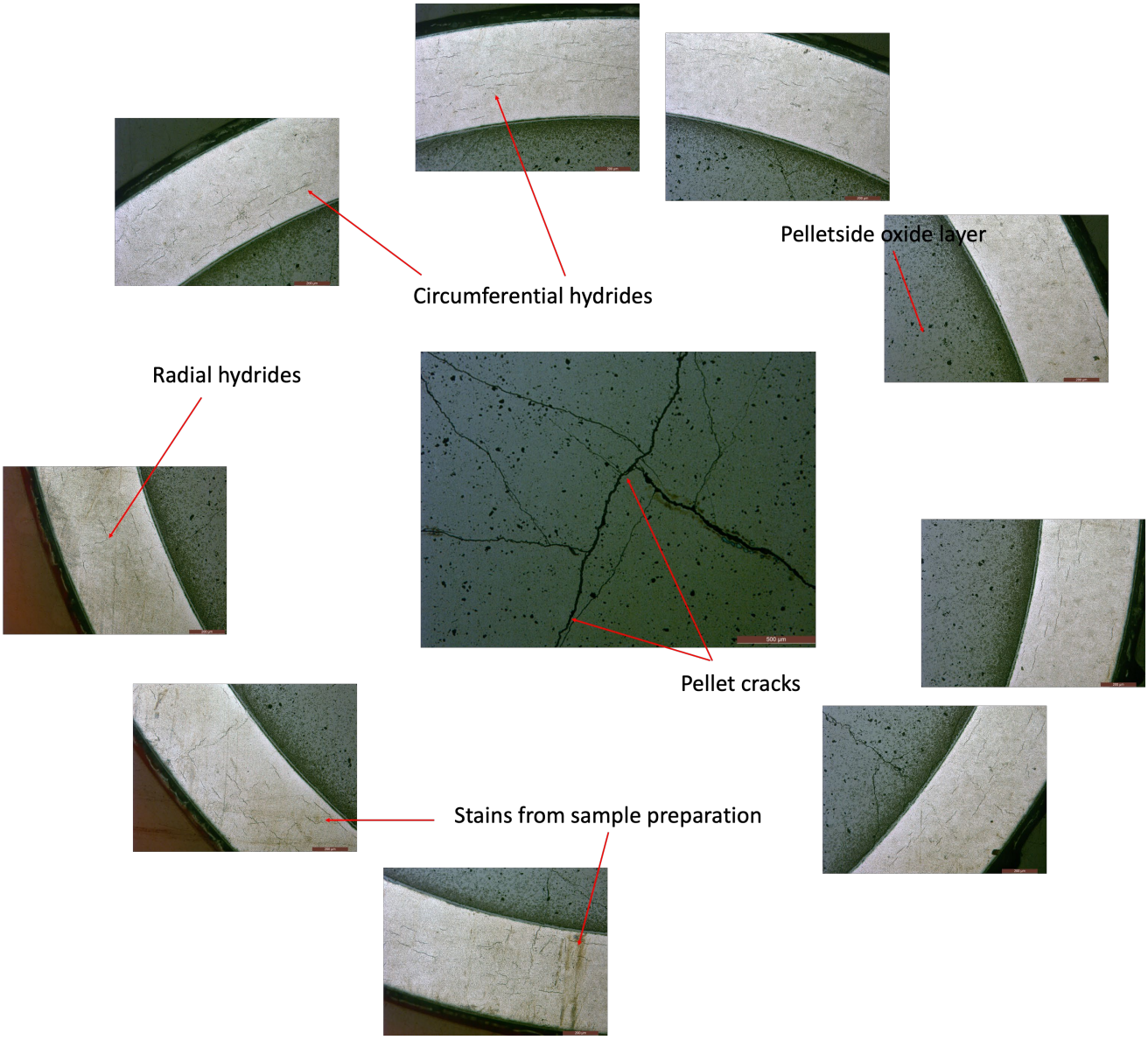

Figure B-22. Fueled overview of 30AE14-2203-2222.

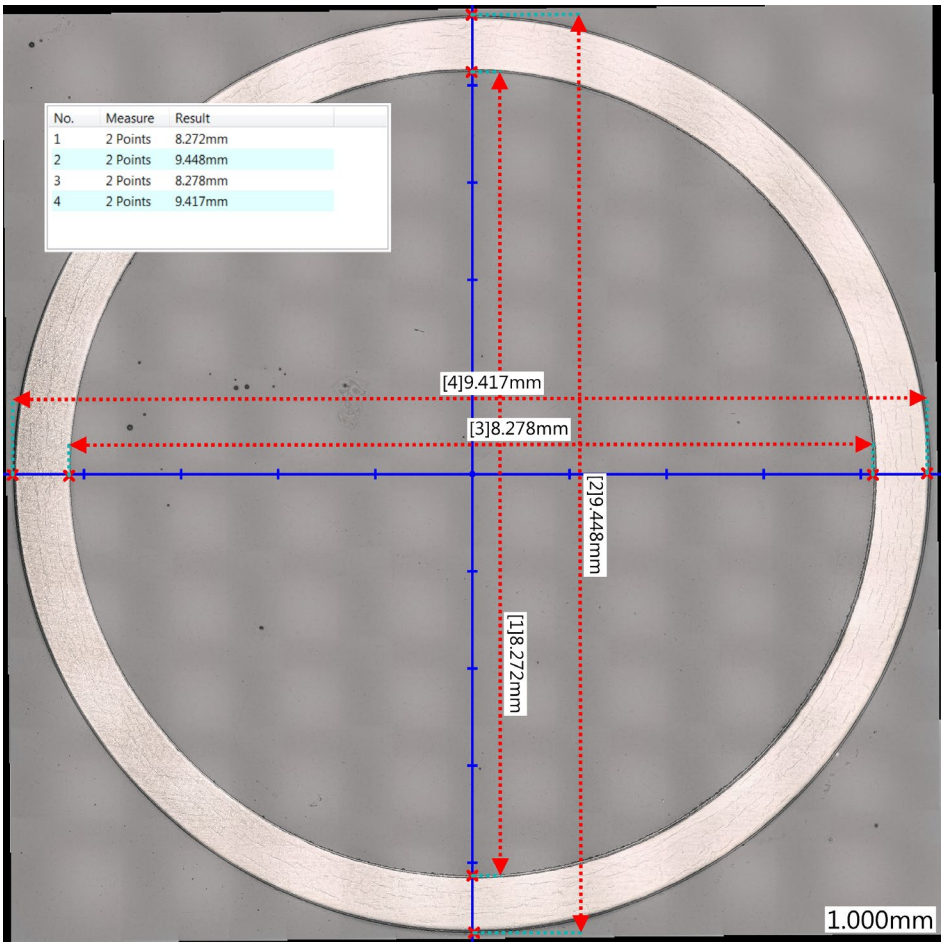

Figure B-23. Defueled overall view, 30AE14-2675-2694 (heat-treated).

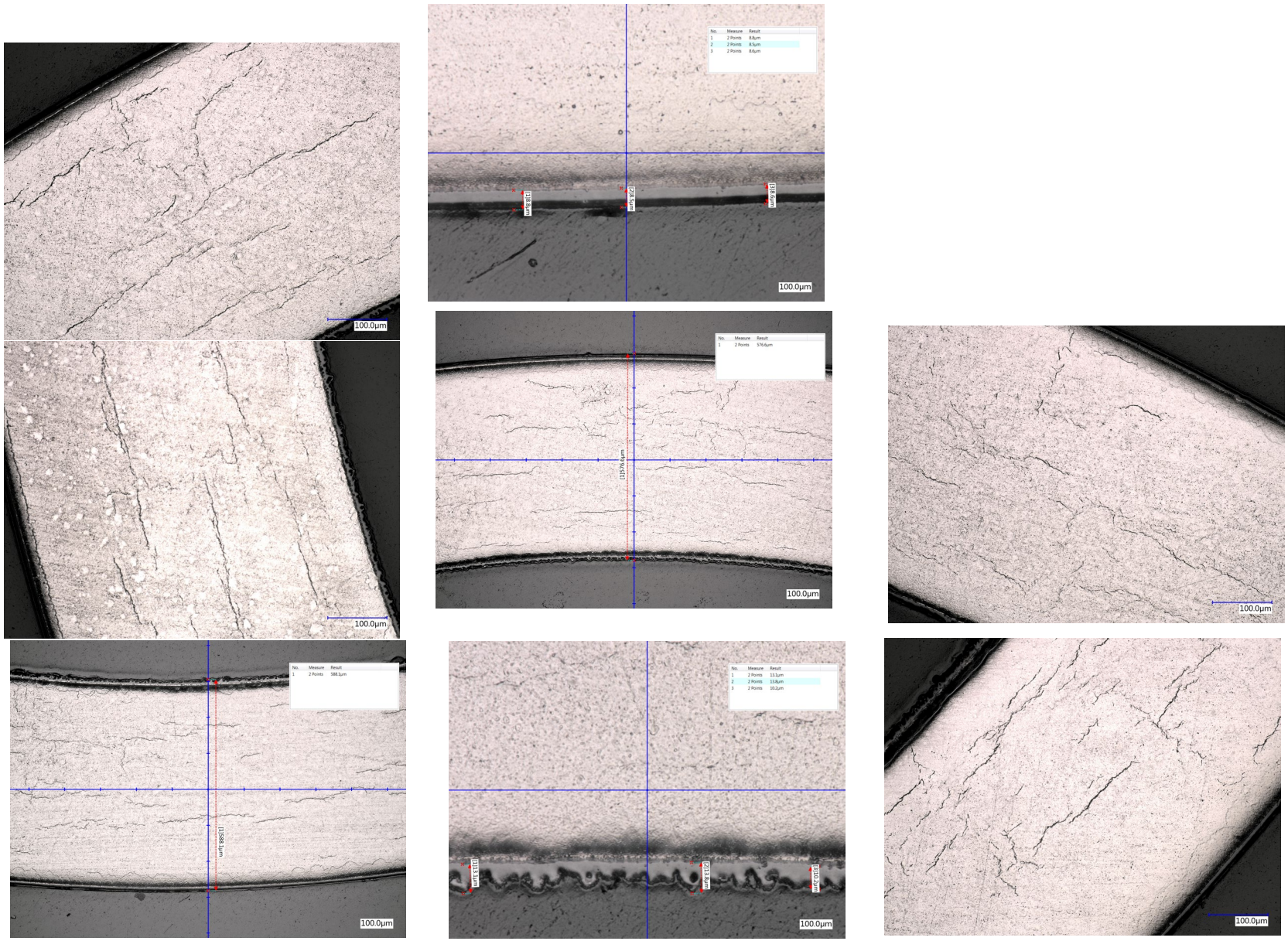

Figure B-24. Magnified areas of the cladding, 30AE14-2675-2694 (heat-treated).

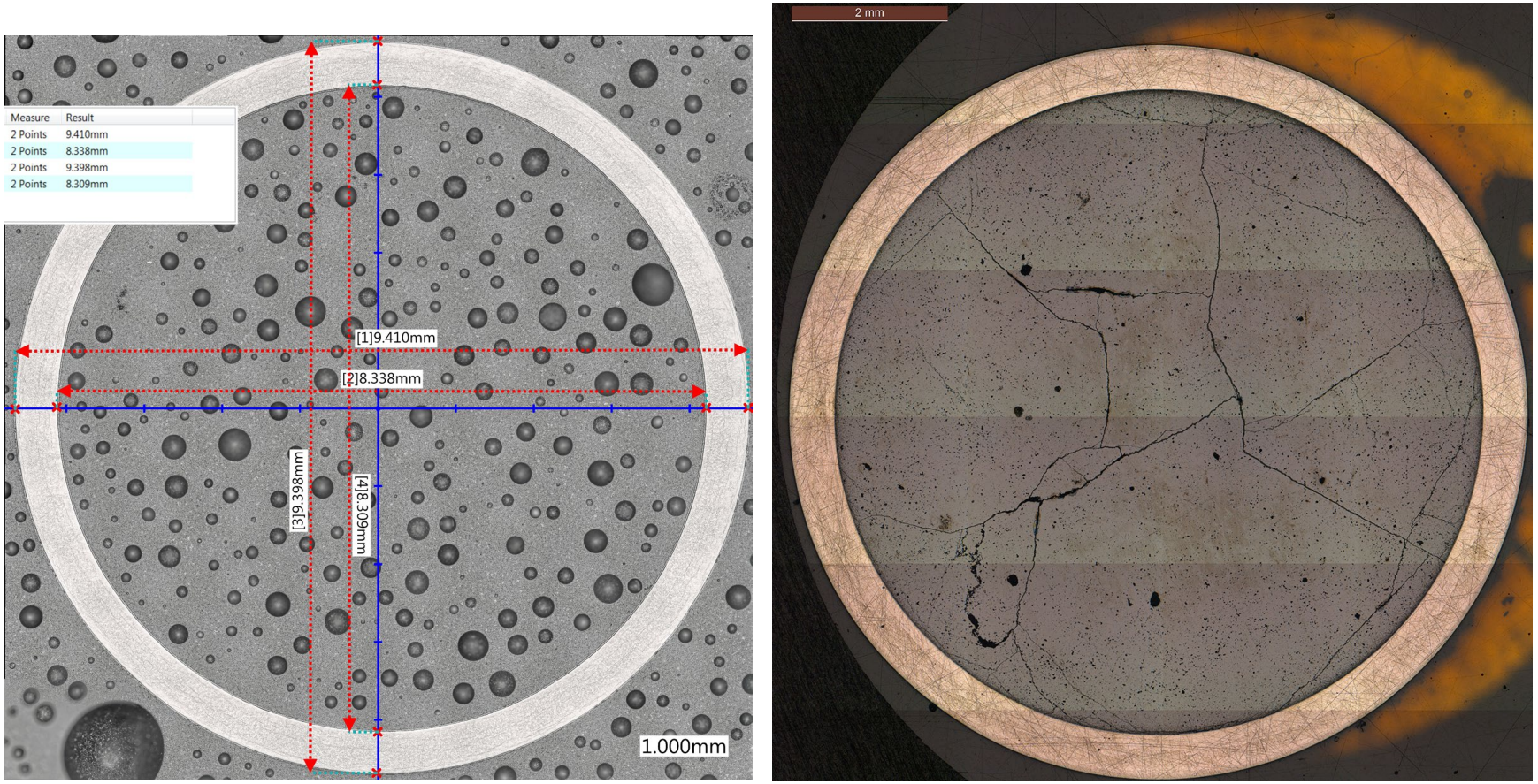

Figure B-25. Fueled (right) and defueled (left) overall section views, 30AE14-3399-3418 (heat-treated rod).

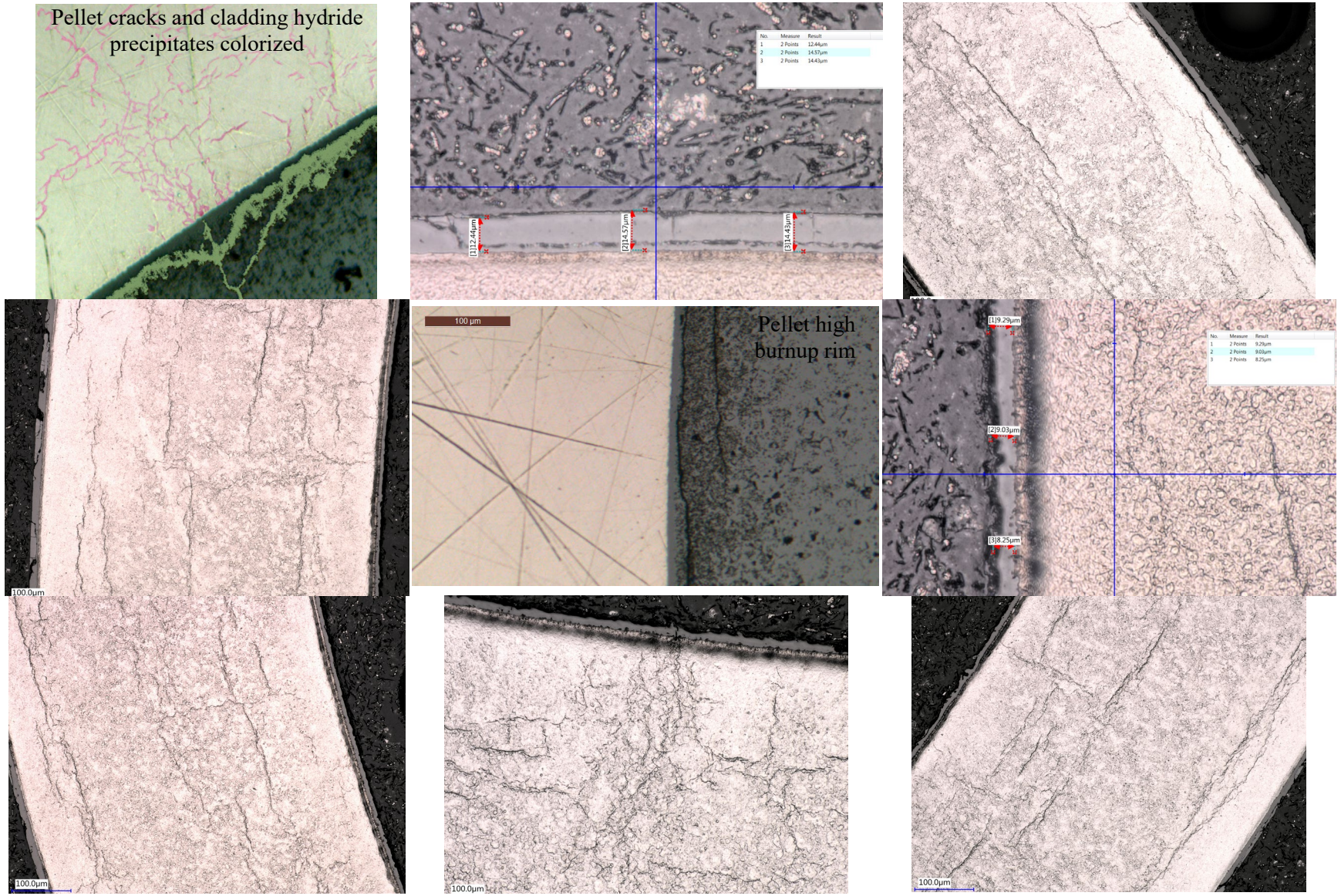

Figure B-26. Magnified views, 30AE14-3399-3418 (heat-treated rod).

B-3.3 ZIRLO-Clad Sister Rods

Eleven MET mounts are available for the three Phase 1 ZIRLO-clad sister rods: 3D8E14 and 6U3K09 (as-received baseline rods), and 3F9N05 (FHT applied). Figure B-27 through Figure B-35 provide views of the baseline rods, and Figure B-36 through Figure B-43 provide views of the heat-treated rod. The three rods examined were from the same fuel vendor but were manufactured at different times and operated in different reactor cycles. At the elevations examined, the estimated burnup ranges from 43 to 64 GWd/MTU (see Table B-4). A specimen from 3F9N05-2300-2319 (Figure B-37) was damaged during the grinding, with deep scratches on the cladding surface; these polishing defects are noted on the image and should be ignored.

As expected, the visible hydride density increased with increasing axial elevation and increasing oxide thickness. The precipitated hydrides in the baseline ZIRLO-clad rods (3D8E14 and 6U3K09) are primarily located at the OD and ID of the cladding and are oriented circumferentially. For 3D8E14, there is both an ID and OD circumferential hydride rim, and also, there are unusual short hydrides in the central region of the wall that form a cross pattern (see Figure B-31 and Figure B-32). The circumferential hydrides are mainly homogenously distributed through the thickness of the cladding, with a slightly denser rim at the cladding OD, as shown in Figure B-33, Figure B-34, and Figure B-35. The 6U3K09 pellet is cracked in the expected pattern, with no missing pellet surface visible. The depth of the pellet HBU rim ranged from 59 to 91 μm for this baseline rod.

For the heat-treated ZIRLO-clad rod, a few hydrides were observed near the clad ID and OD at 700–719 mm axial elevation as shown in Figure B-36. The hydride density increases at higher axial elevations, and the circumferential hydrides appeared to be more regularly distributed through the wall section, as shown in Figure B-37, Figure B-38, and Figure B-39. Several short radial hydrides are visible at the ID and near the OD of the cladding. An inspection of magnified areas of the fueled METs indicate very short radial hydrides at pellet crack locations, as further discussed in Section B-3.6. The pellet cracks are as expected, with no missing pellet surface. The HBU rim is varied between 35–90 μm.

A pellet–pellet gap of 3 mm was identified in rod 3D8E14 at an elevation of 1,403 mm during the NDE [B-4]. The rod was sectioned longitudinally at that elevation to reveal the pellet–pellet interfaces and the gap and to allow for additional examination of the pellet and cladding condition as related to the gap. A longitudinal slice of the section (approximately one third of the rod OD) was removed to reveal the pellets and was reserved for cladding hydrogen measurements. The resulting segment was then mounted and polished, and the gap was measured optically, as shown in Figure B-44. The gap is actually less than 1 mm, as shown in Figure B-44(a), and was overestimated by the gamma scan, likely because of the reduced gamma source at the chamfers and dishes in the pellets. The longitudinal specimen is slightly tilted in its mount, giving the appearance of a taper, as shown in Figure B-44(b). Because of the tilt and the off-center cut location, diameter measurements taken from the longitudinal image are not accurate. Axial measurements taken from the longitudinal image are less affected but are still inaccurate. The longitudinal view allows for inspection of both axial and radial pellet cracks that occurred during reactor operation. The pellet HBU rim is easily discernable and is enhanced at the pellet chamfer locations. The lower pellet has a small chip that relocated within the dish region as shown at the left end of Figure B-44(b). At least one chamfer has loose chips, as shown at the right end of Figure B-44(b). Figure B-45 provides closer views of these details and provides a view of the hydride distribution just inside the cladding ID. The ID cladding oxide layer is discontinuous at the pellet–pellet gaps, and although some pellet material appears to be well bonded with the cladding ID oxide, there is a continuous crack in the pellet that keeps the pellet and cladding from fully functioning as a solid mechanical section. Following axial imaging, the specimen was cross sectioned to allow views in the gap (Figure B-44[d]) and above (Figure B-44[e]) and below it (Figure B-44[c]). The OD, ID, oxide layers, cladding wall thickness, and pellet HBU rim were measured on the cross-sectional METs and are provided in Table B-6. For comparison, the intact rod OD measured during NDE using LVDTs is also listed in Table B-6. The pre-cut OD matches within 4 μm in the pellet elevations, but

after cutting, the MET-measured OD in the gap region is 8.8 μm larger. It is not clear whether some residual strain was released in the gap after cutting or whether this discrepancy is caused by measurement uncertainty. Figure B-46 provides examples of the hydride distribution in the cladding (a) above the gap in the pellet body, (b) in the gap, and (c) below the gap in the pellet body. Although the section above the gap was not fully polished and the central portion of the wall is thus not useful for comparison, there is not a visual difference in the hydride distribution in the gap as compared with the cladding in the pellet body region. Total cladding hydrogen measurements have been performed to better quantify any additional hydrogen (in solution or precipitated) in the pellet–pellet gap region and are discussed in Section B-4.

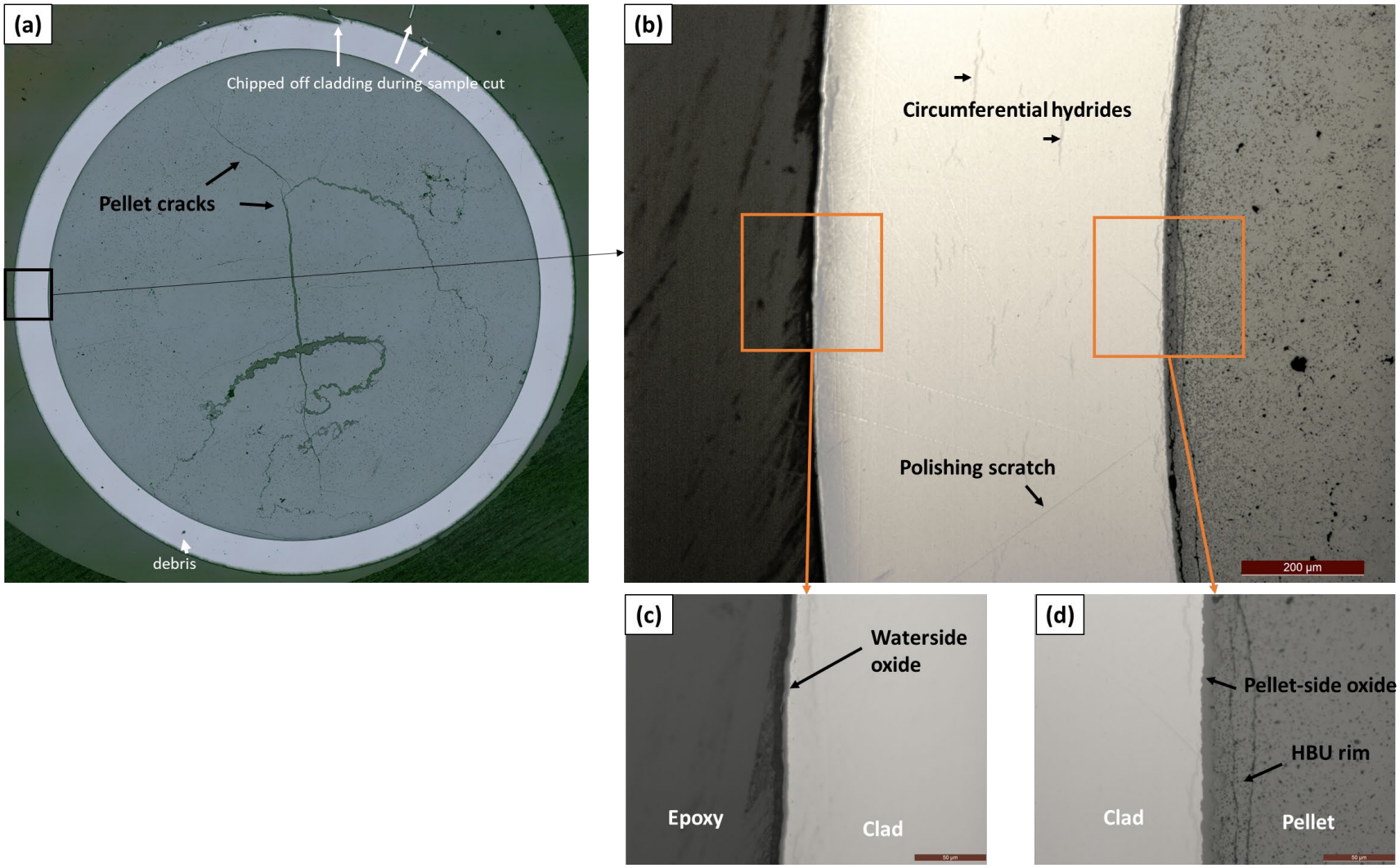

Figure B-27. Views of 3D8E14-0700-0719 (fueled and unetched baseline rod): (a) overall cross-section showing pellet crack morphology, (b) magnified representative image captured from the right quarter of the sample showing small circumferential hydrides (scale bar=200 µm), (c) waterside oxide layer (scale bar=50 µm), and (d) pellet-side oxide and HBU rim (scale bar=50 µm).

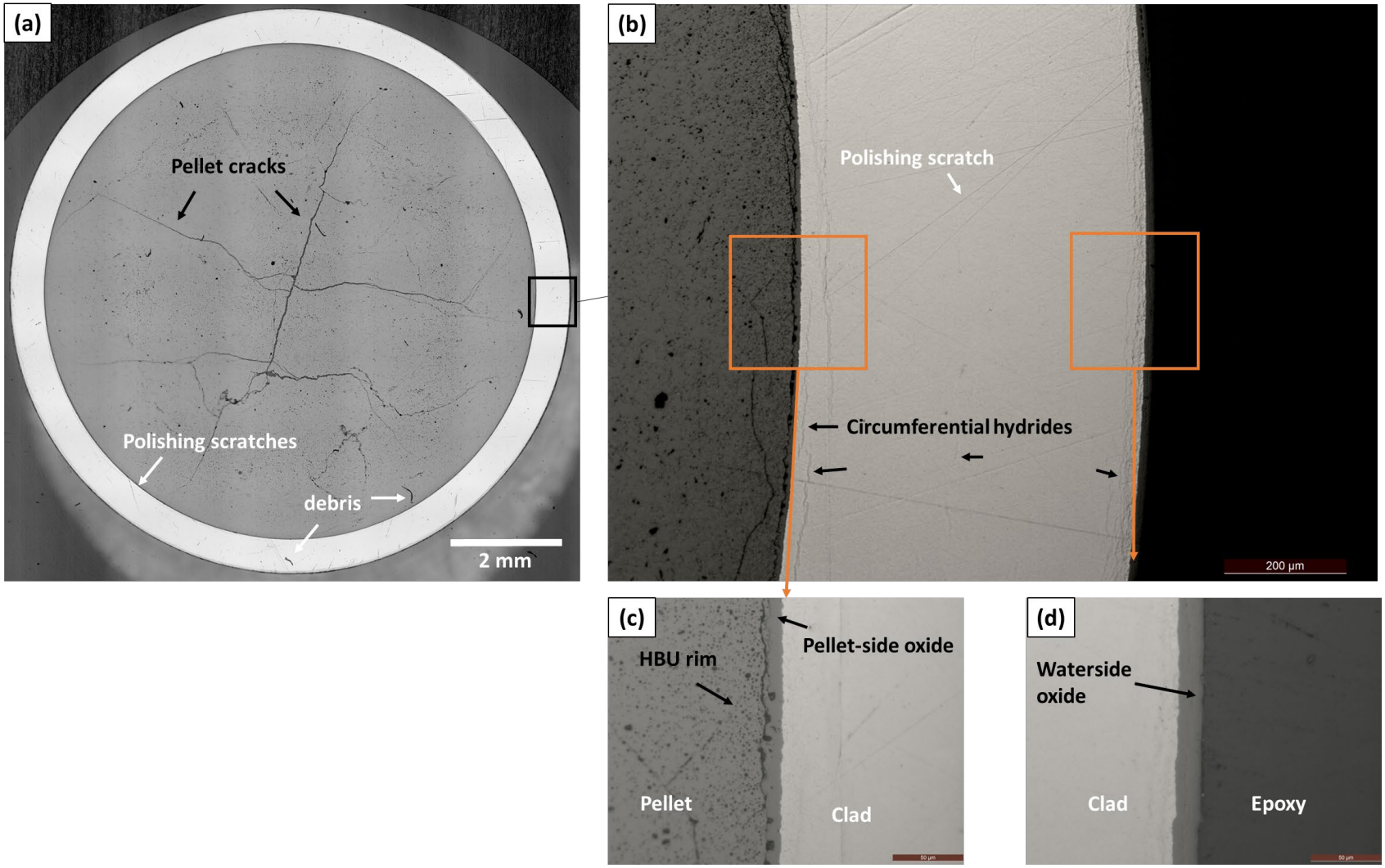

Figure B-28. Views of 3D8E14-2303-2322 (fueled and unetched baseline rod): (a) overall cross-section showing pellet crack morphology, (b) magnified representative image captured from the right quarter of the sample showing circumferential hydrides (contrasted for better visibility) (scale bar=200 µm), (c) pellet-side oxide and HBU rim (scale bar=50 µm), and (d) waterside oxide layer (scale bar=50 µm).

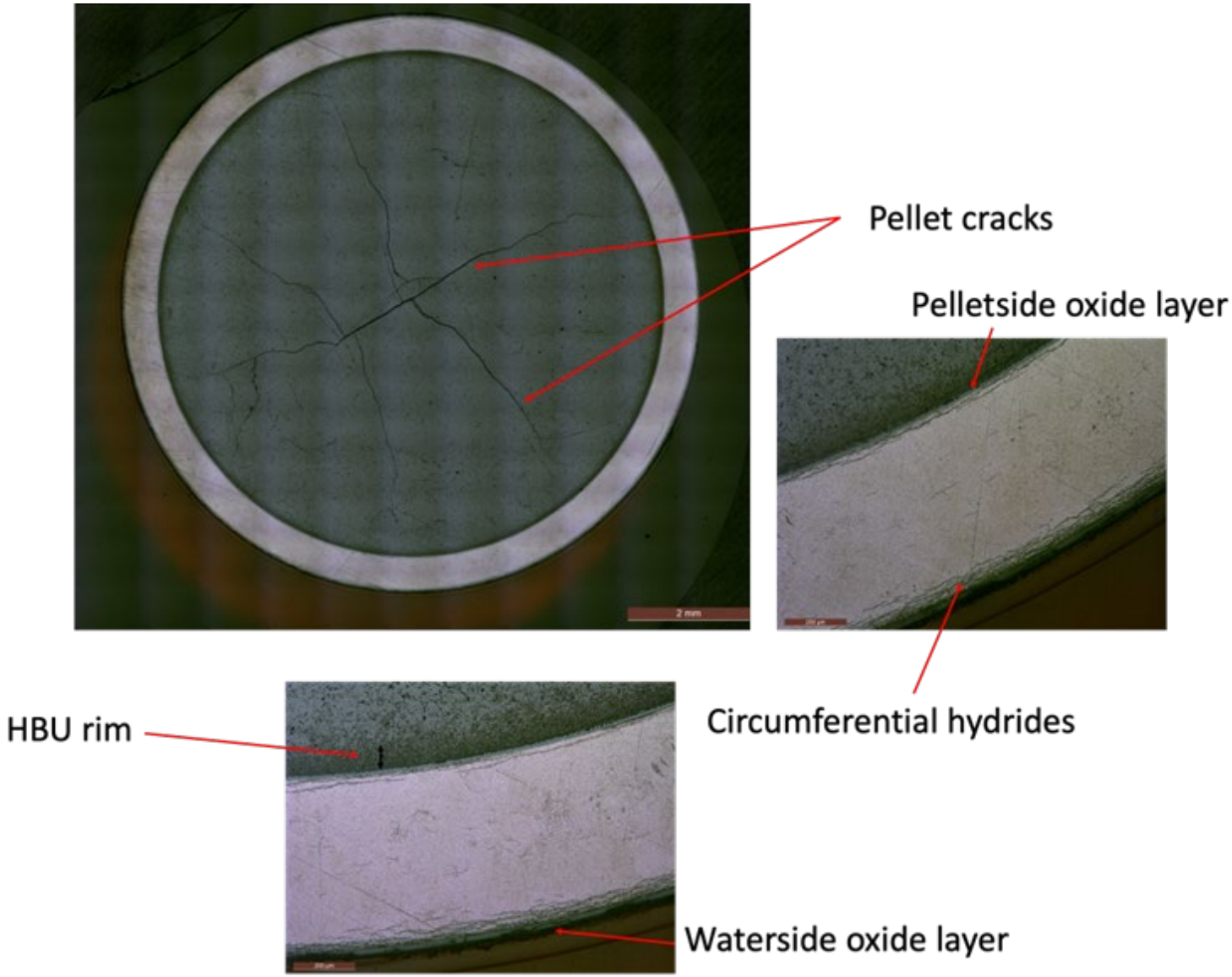

Figure B-29. Additional views of 3D8E14-2303-2322 after etching.

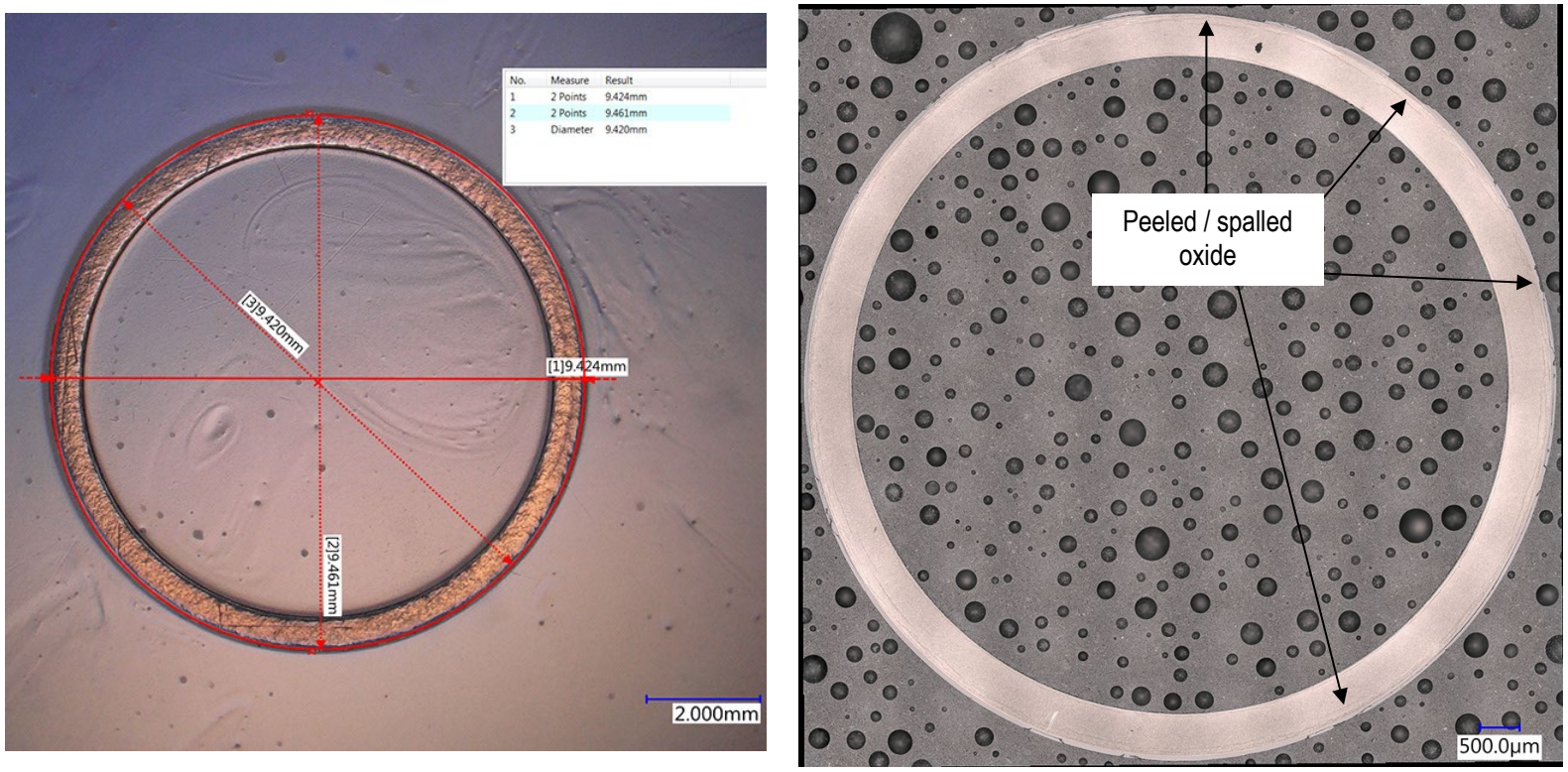

Figure B-30. Defueled overall view, 3D8E14-2655-2674 (left) and 3D8E14-3206-3225 (right) (baseline rod).

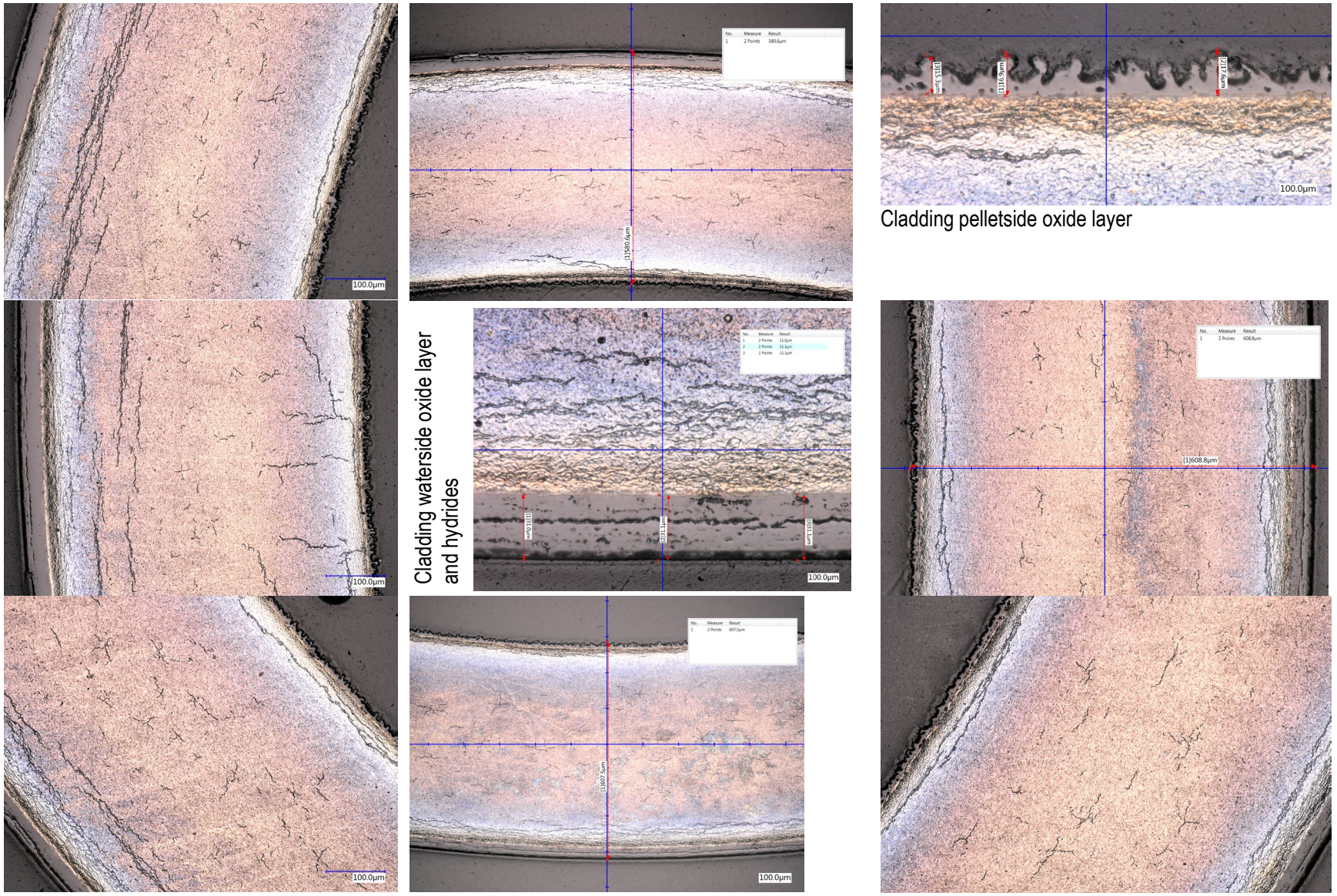

Figure B-31. Magnified areas of 3D8E14-2655-2674 cladding (baseline rod).

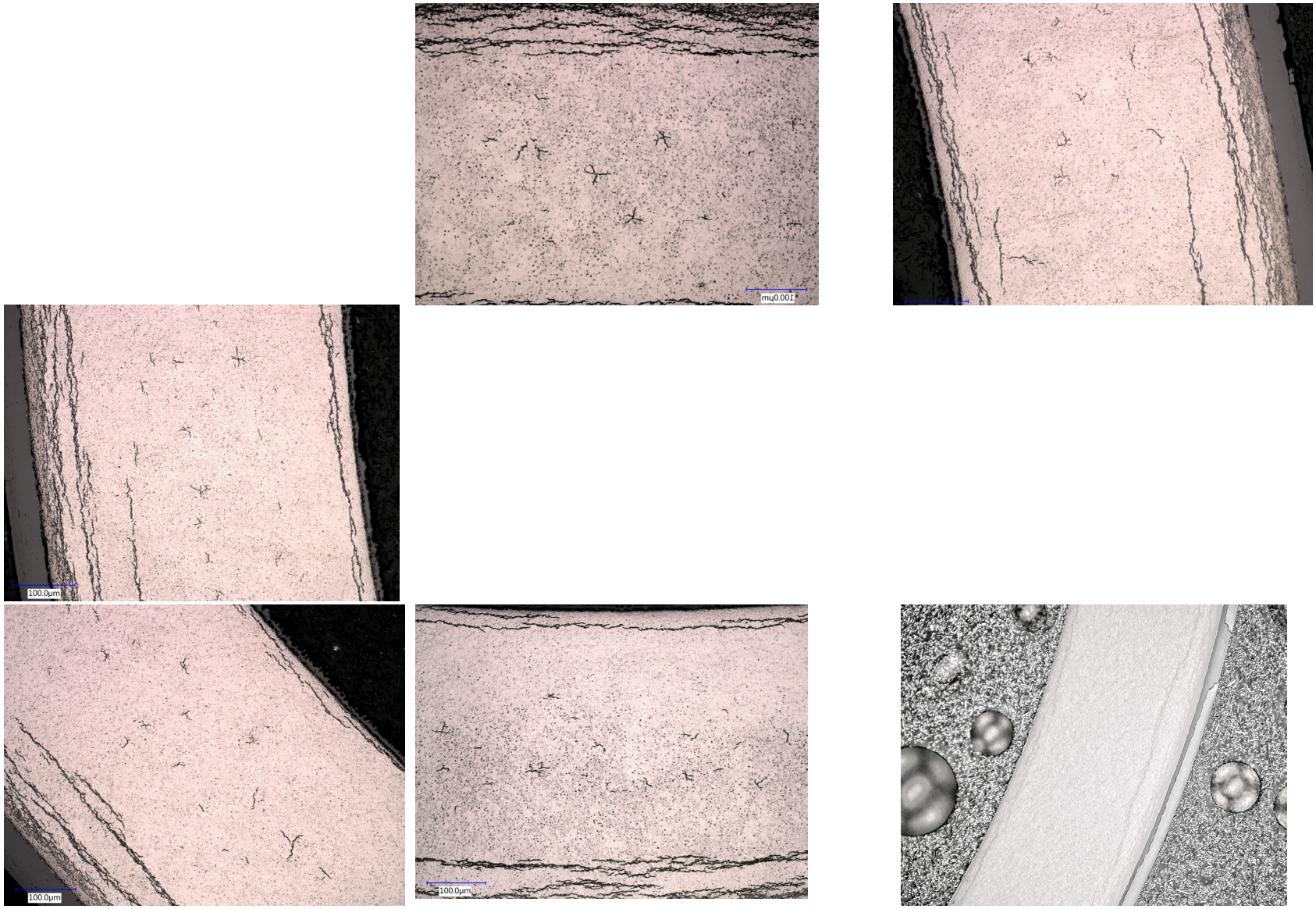

Figure B-32. Magnified areas of 3D8E14-3206-3225 cladding (baseline rod).

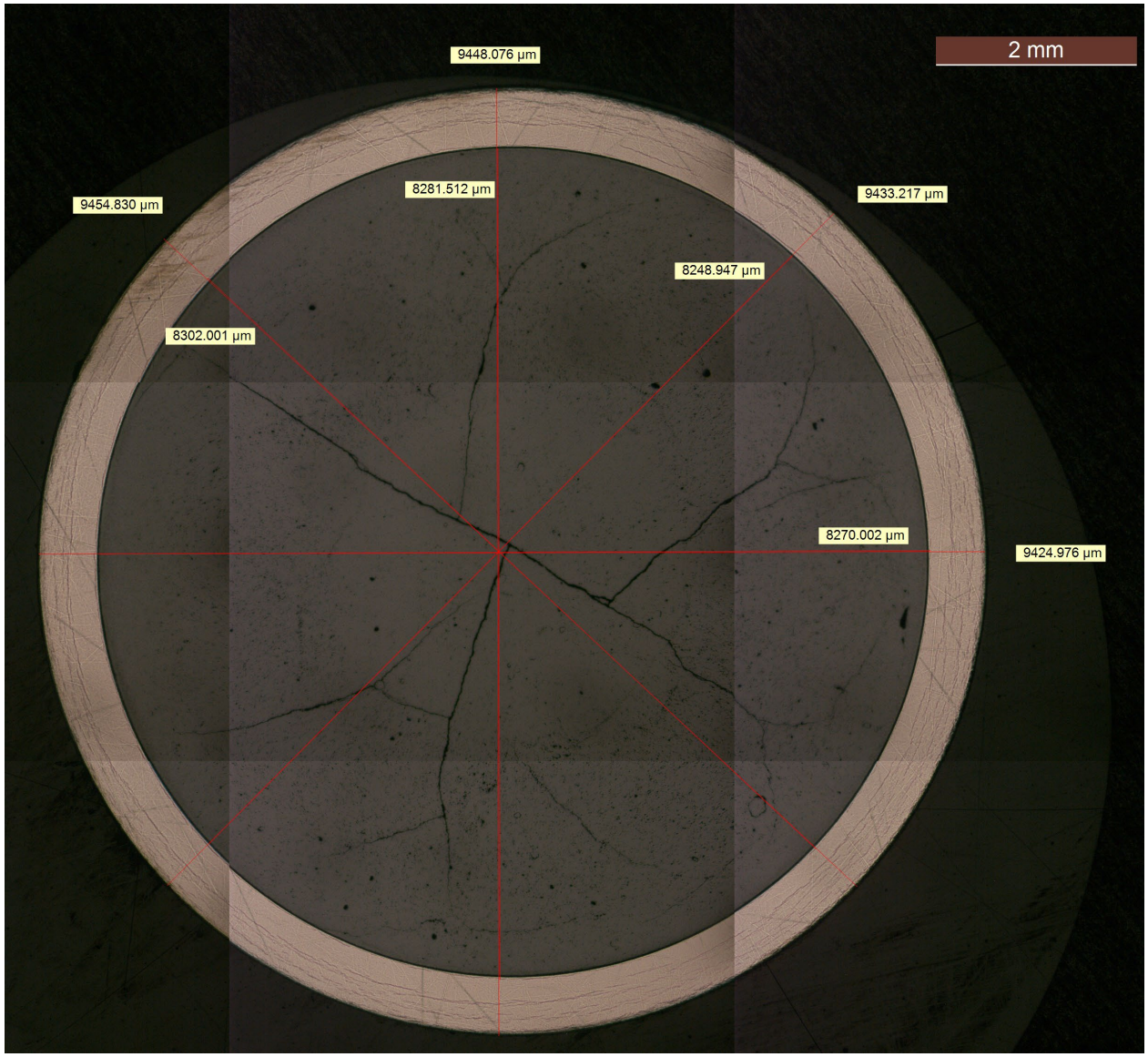

Figure B-33. Fueled overall view, 6U3K09-2616-2635 (baseline rod).

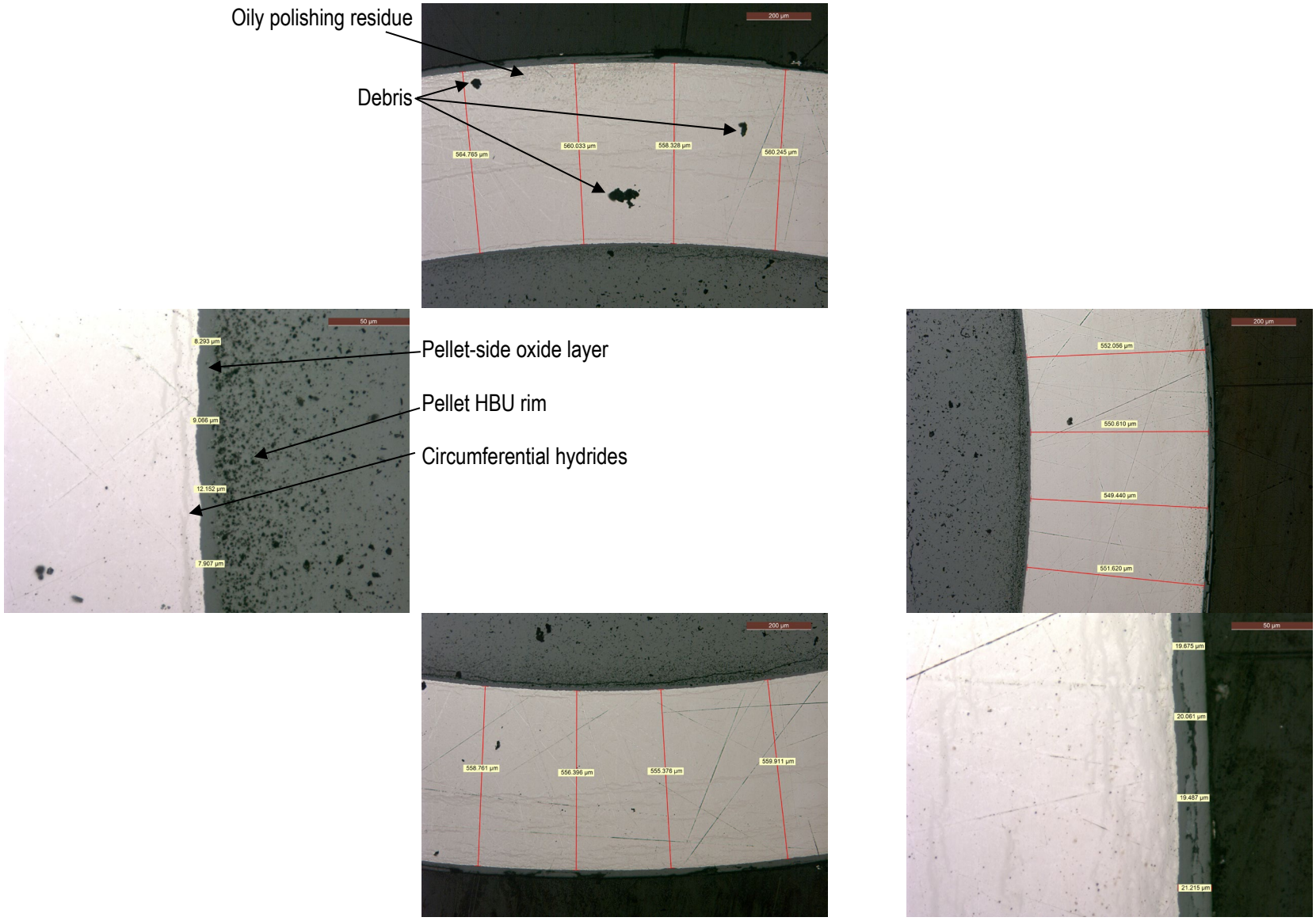

Figure B-34. Magnified views, 6U3K09-2616-2635 (baseline rod).

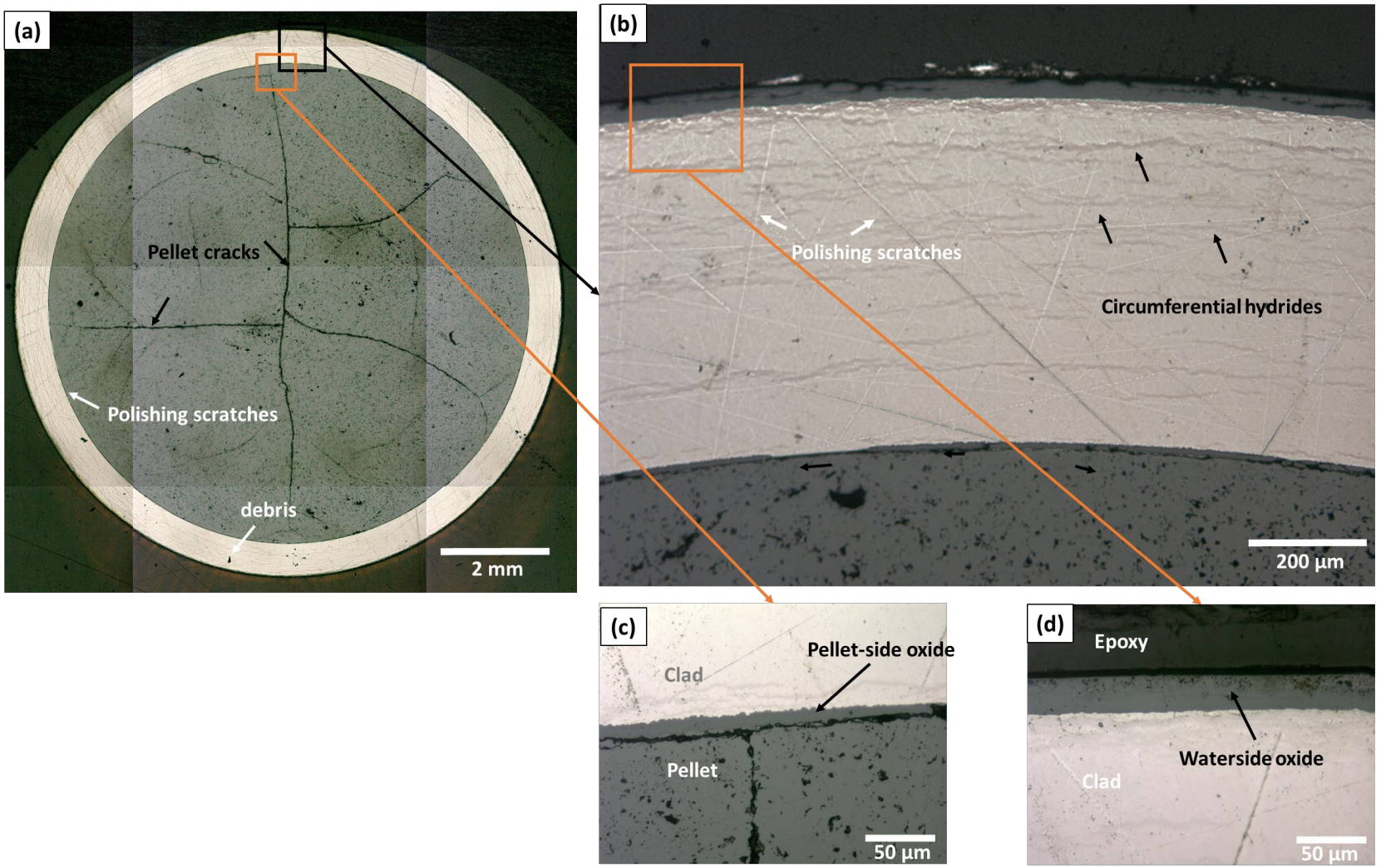

Figure B-35. Views of 6U3K09-3506-3525 (fueled and unetched baseline rod): (a) overall cross-section showing pellet crack morphology, (b) magnified representative image captured from the right quarter of the sample showing circumferential hydrides (scale bar=200 µm), (c) pellet-side oxide and HBU rim (scale bar=50 µm), and (d) waterside oxide layer (scale bar=50 µm).

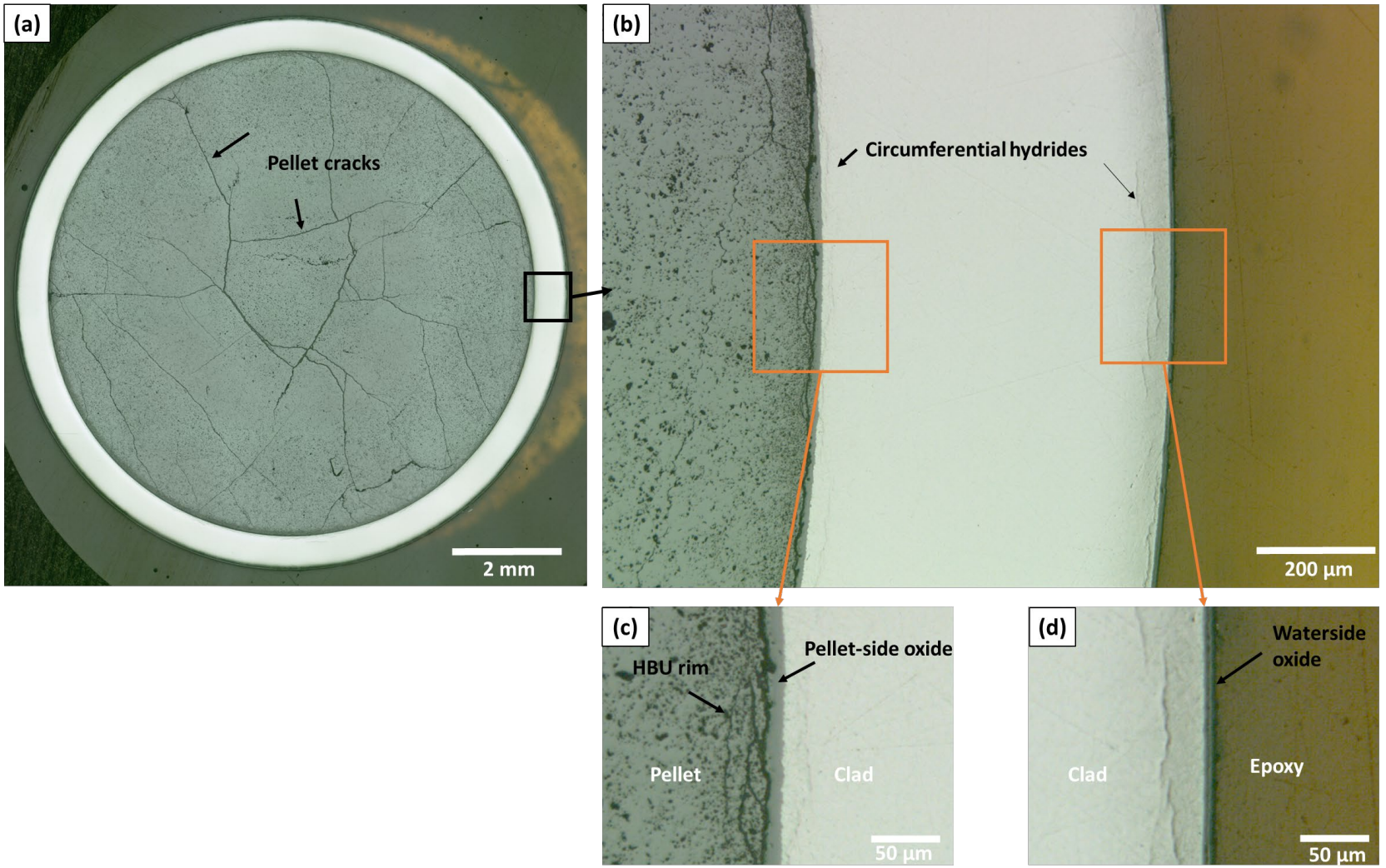

Figure B-36. Views of 3F9N05-0700-0719 (fueled and unetched heat-treated rod): (a) overall cross-section showing pellet crack morphology, (b) magnified representative image captured from the right quarter of the sample showing circumferential hydrides (scale bar=200 µm), (c) pellet-side oxide and HBU rim (scale bar=50 µm), and (d) waterside oxide layer (scale bar=50 µm).

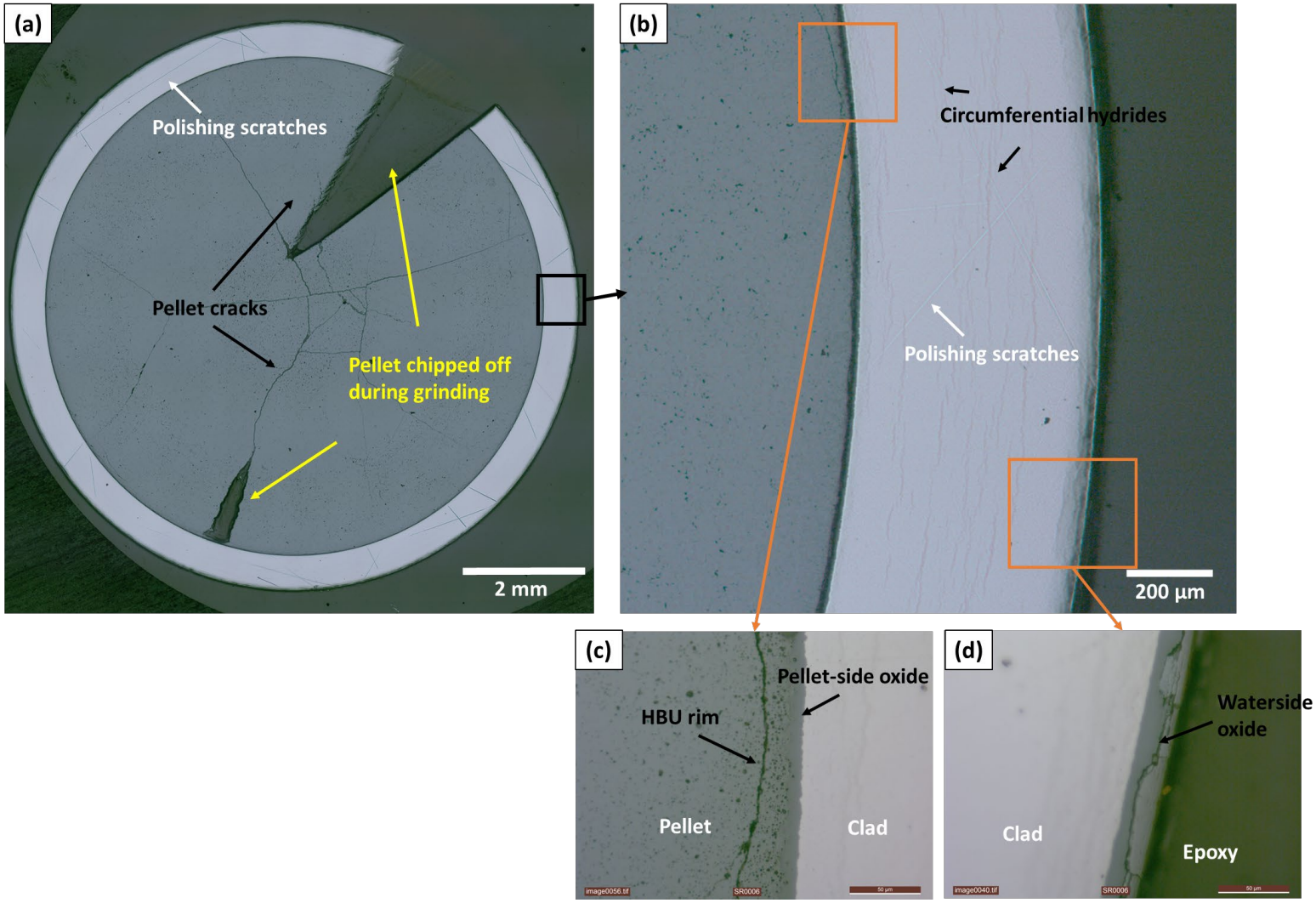

Figure B-37. Views of 3F9N05-2300-2319 (fueled and unetched heat-treated rod): (a) overall cross-section showing pellet crack morphology, (b) magnified representative image captured from the right quarter of the sample showing circumferential hydrides (scale bar=200 µm), (c) pellet-side oxide and HBU rim (scale bar=50 µm), and (d) waterside oxide layer (scale bar=50 µm).

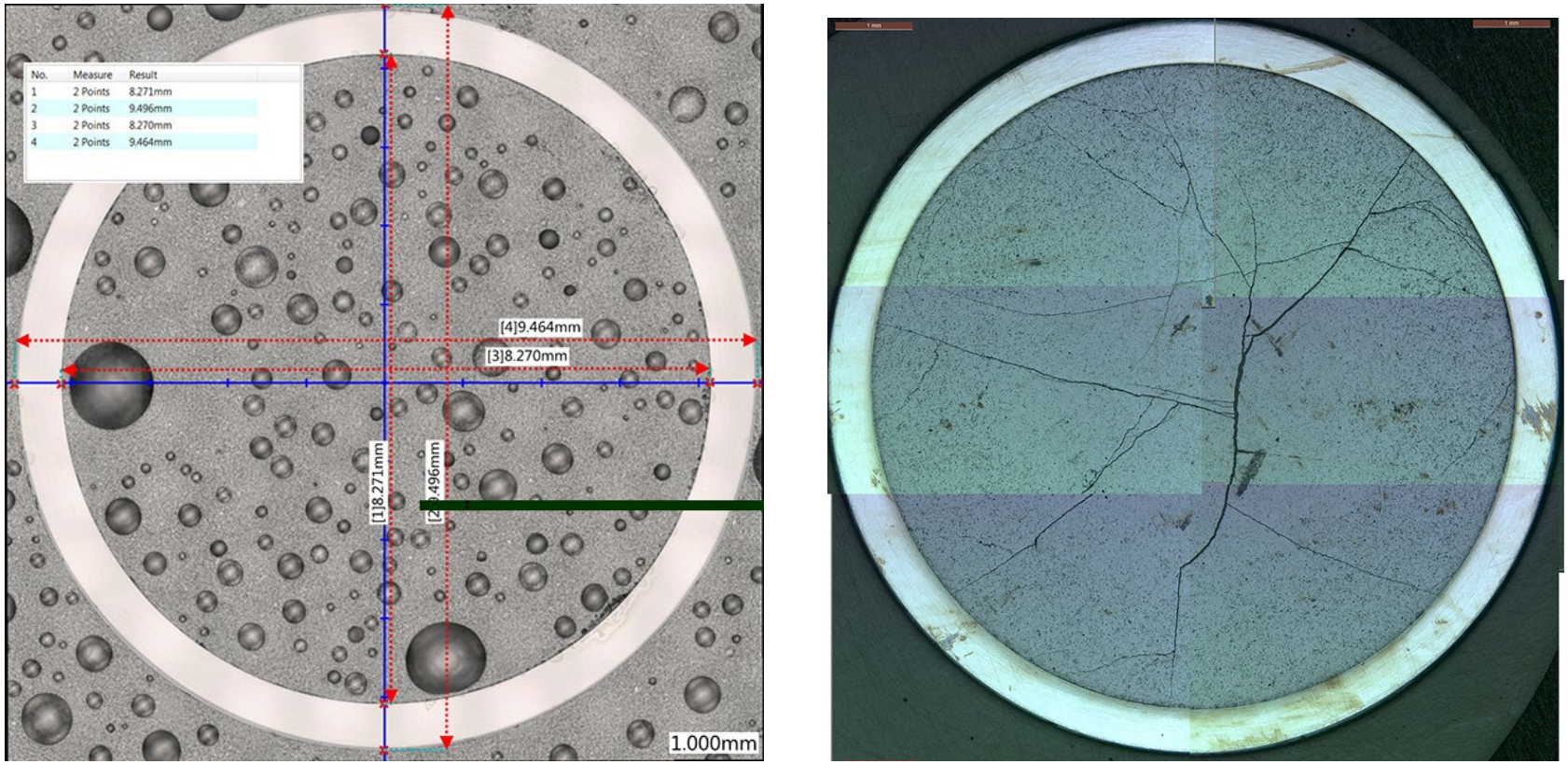

Figure B-38. Defueled (left) and fueled (right) overall views of 3F9N05-3331-3350 (heat-treated).

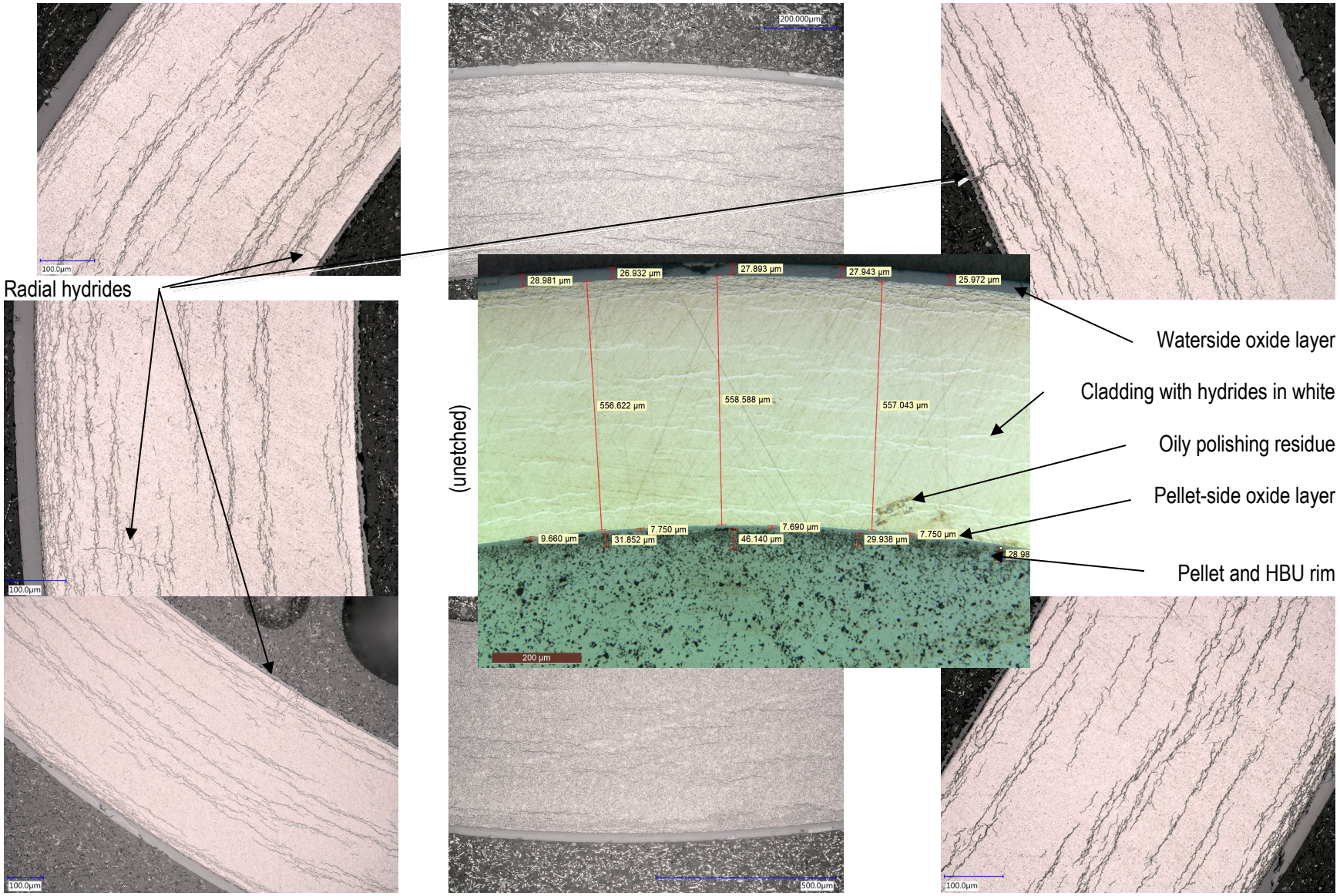

Figure B-39. Magnified views of 3F9N05-2863-2882 (heat-treated, etched).

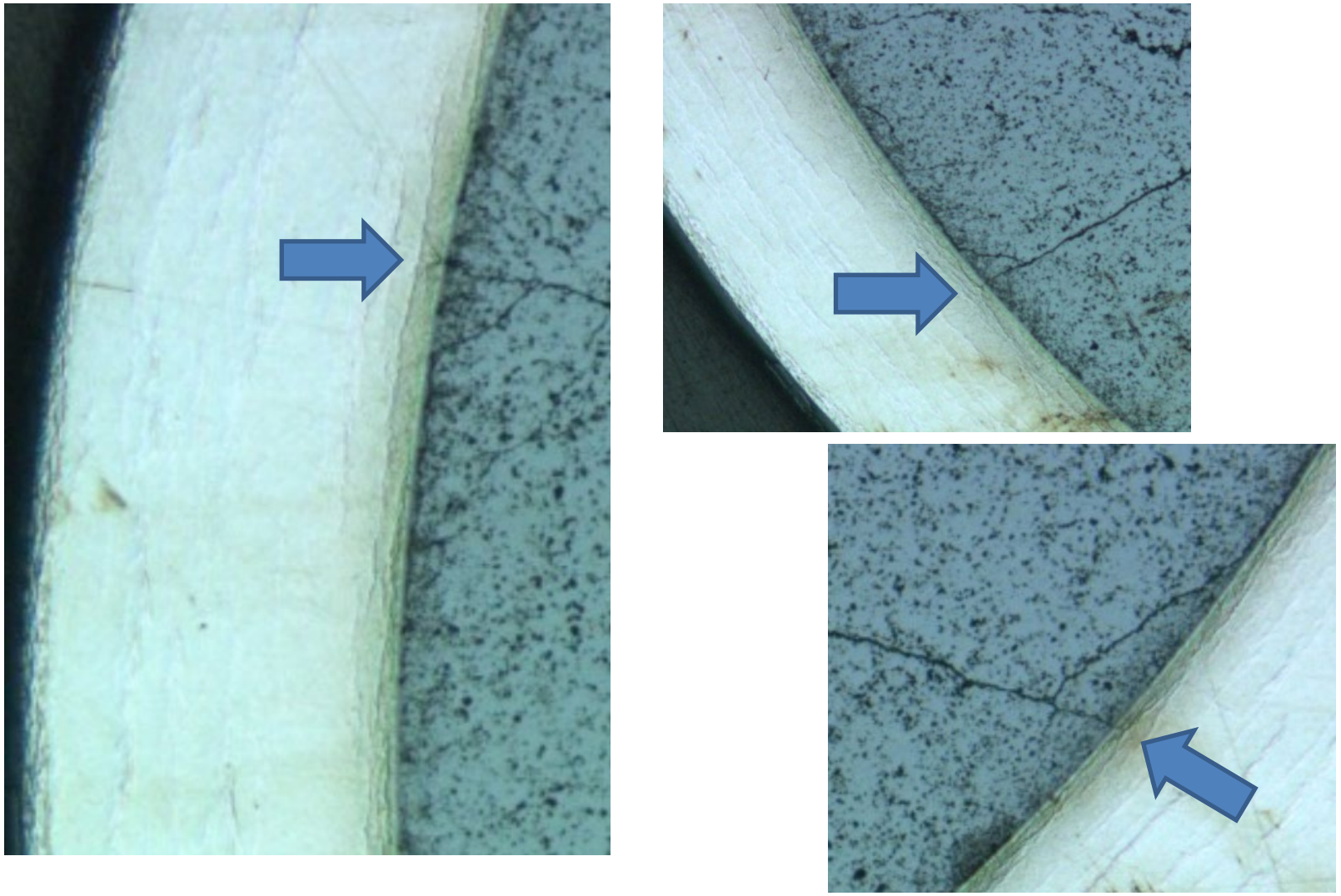

Figure B-40. Magnified views of 3F9N05-2863-2882 (heat-treated, unetched) with cladding at pellet crack locations indicated.

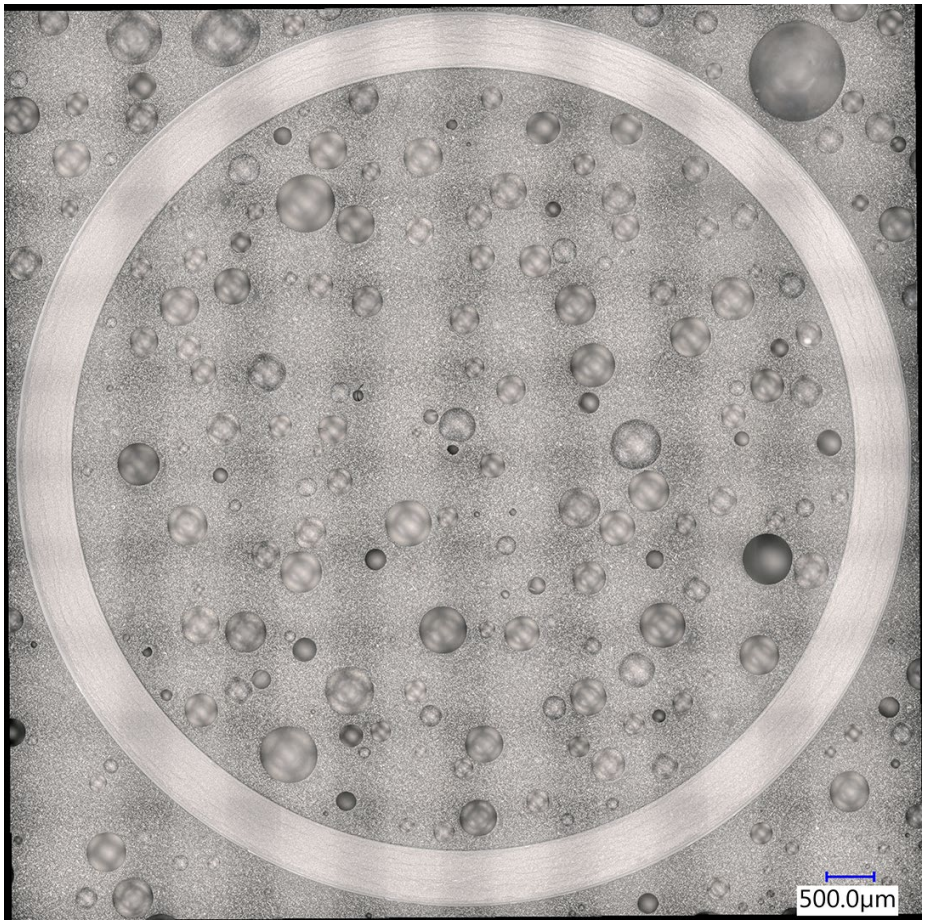

Figure B-41. Defueled overall view of 3F9N05-2863-2882 cladding (heat-treated).

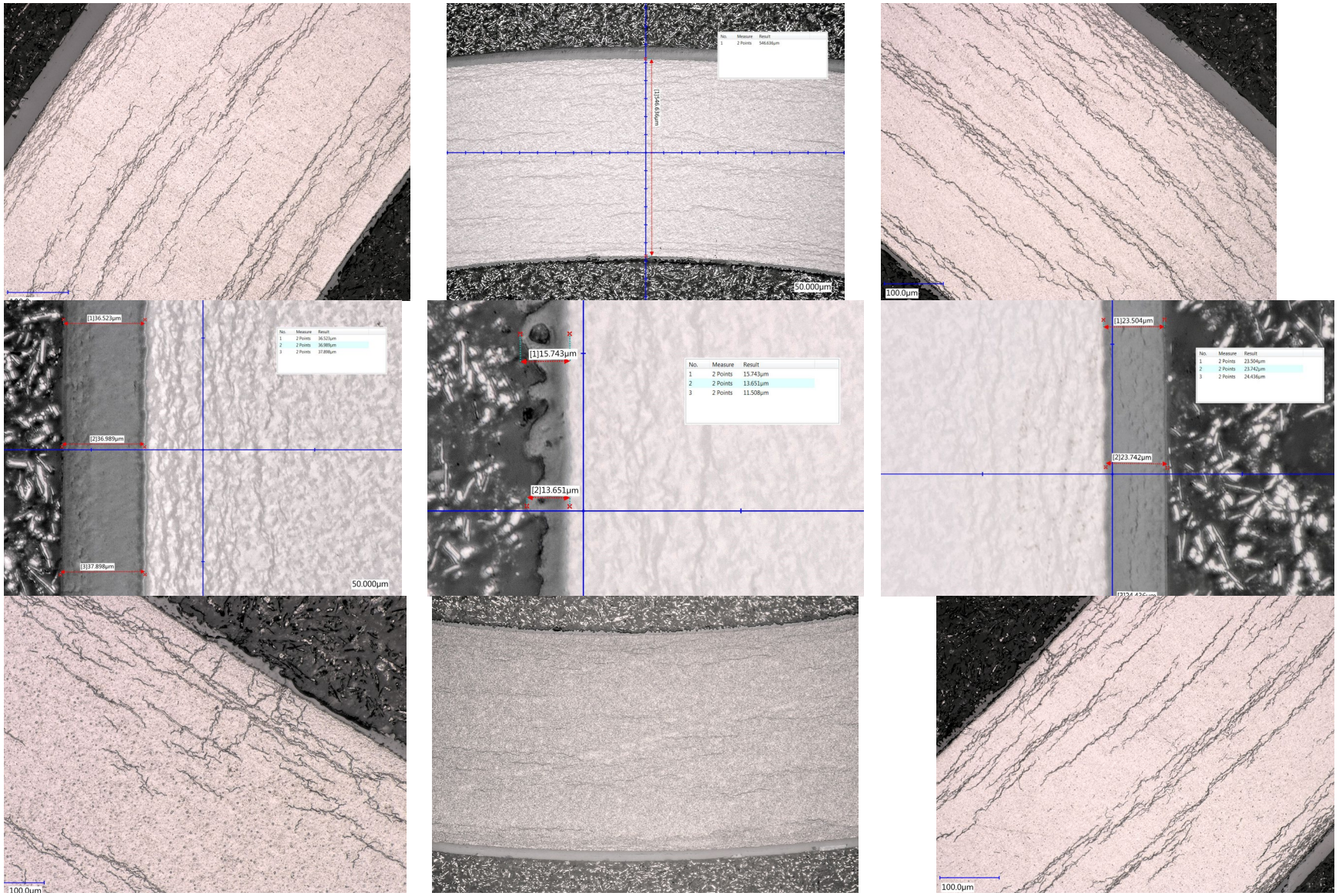

Figure B-42. Magnified views of 3F9N05-2863-2882 cladding (heat-treated, etched).

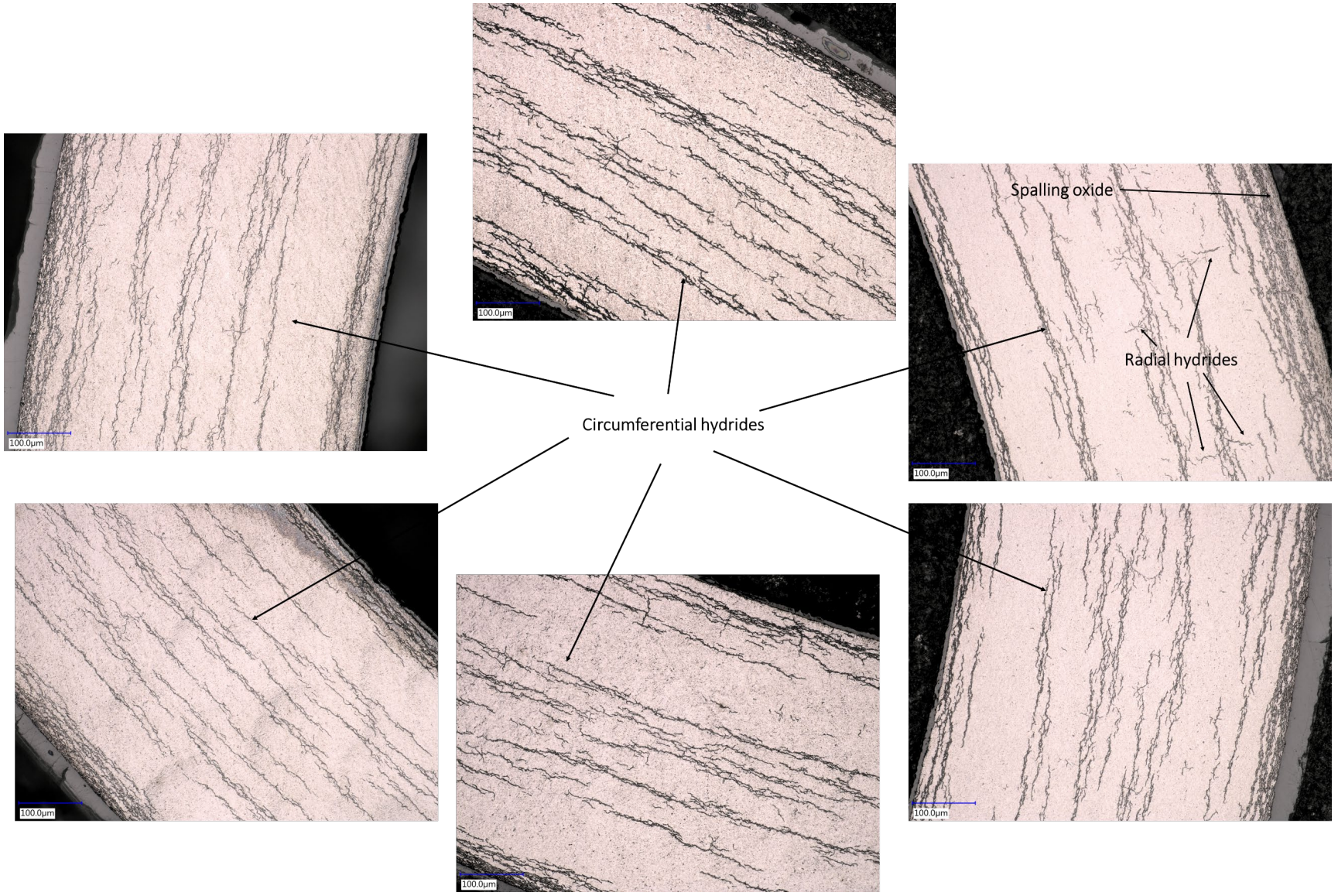

Figure B-43 Magnified views of 3F9N05-3331-3350 cladding (heat-treated, etched).

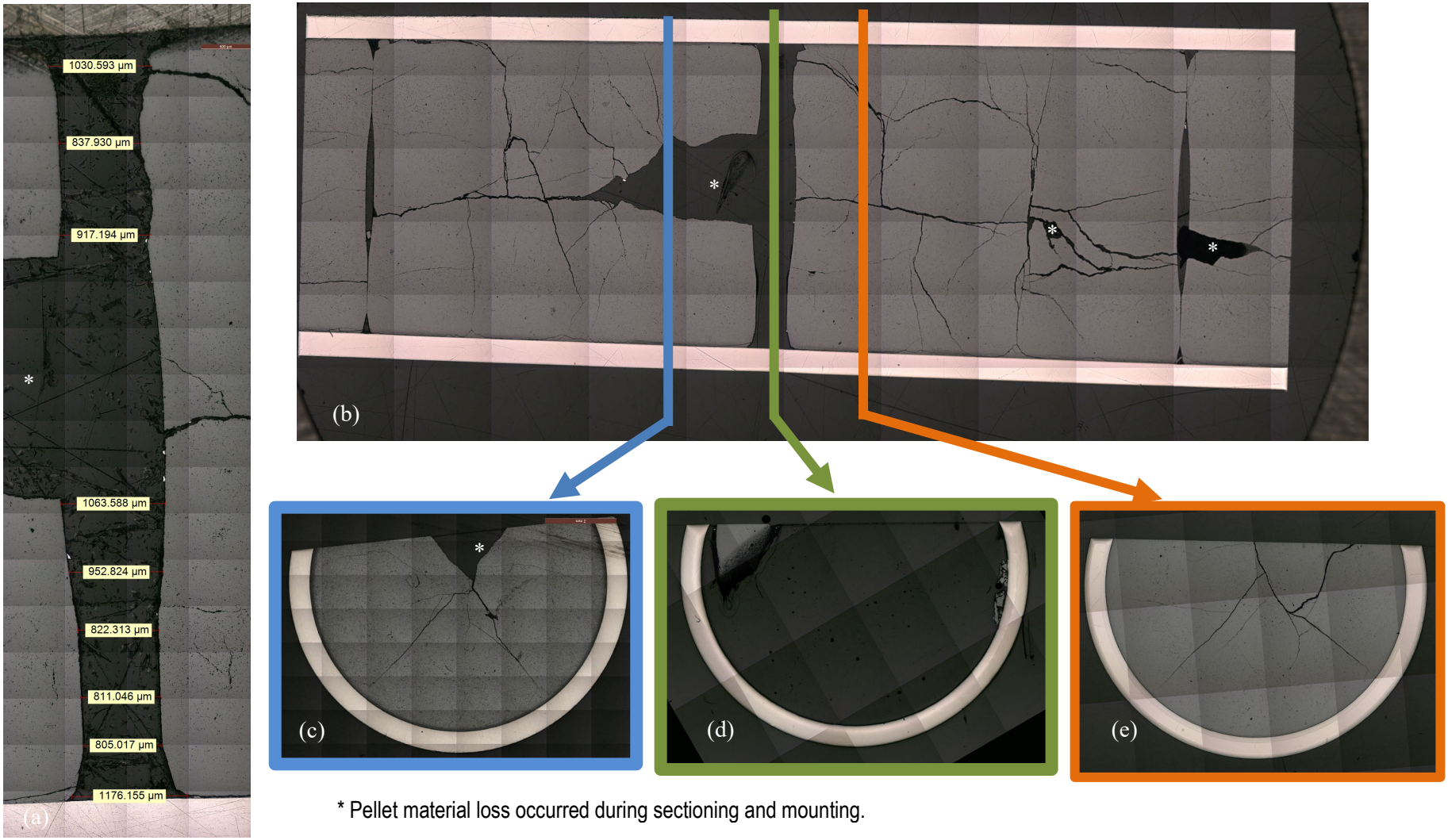

Figure B-44. 3D8E14 at 1,403 mm elevation: (a) pellet–pellet gap measurements, (b) longitudinal section view and cross-sectional view locations, (c) cross-sectional view of pellet below the pellet–pellet gap, (d) cross-sectional view in the pellet–pellet gap, and (e) cross-sectional view of the pellet above the pellet–pellet gap.

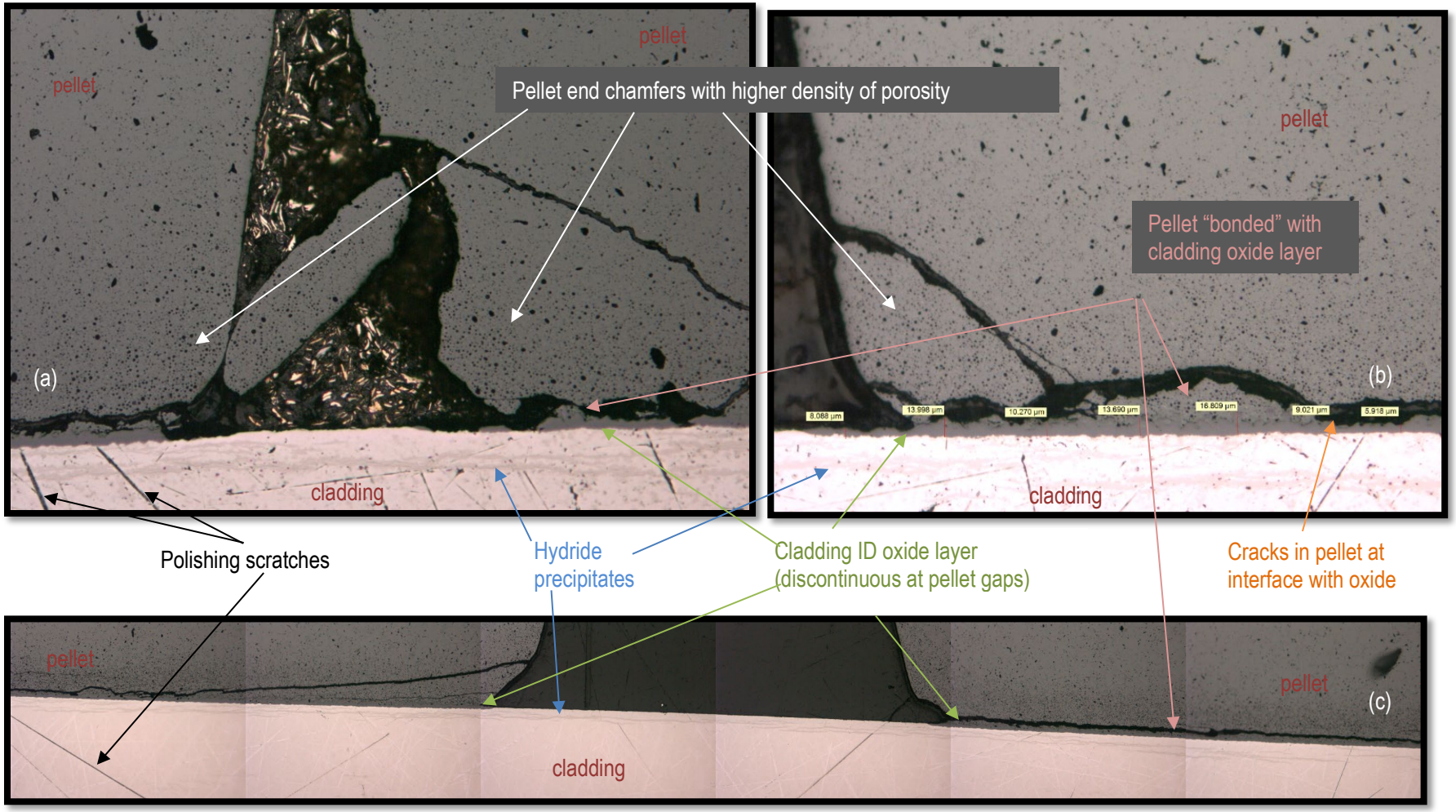

Figure B-45. 3D8E14 centered at 1,403 mm elevation 200× longitudinal views of three pellet–pellet interface locations showing pellet cracking, HBU rim and corner effects, and cladding ID hydrides.

Table B-6. Measurements of 3D8E14 centered at pellet-pellet gap elevation.

	Cladding wall thickness (µm)			Waterside oxide layer thickness (µm)			Pellet-side oxide layer thickness (µm)			Pellet HBU rim thickness (µm)			Cladding ID (µm)	Cladding OD (µm)	NDE average OD (µm)
	Average	Maximum	Minimum	Average	Maximum	Minimum	Average	Maximum	Minimum	Average	Maximum	Minimum			
Above gap (~1,408 mm elevation)	568.9	580.2	558.6	14.9	18.3	12.5	11.2	13.7	6.2	85.8	108.0	65.0	8,318.0	9,480.2	9,481.9
In gap (~1,403 mm elevation)	568.3	576.9	556.9	12.0	12.4	11.6	0	0	0	N/A			8,363.3	9,475.5	9,466.4
Below gap (~1,398 mm elevation)	569.7	582.9	558.2	12.9	15.6	9.2	11.7	17.5	7.9	85.1	130.5	61.5	8,339.4	9,483.4	9,480.0

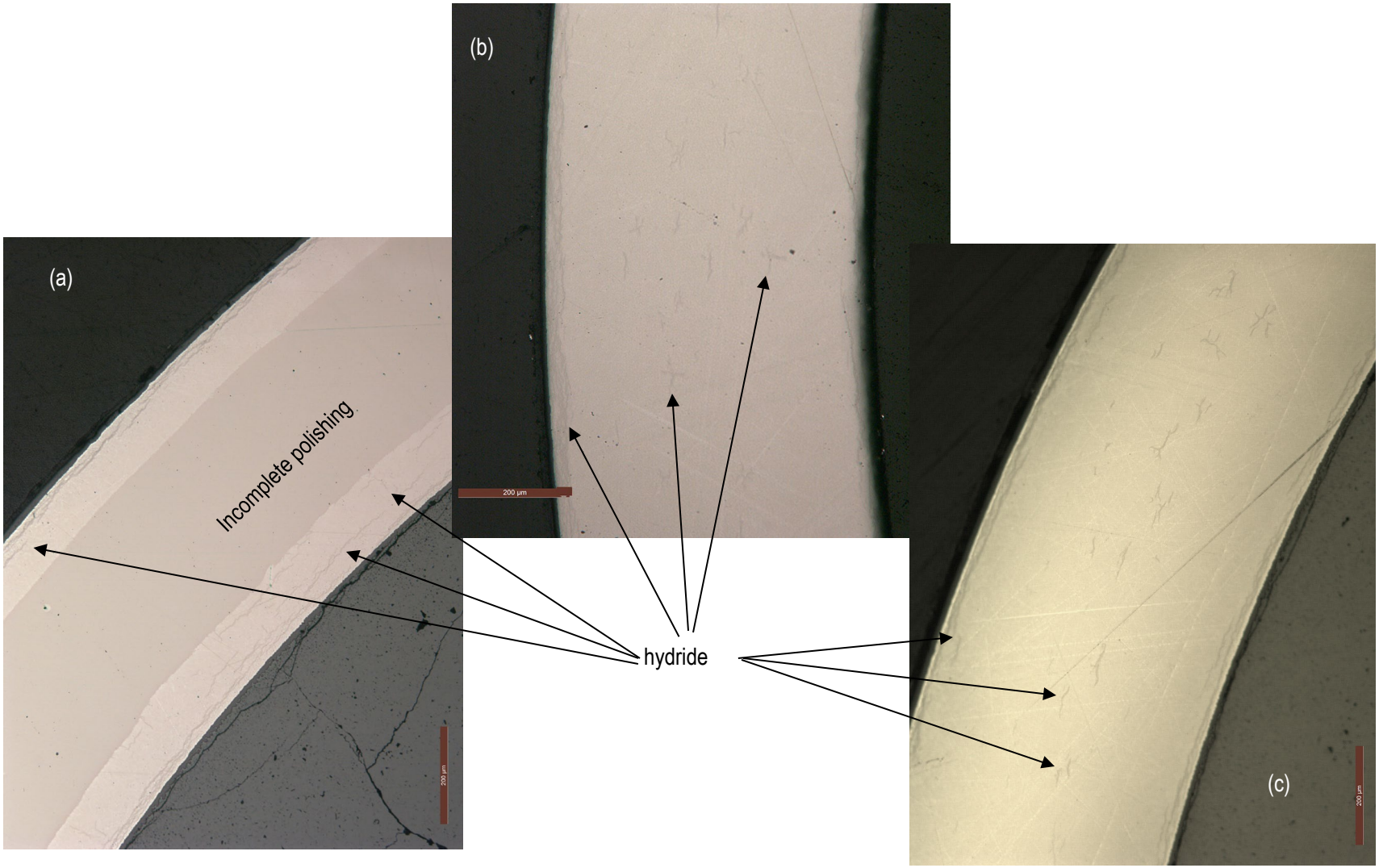

Figure B-46. 3D8E14 centered at 1,403 mm elevation, cladding hydride distribution (a) above the gap in the pellet body, (b) in the gap, and (c) below the gap in the pellet body.

B-3.4 Zirc-4-Clad Sister Rods

Figure B-47 through Figure B-52 provide views of heat-treated Zirc-4 samples prepared from different axial elevations.

Figure B-47 shows an overall view of the sample prepared from 1,300–1,319 mm axial elevation, which is the lowest elevation examined. The figure shows very long circumferential hydrides throughout the thickness of cladding with no pronounced hydride rim. The oxide layer was uniform with no spalling or peeling; however, a few long circumferential cracks were observed in the oxide layer (Figure B-47d) that may be precursors to peeling. No radial hydride was observed at this axial elevation.

At higher axial elevations, noticeable oxide spalling/peeling was observed as shown in Figure B-48 through Figure B-52. Figure B-48 shows an overall view of the sample prepared from F35P17-2383-2402. The hydride rim at this axial elevation was mainly observed near the spalled oxide locations. An example is shown in Figure B-48b in which a thick hydride rim is clearly seen near the spalled oxide location. Moreover, a distinguishable dark region was observed in one quadrant of the sample (see Figure B-48c) which was interpreted as a hydride blister, and several long cracks inside this region extend from the waterside surface through the depth of the blister. No radial hydride was found in this sample. Also, there is a noticeable increase in the circumferential hydride density accompanying the hydride rim and/or where the blister was found.

At 2735-2754 mm axial elevation (Figure B-49 and Figure B-50), a noticeable increase in the circumferential hydride density was observed with the formation of a hydride rim. In this sample, a few short radial hydrides were found. A large portion of the waterside oxide layer is spalled, with an average waterside oxide layer thickness of 81 μm and a maximum thickness of 86 μm at this rod elevation. The spalled layer is almost the full thickness, as shown in Figure B-51, with a ~9 μm layer remaining in the spalled area. The remaining wall thickness in the spalled area is ~510 μm. The pellet cracks are as expected with no missing pellet surface. The average pellet HBU rim is 101 μm on average.

The oxide and hydride morphology at 3,050–3,069 mm axial elevation was similar to that found at 2,735–2,754 mm (see Figure B-52), except that a thicker hydride rim was found.

F35P17 was manufactured by Westinghouse and was used in a lead rod program. It was operated to a rod average burnup of 60 GWd/MTU, and the waterside oxide thickness was previously measured at poolside after reactor discharge [B-9]. The waterside oxide thickness was also measured during the sister rod NDE (before the heat-treatment) using two different instruments, the Electric Power Research Institute's F-SECT system and ORNL's eddy current system. At the elevation of F35P17-2735-2754, F-SECT reported ~90 μm, and the eddy current reported ~100 μm.

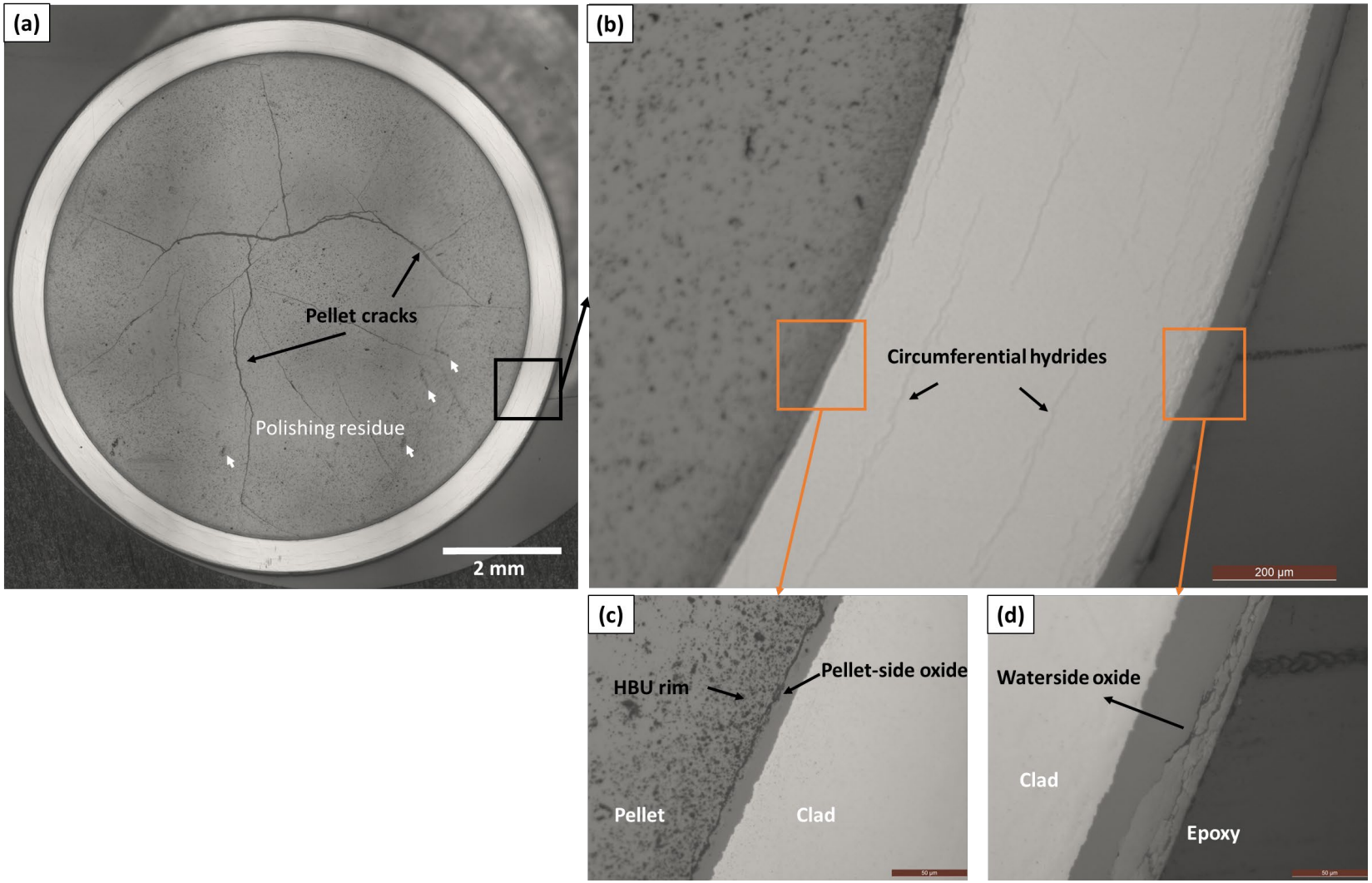

Figure B-47. Views of F35P17-1300-1319 (fueled and unetched heat-treated rod): (a) overall cross-section showing pellet crack morphology, (b) magnified representative image captured from the right quarter of the sample showing circumferential hydrides (scale bar=200 µm), (c) pellet-side oxide and HBU rim (scale bar=50 µm), and (d) waterside oxide layer (scale bar=50 µm).

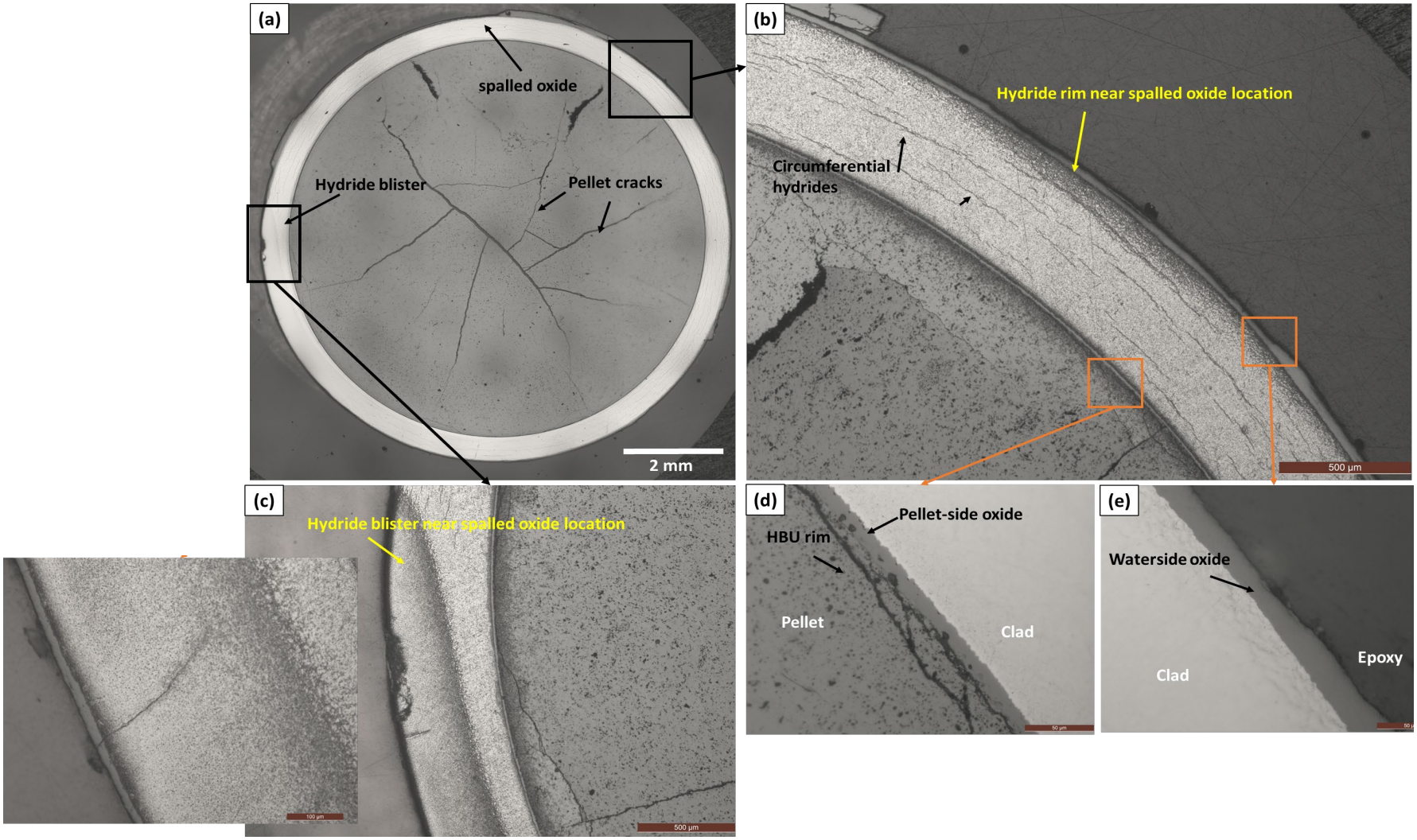

Figure B-48. Views of F35P17-2383-2402 (fueled and etched heat-treated rod): (a) overall cross-section, (b) magnified representative image captured from the right quarter of the sample showing circumferential hydrides and hydride rim which was clearly visible near the spalling oxide (scale bar=500 µm), (c) hydride blister (scale bar=500 µm), (d) pellet-side oxide and HBU rim (scale bar=50 µm), and (e) waterside oxide layer (scale bar=50 µm).

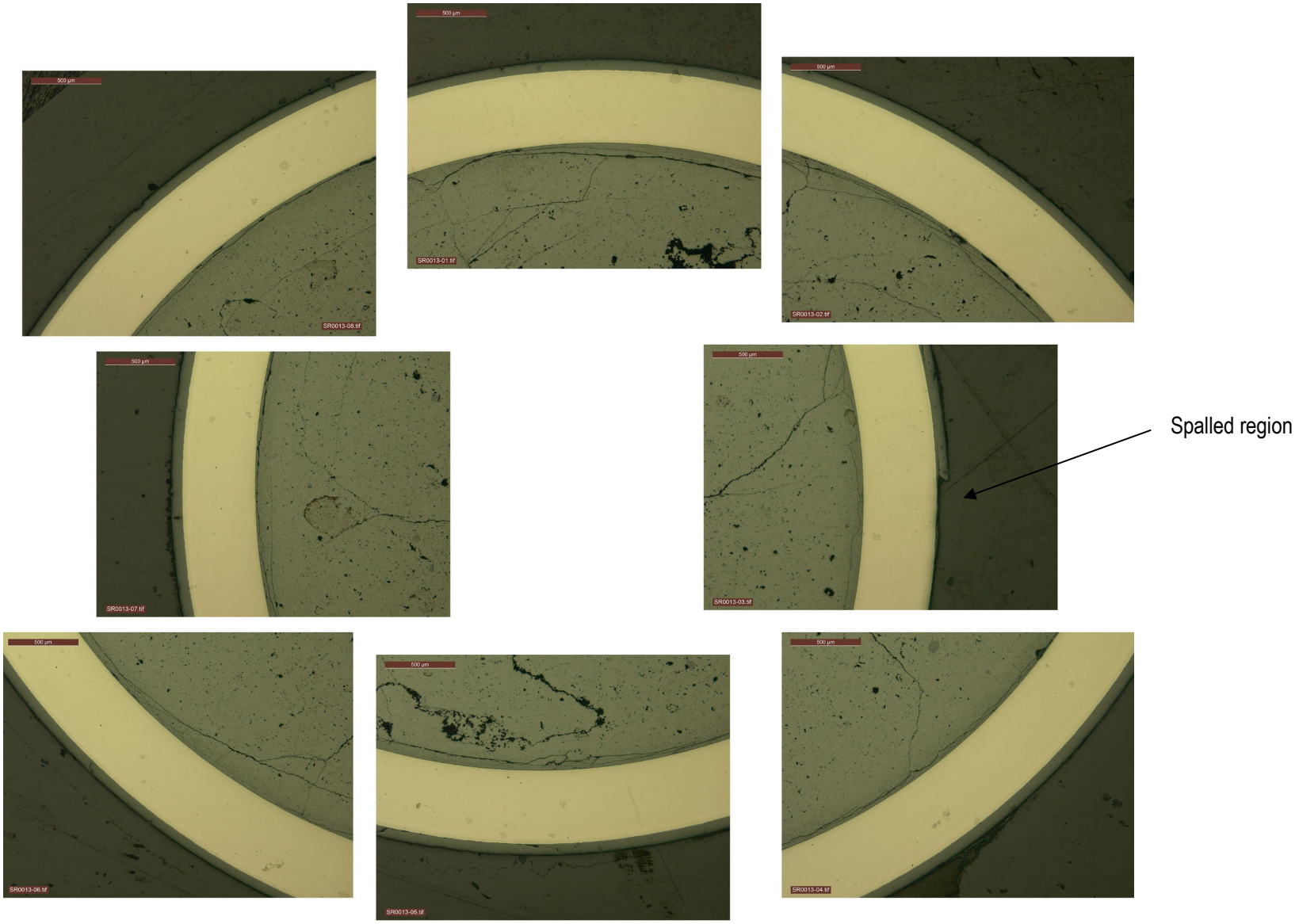

Figure B-49. Mosaic view, fueled, F35P17-2735-2754 (heat-treated).

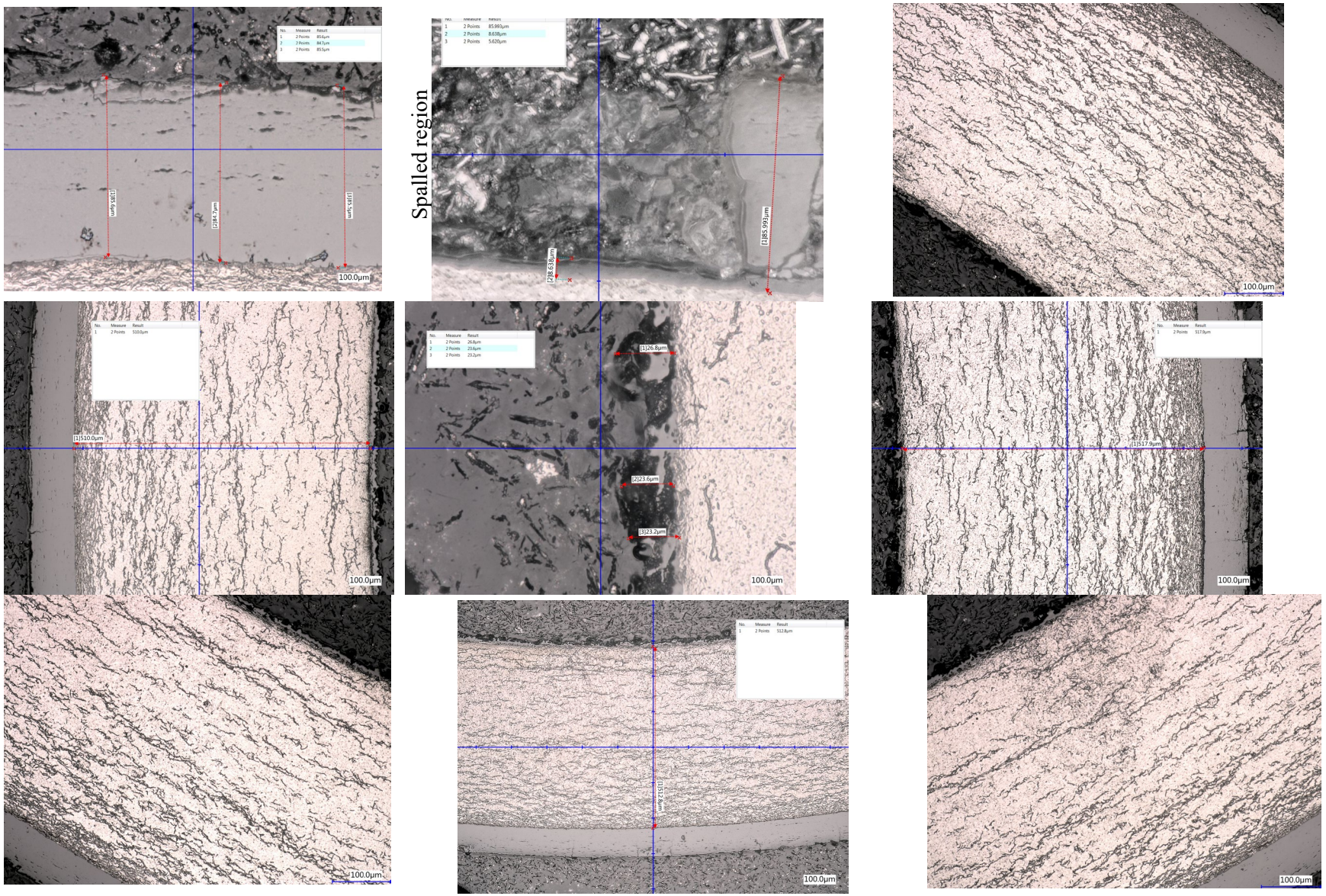

Figure B-50. Magnified views, defueled, F35P17-2735-2754 (heat-treated).

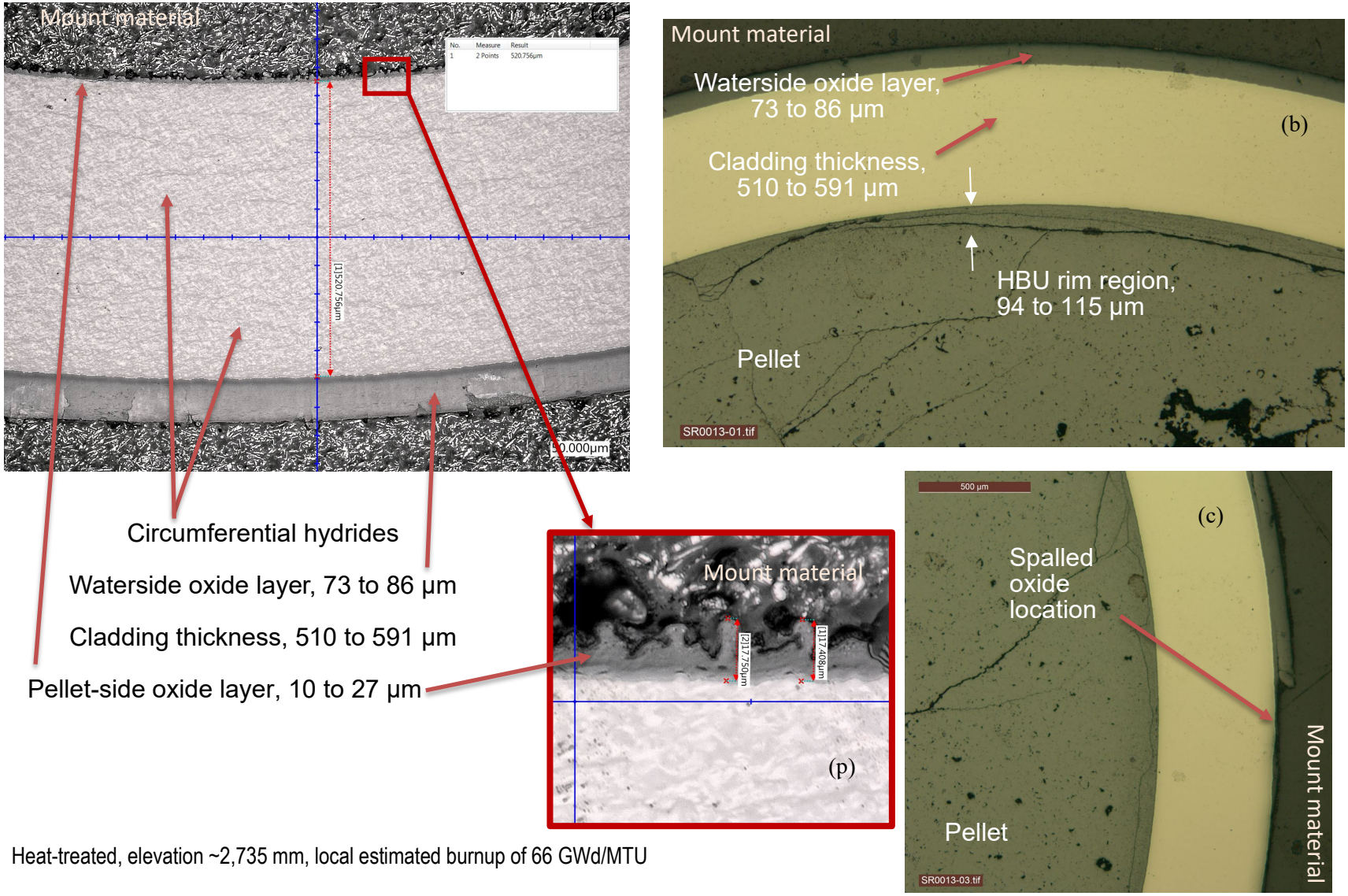

Figure B-51. Selected MET views of heat-treated Zirc-4-clad sister rod F35P17.

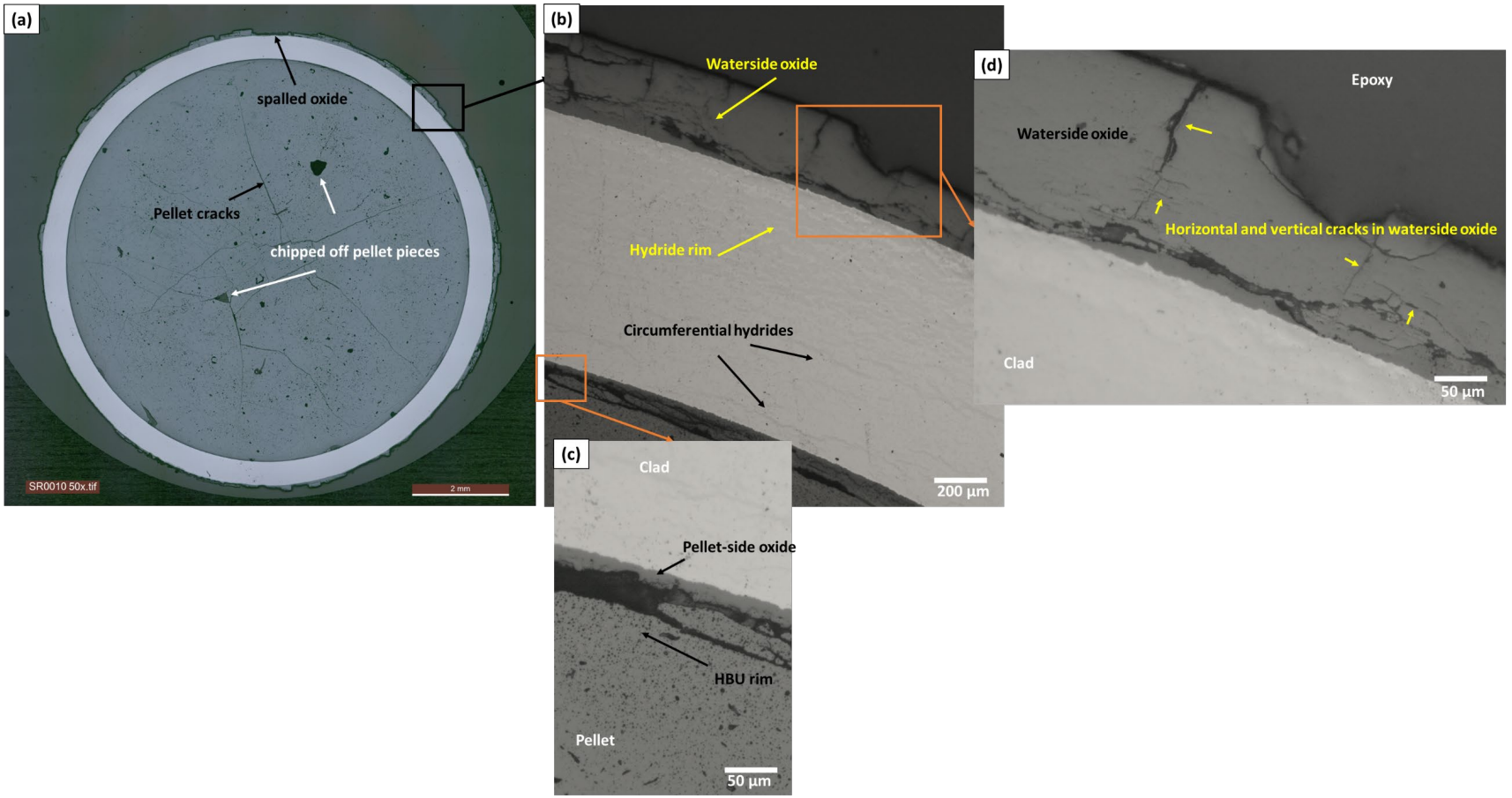

Figure B-52. Views of F35P17-3050-3069 (fueled and unetched heat-treated rod): (a) overall cross-section, scale bar=2mm, (b) magnified representative image captured from the right quarter of the sample showing circumferential hydrides and hydride rim (scale bar=200 µm), (c) pellet-side oxide and HBU rim (scale bar=50 µm), and (e) waterside oxide layer (scale bar=50 µm).

B-3.5 LT Zirc-4-Clad Sister Rods

Figure B-53 through Figure B-59 provide views of LT-Zirc-4 clad rods at different axial elevations. Rod 3A1F05 is a baseline rod that was operated to an average rod burnup of 51 GWd/MTU, as is typical for batch-supplied fuel.

Figure B-53, Figure B-54, and Figure B-55 show a uniform waterside oxide layer with a dense hydride rim on the LT Zirc-4 clad rods at several axial elevations. The hydrides are oriented circumferentially. At 2,383–2,402 mm, a few spalled oxide layer and circumferential cracks in the oxide layer were observed (see Figure B-56b). Further evidence of spalling is visible at 2,754 mm rod elevation, as shown in Figure B-57 and Figure B-58. At the elevations examined, there is a high density of hydrides near the waterside surface of the cladding and a lower density through the remainder of the wall section. Interior hydrides are circumferentially oriented. Figure B-57 shows a possible pellet missing surface at 3A1F05-1585-1604, but there is no evidence that it impacted cladding performance.

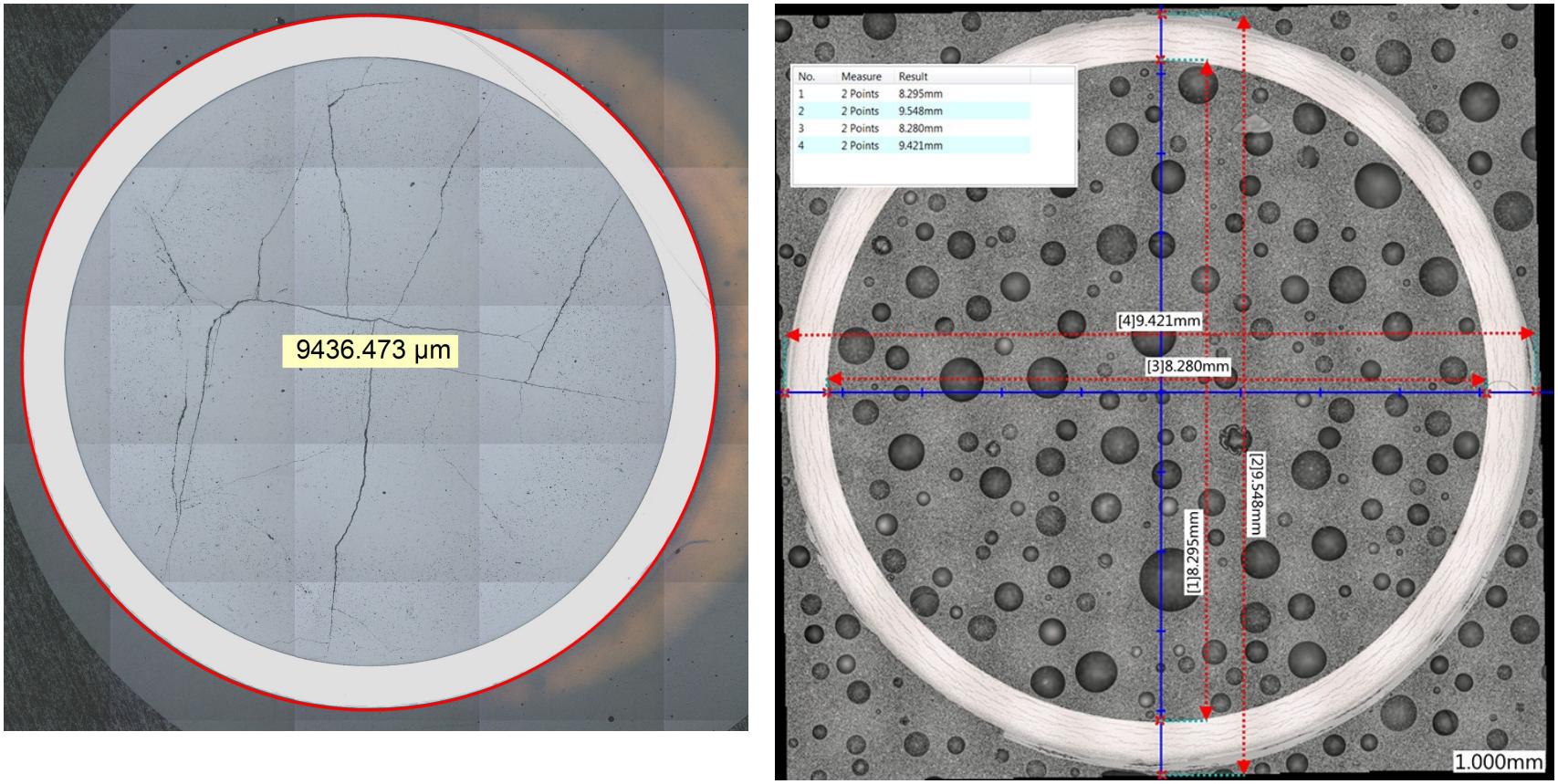

Figure B-53. Fueled overall view of 3A1F05-1260-1279 (left) and 3A1F05-2735-2754 (right) (baseline rod).

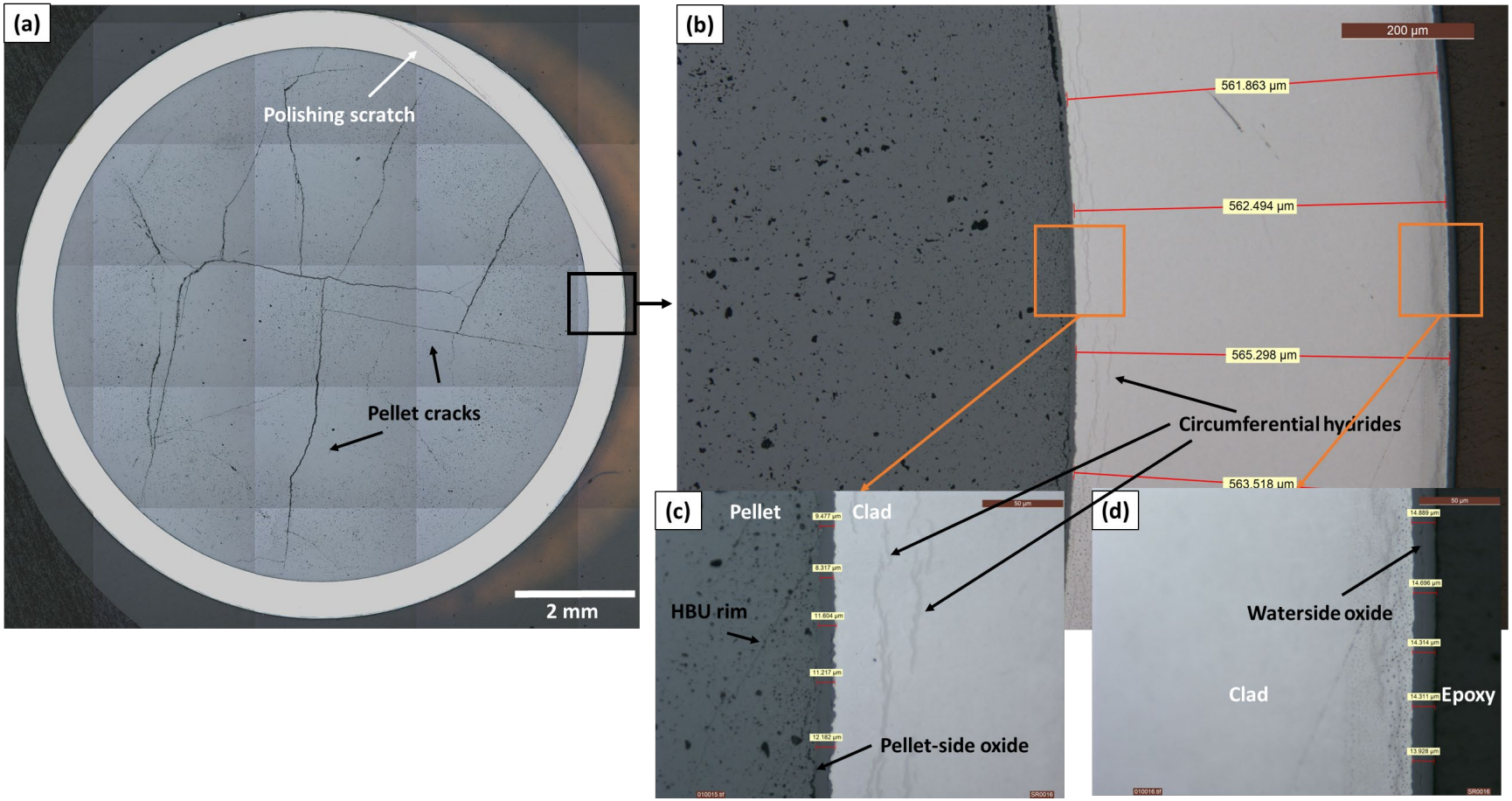

Figure B-54. Views of 3A1F05-1260-1279 (fueled and unetched baseline rod): (a) overall cross-section, scale bar=2mm, (b) magnified representative image captured from the right quarter of the sample showing circumferential hydrides (scale bar=200 µm), (c) pellet-side oxide and HBU rim (scale bar=50 µm), and (d) waterside oxide layer (scale bar=50 µm).

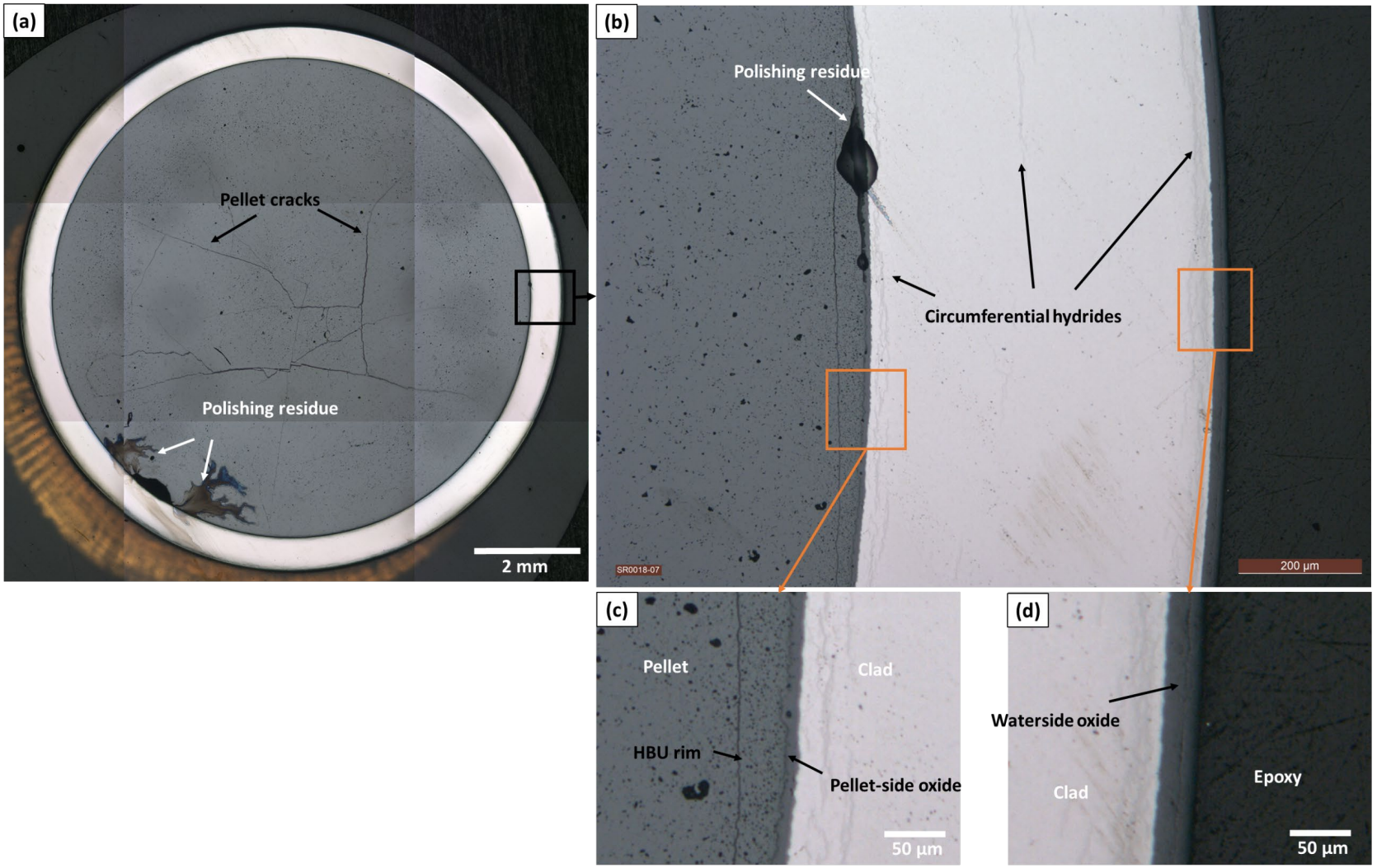

Figure B-55. Views of 3A1F05-1585-1604 (fueled and unetched baseline rod): (a) overall cross-section, scale bar=2mm, (b) magnified representative image captured from the right quarter of the sample showing circumferential hydrides (scale bar=200 µm), (c) pellet-side oxide and HBU rim (scale bar=50 µm), and (d) waterside oxide layer (scale bar=50 µm).

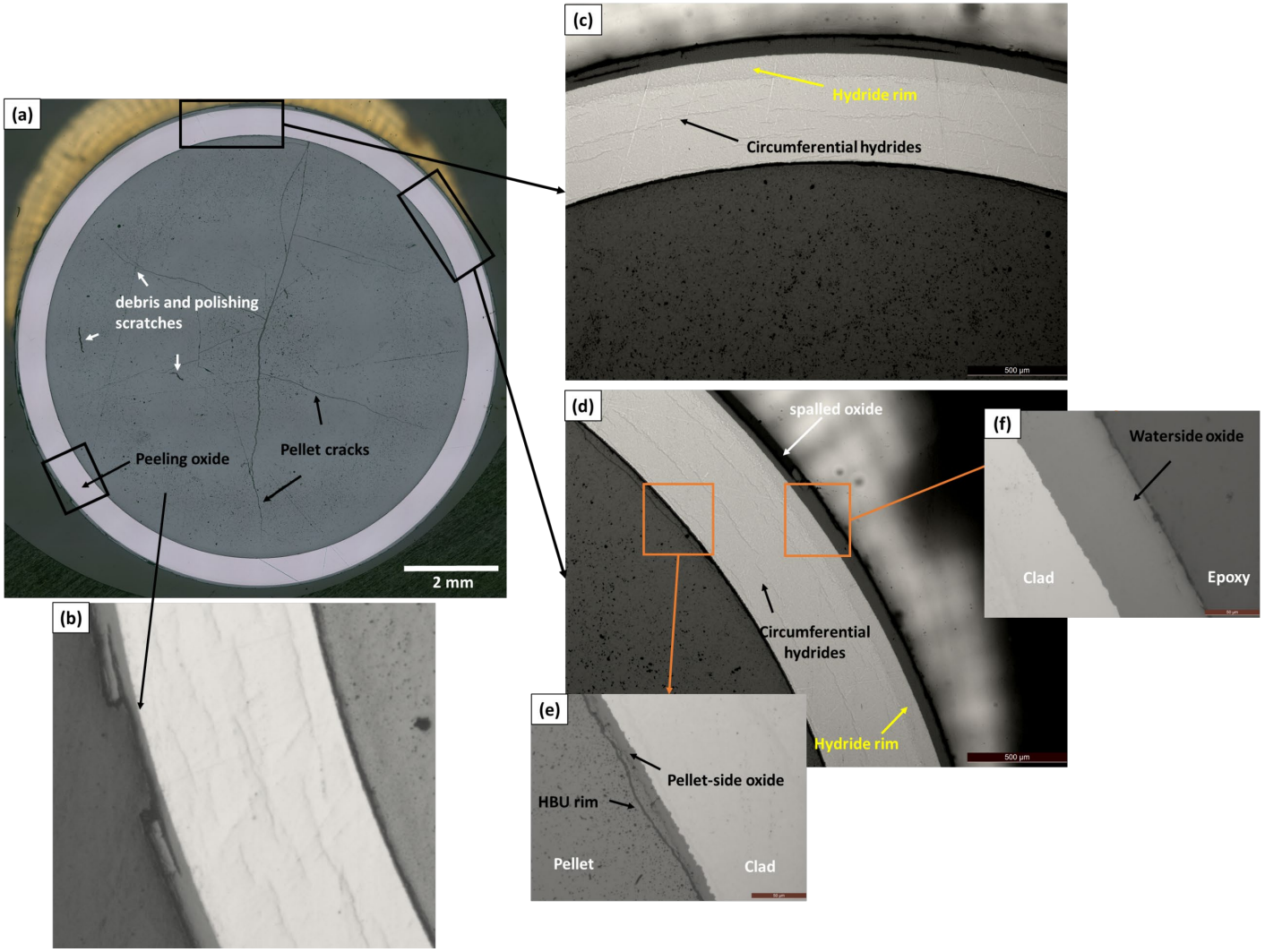

Figure B-56. Views of 3A1F05-2383-2402 (fueled and unetched baseline rod): (a) overall cross-section showing pellet cracks and peeling oxide location in (b), (c-d) magnified image showing circumferential hydrides and hydride rim in the cladding (scale bar=500 µm), (d) pellet-side oxide and HBU rim (scale bar=50 µm), and (e) waterside oxide layer (scale bar=50 µm).

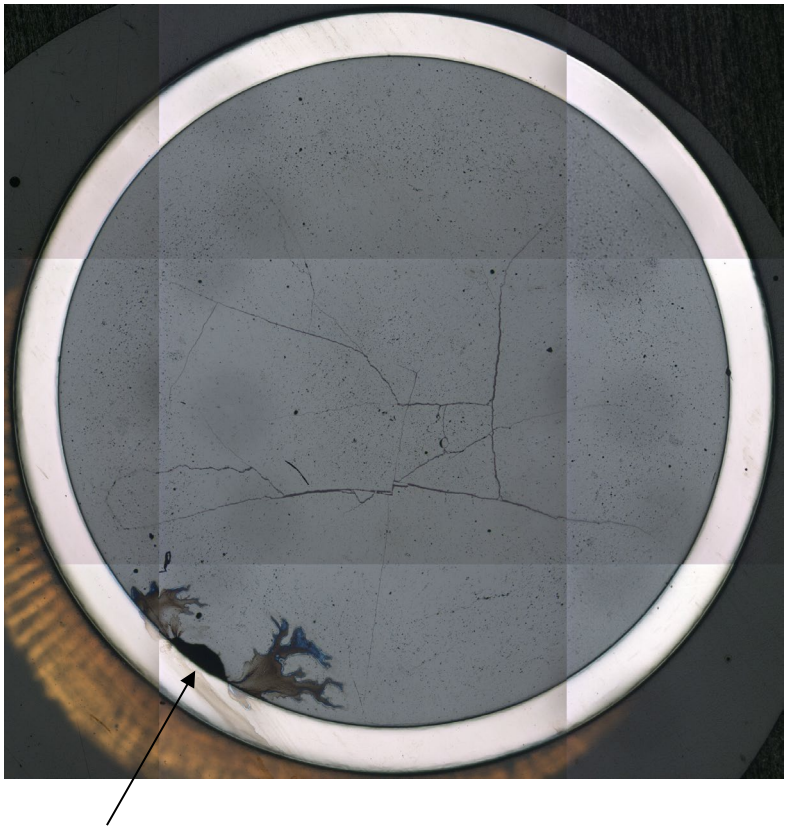

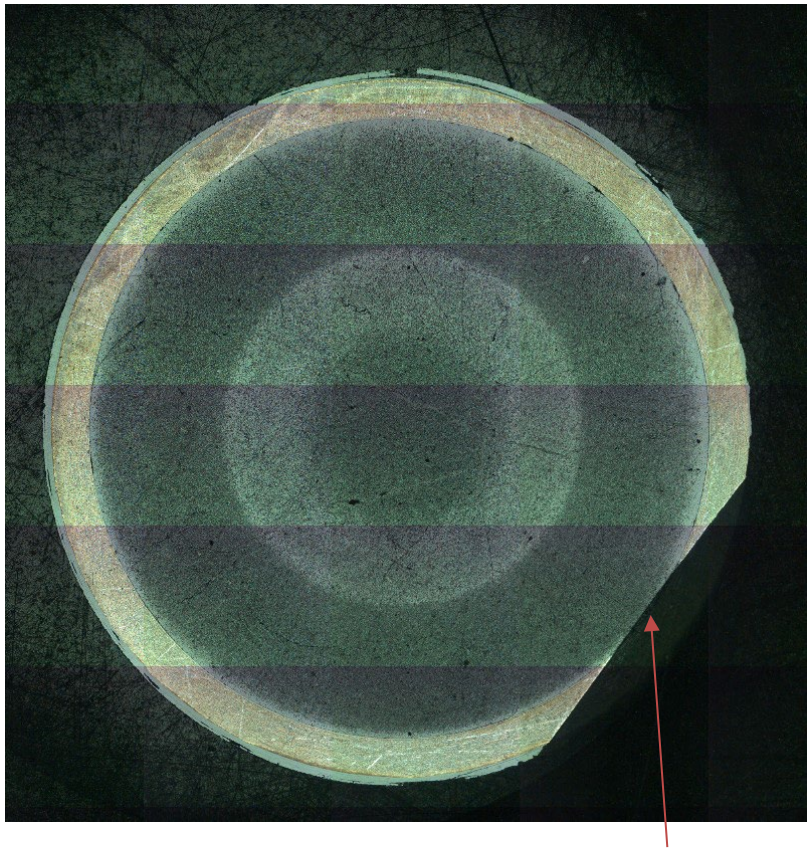

Figure B-57. Fueled overall view of 3A1F05-1585-1604 (left) and 3A1F05-2735-2754 (right) (baseline rod).

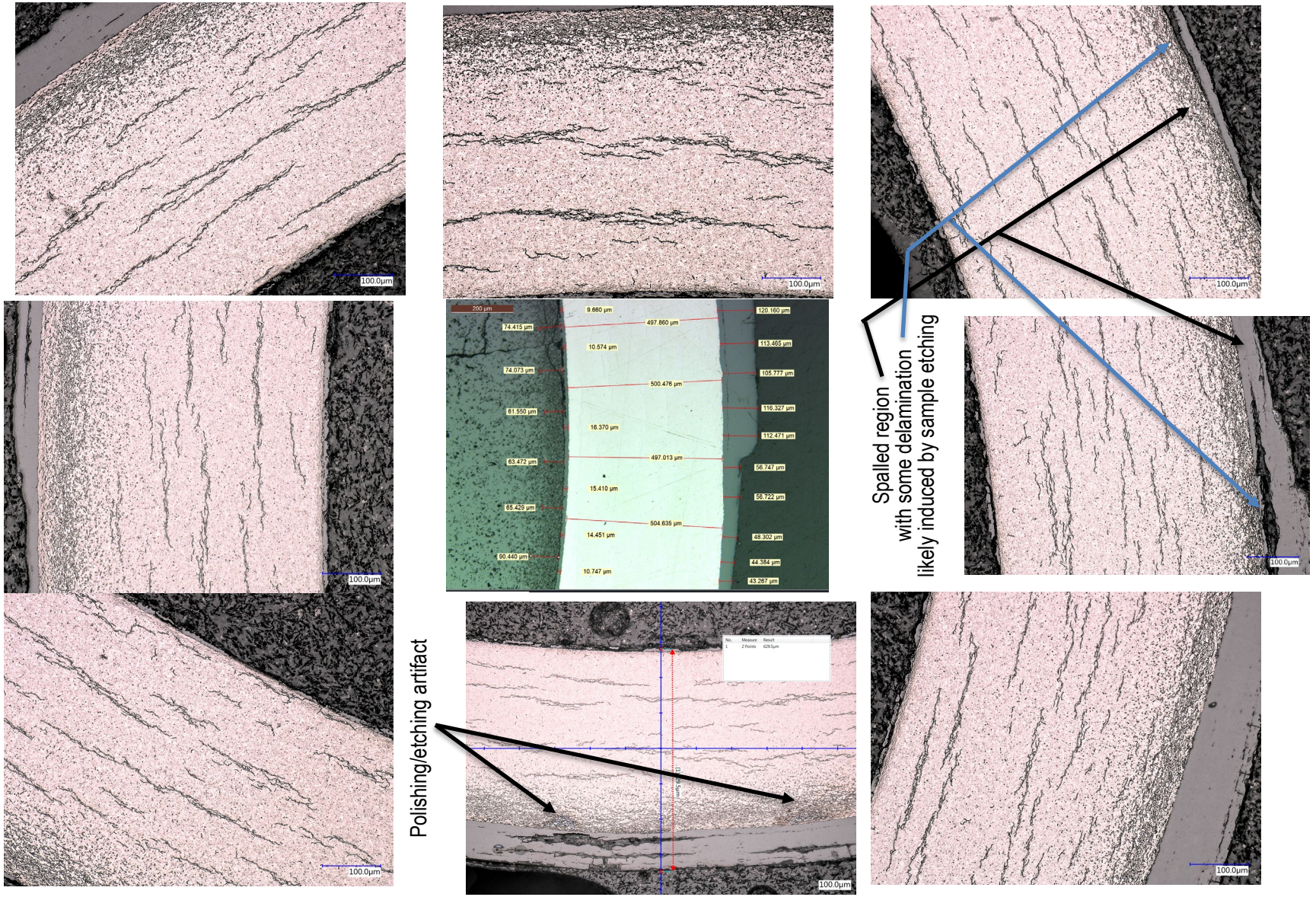

Figure B-58. Magnified views of 3A1F05-2735-2754 (baseline rod).

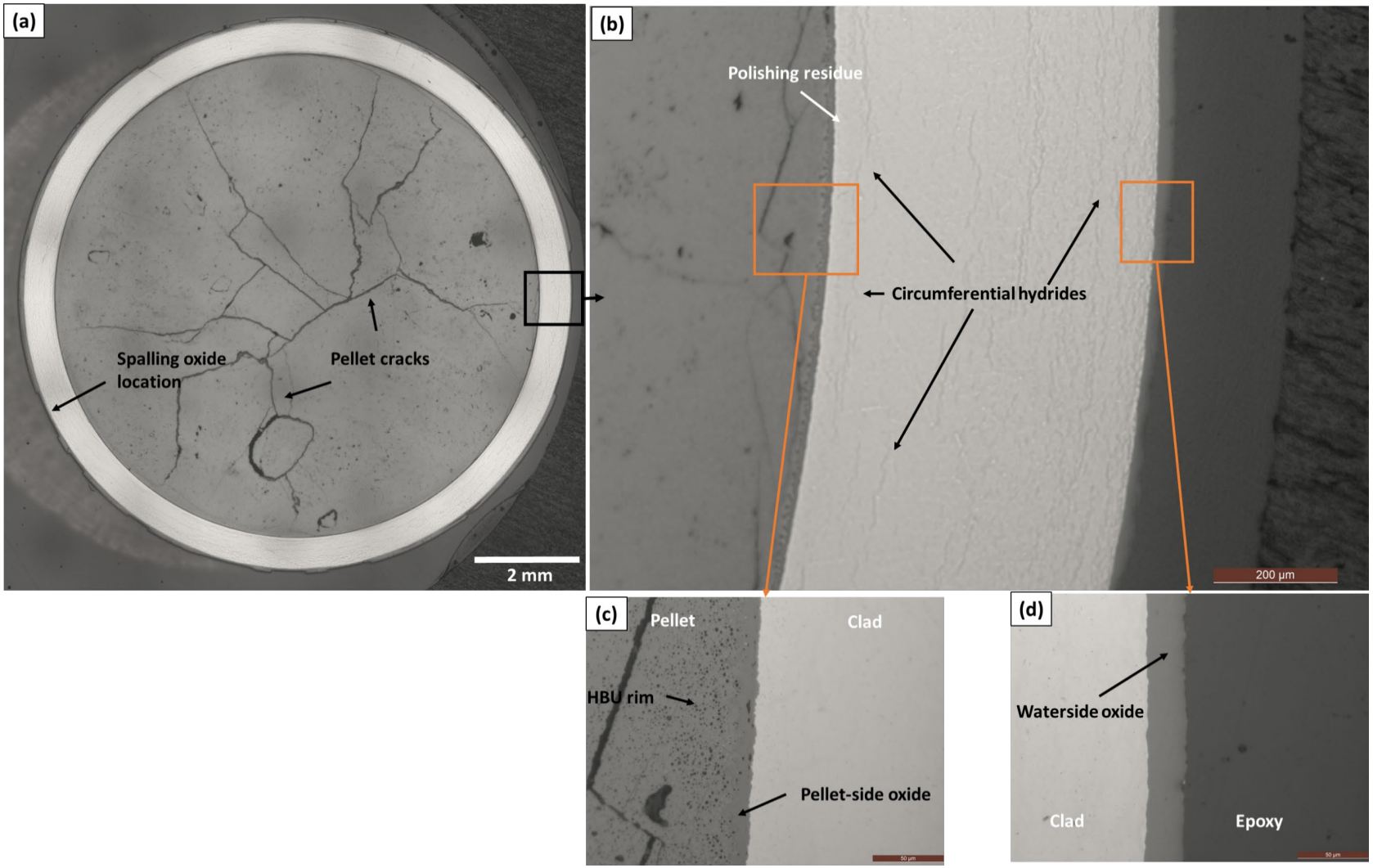

Figure B-59. Views of 3A1F05-3105-3124 (fueled and unetched baseline rod): (a) overall cross-section, scale bar=2mm, (b) magnified representative image captured from the right quarter of the sample showing circumferential hydrides and hydride rim (scale bar=200 µm), (c) pellet-side oxide and HBU rim (scale bar=50 µm), and (d) waterside oxide layer (scale bar=50 µm).

B-3.6 Evidence of Radial Hydrides Nucleated on Pellet Cracks

Several studies (for example, [B-8.] through [B-15.]) have been completed to evaluate the effects of reoriented precipitated hydrides on the integrity of SNF cladding in dry storage. As discussed in Section B-4, SNF rod cladding picks up hydrogen as it oxidizes in reactor. Because the oxidation and hydrogen pickup occur at the waterside surface of the cladding, the concentration of hydrogen is typically larger at the outer circumference of the cladding, but it is well known that hydrogen diffuses under the influence of concentration, thermal, and stress gradients. Hydrogen concentrated above the solubility limit is precipitated as zirconium hydride platelets and, given the texture of the as-fabricated cladding, the platelets are preferentially oriented circumferentially along the longitudinal axis of the rod. Hydride precipitates are brittle relative to the zirconium-based alloy matrix, and precipitated hydrides can change the macroscopic ductility and fracture toughness of the cladding.

In dry storage, given the right combination of temperature and cladding stress, it is possible to re-dissolve the as-discharged precipitated cladding hydrides and then re-precipitate them along the radial direction of the cladding instead of in the circumferential direction, as illustrated in Figure B-3. The direction of the hydride platelets is important because the hydrides themselves are fairly brittle and the interface surfaces with the base zirconium alloy provide convenient planes for cladding fracture. Testing of cladding with reoriented hydrides ([B-8.] through [B-15.]) has demonstrated that, under certain loading conditions, cladding with radially-oriented hydrides demonstrates the characteristics of brittle fracture, even though the base alloy remains ductile.

Most previous ring compression tests were completed using empty cladding tubes (both irradiated and unirradiated). The tubes were pressurized and then subjected to a thermal transient. Because the pellets were not present, the cladding stress distribution was continuous. However, it is known that stress fields affect the precipitation of the hydride platelets, and the stress in the cladding when the pellet is present is varied. Because the ORNL rods are heat treated with the pellets intact, the variations associated with pellet discontinuities are present to influence platelet precipitation.

In earlier metallographic studies (FY19), a hydride was observed that originated at the cladding ID directly adjacent to a pellet crack. This observation has since been validated by other observations within the sister rod collection and also by experiments at other laboratories. Figure B-60 to Figure B-64 provide additional examples of radial hydrides nucleated on pellet cracks for the heat-treated sister rods. To date, we have not observed ID pellet crack nucleated hydrides in the baseline cladding samples and we believe the phenomenon is associated with the cladding stress state in interim dry storage.

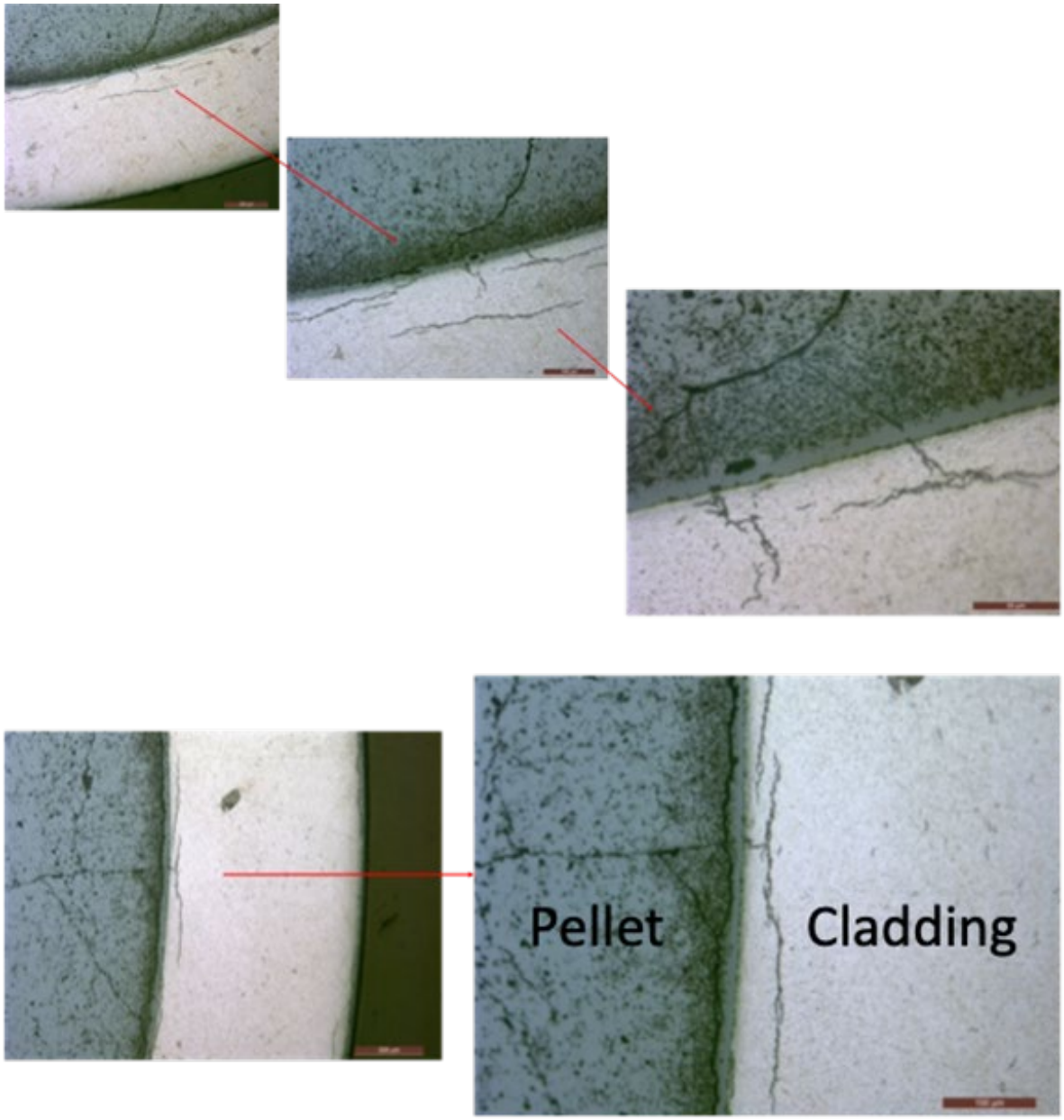

Figure B-60. MET images of sample 3F9N05-0700-0719 showing radial hydrides in conjunction with pellet cracks in three instances.

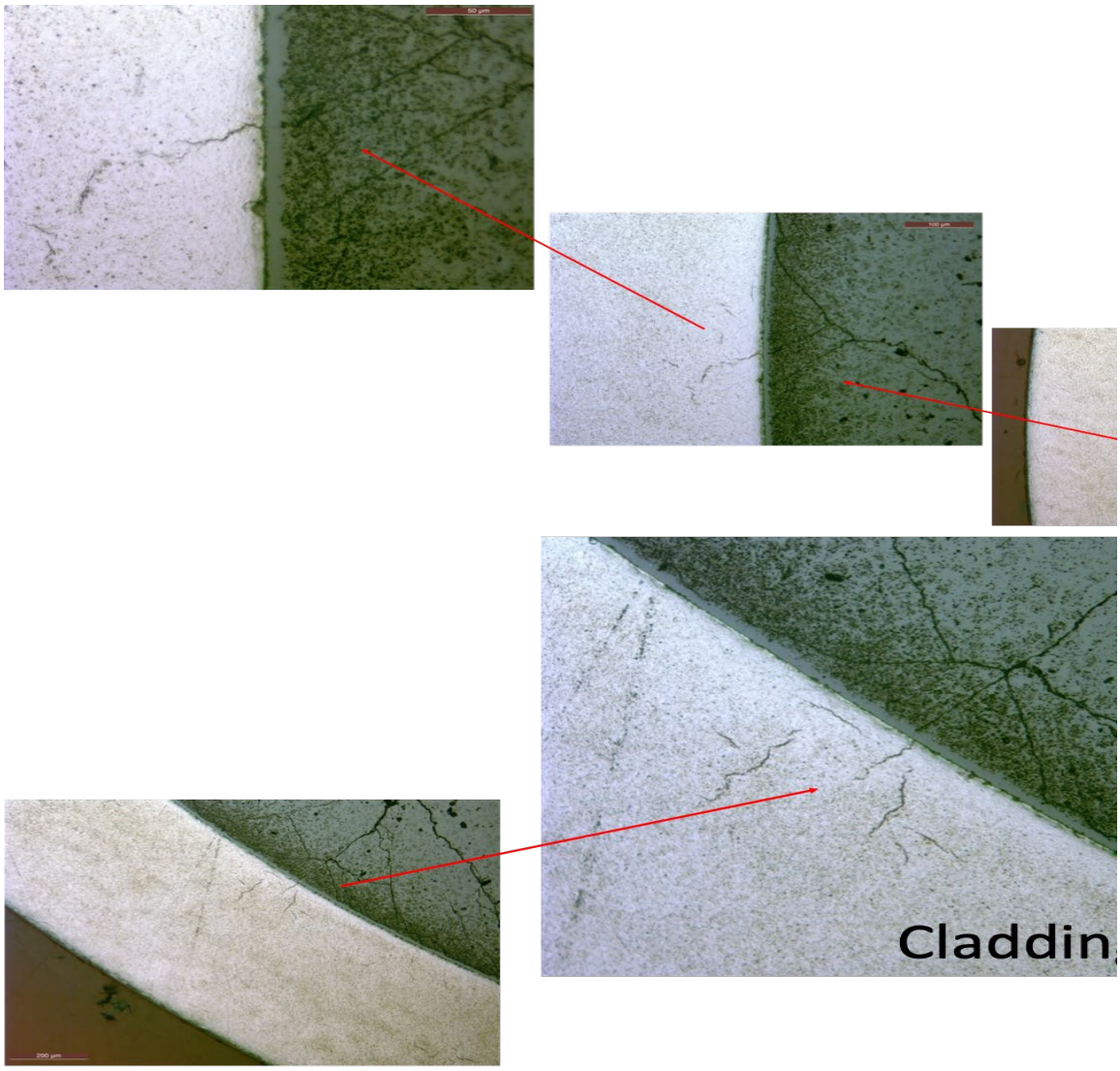

Figure B-61. MET images of sample 30AE14-0653-0672 showing radial hydrides and pellet cracks in conjugation at two instances.

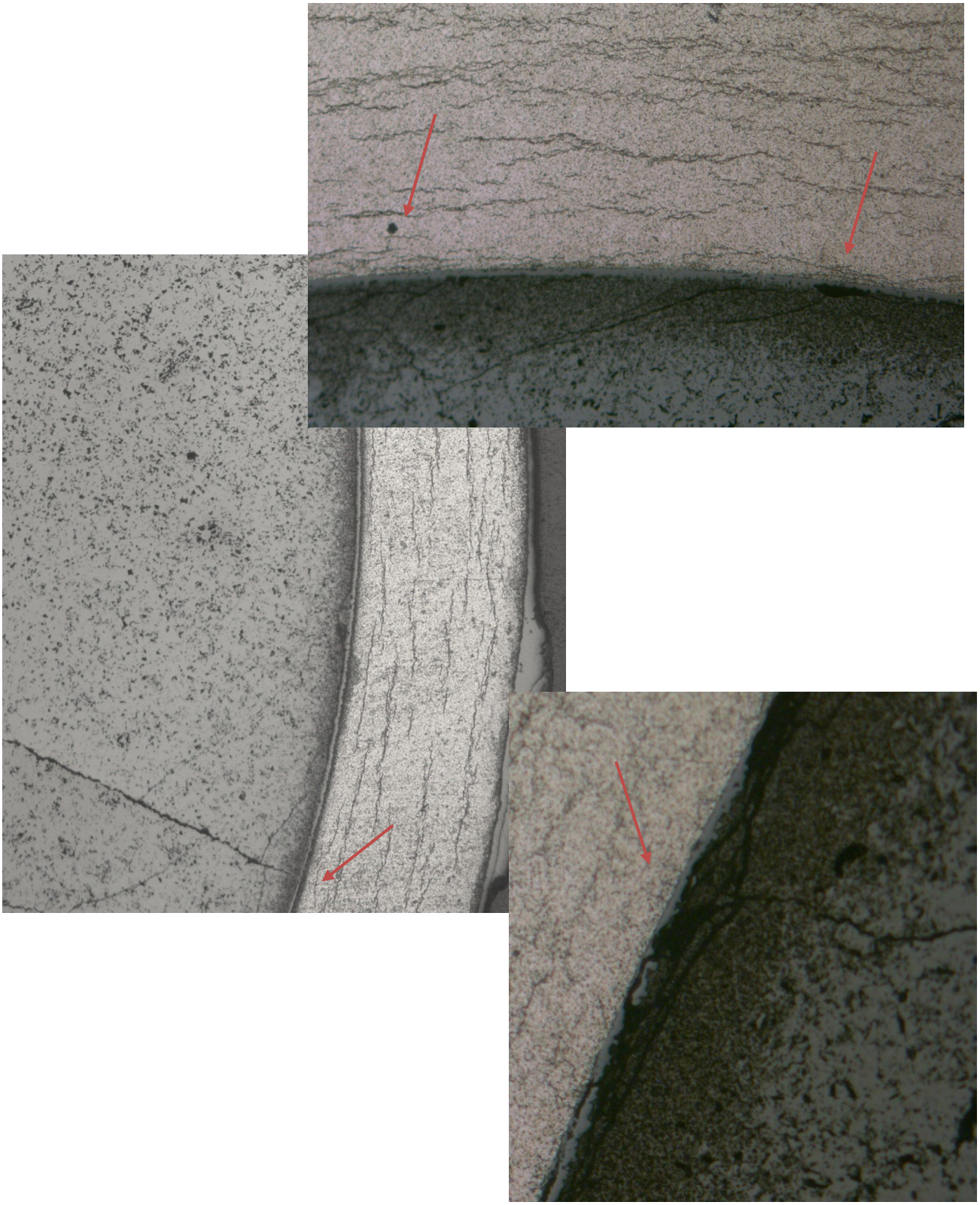

Figure B-62. Section view of heat-treated Zirc-4-clad rod F35P17 showing few reoriented hydrides and hydrides at ID nucleated at pellet crack.

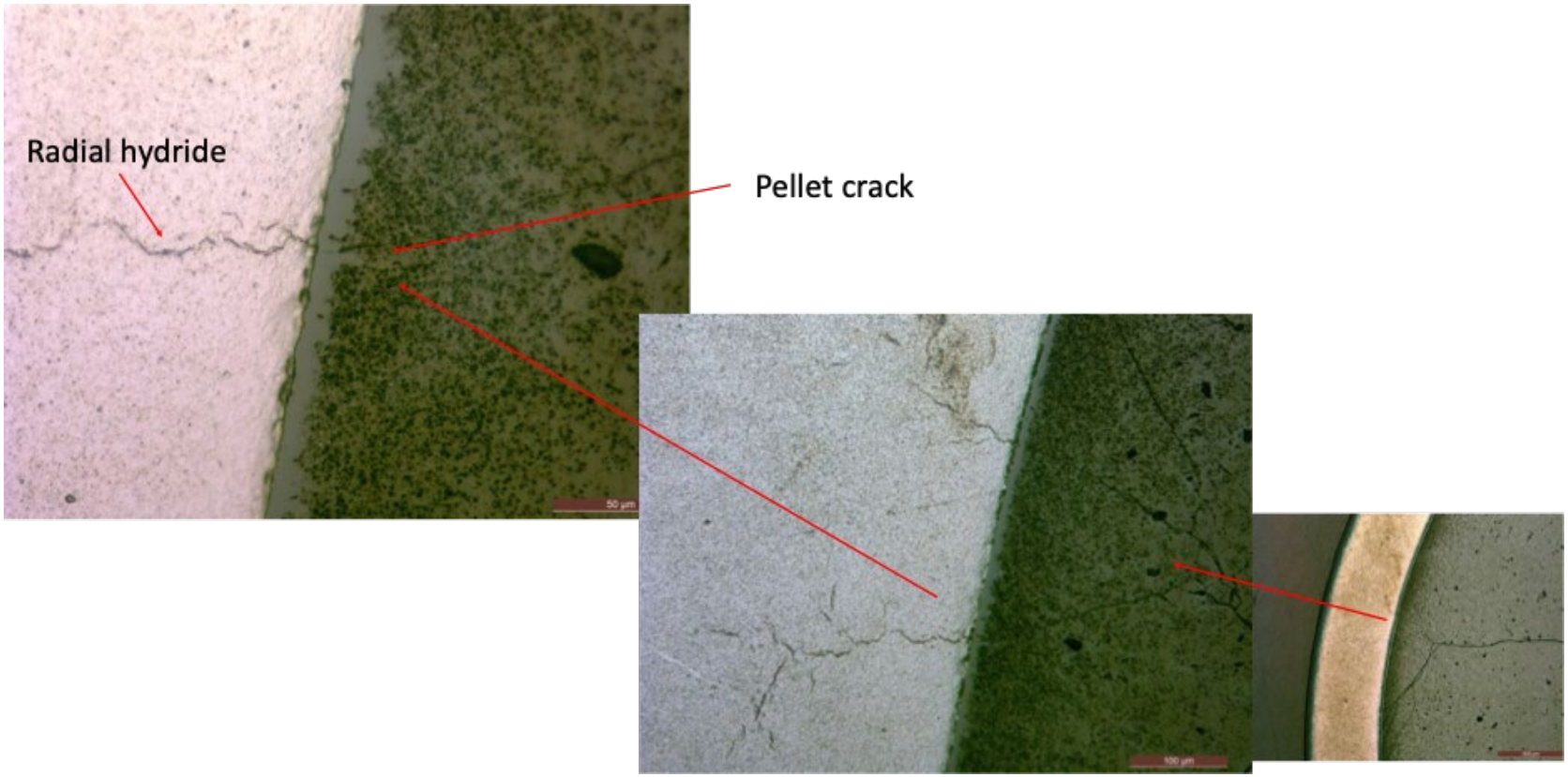

Figure B-63. MET images of sample 30AE14-1677-1696 showing radial hydrides in conjunction with pellet cracks

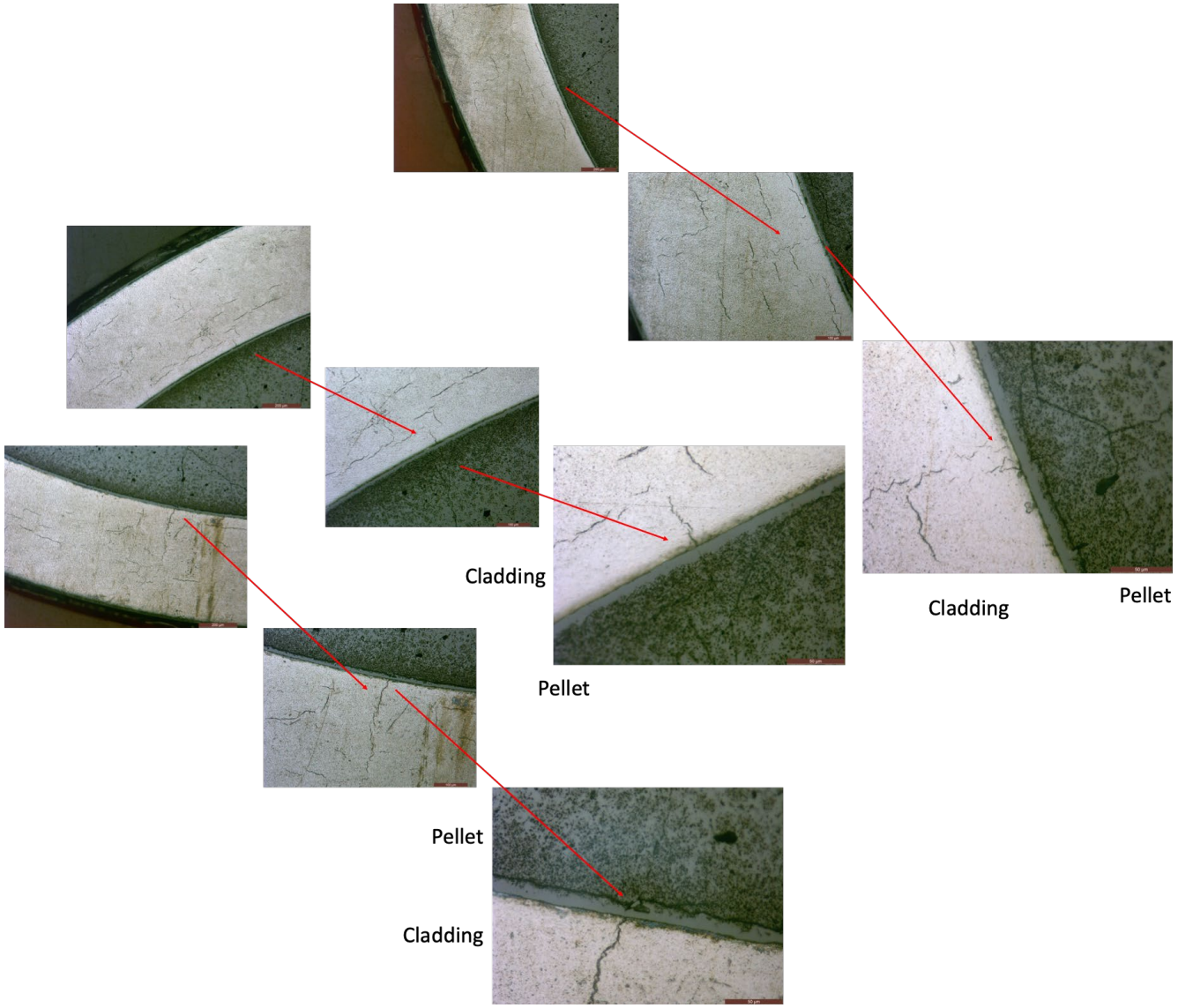

Figure B-64. Met images of sample 30AE14-2203-2222 showing three examples of radial hydrides nucleated at pellet cracks.

B-3.7 Waterside-oxide thickness calculation for spalled/non-uniform oxide fuel samples using image processing and analysis

MET images of samples with non-uniform waterside-oxide thicknesses were post-processed using ImageJ to accurately calculate the thickness [B-16.] . The analysis involved estimating the overall area of waterside-oxide layer on a cladding sample and estimating an average thickness by assuming this layer to be uniformly present around the circumference of the sample.

The analysis was conducted using the Trainable WEKA Segmentation plugin on FIJI (ImageJ) to identify and segment the different layers in a MET image (oxide, cladding and pellet) [B-17.] . The plugin works by training WEKA, a collection of machine learning algorithms [B-18.] , with a set of user-defined image features to produce pixel-based segmentations (Figure B-65). The first step involved selecting individual features on an input MET image and labeling it as separate classes for training (Figure B-66). Once the training process ends, the displayed image is completely segmented, and the result is overlaid with separate colors denoting the corresponding class. The training step was then iterated until the displayed image was correctly segmented and the results overlaid with the corresponding class colors. Some samples required additional features to be specified under a class before the training was re-iterated as there were some overlaps in the classes. Once, the training and segmentation were complete, individual probability maps were generated to isolate the different features. The probability maps were refined further by thresholding and in some instances, additional post processing was done including despeckle, erosion and dilation processes on the binary image. The area of the oxide layer was then measured either by particle analysis or direct measurement sets to obtain the total oxide layer area around the cladding.

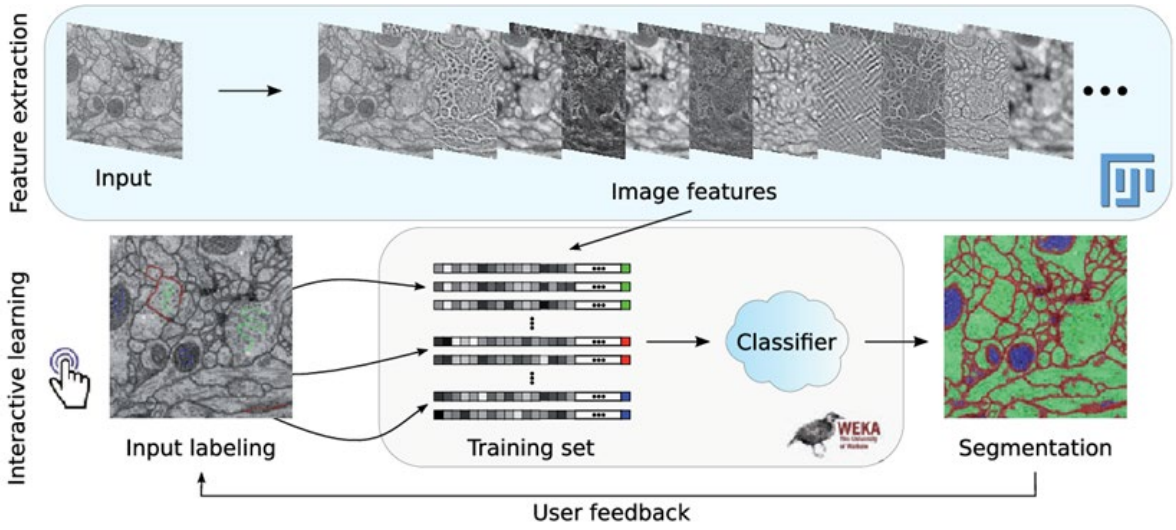

Figure B-65. TWS pipeline for pixel classification from Arganda-Carreras et al. [2].

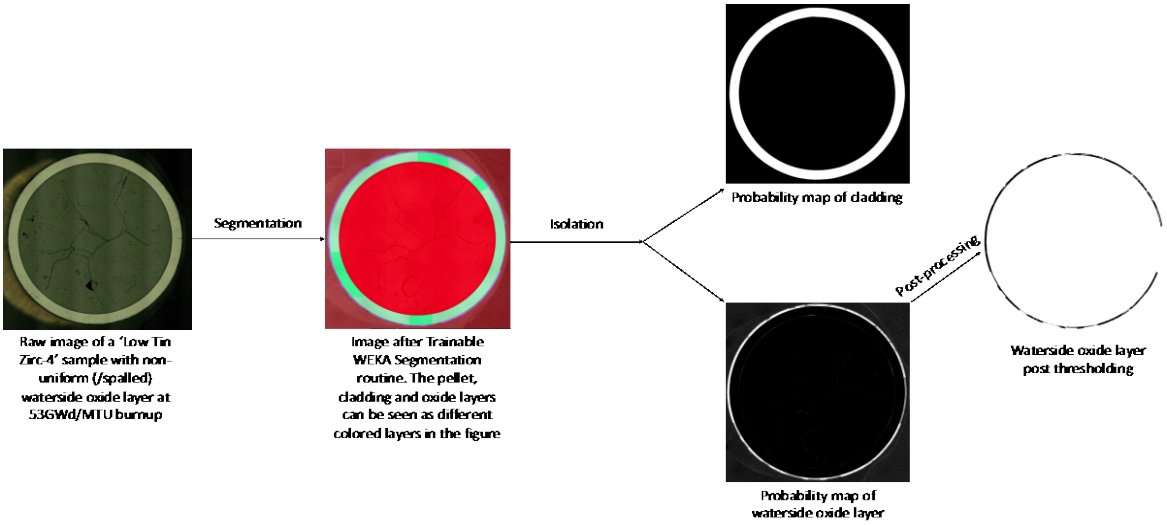

Figure B-66. General workflow adopted for calculating the average non-uniform oxide layer thickness using FIJI.

Once the total area of the oxide layer on a sample was obtained, an imaginary layer of the same area is assumed to be present uniformly around the sample OD and an associated thickness for this imaginary layer was calculated. This thickness is specified as the average oxide layer thickness for the samples presented in Table B-7. Future refinements should include identifying spalled oxide layers and quantifying the percentage of the circumference affected.

Table B-7. Average waterside oxide layer thickness calculated from FIJI image analysis compared with MET measurements of the same specimen.

Specimen ID	Waterside oxide thickness from direct MET measurements (μm)	Average waterside oxide thickness from FIJI analysis (μm)
30AD05–2410–2429	5 to 41, 24 average	16
3D8E14–3206–3225	24 to 57, 47 average	40
3A1F05–2383–2402	52 to 89, 70 average	56
3A1F05–2735–2754	43 to 128, 94 average	48
3A1F05–3105–3124	27 to 98, 75 average	67
F35P17–2383–2402	8 to 146, 47 average (spalled)	83
F35P17–3050–3069	8 to 173, 93 average (spalled)	56

MET images of fuel and cladding are complex due to the number of features present in an image. Another feature of interest in this study was the hydride concentration and the movement of precipitated hydrides from heat-treatment. Hydrides are seen to precipitate along the cladding, seen as long black strands on the cladding surface. The characterization of hydrides in the cladding is often slow and cumbersome due to their long lengths and short widths, requiring low magnification and hence much more noise to resolve. An attempt was made to semi-automatically analyze circumferential hydrides by training a WEKA segmentation model on ImageJ. Sample 3A1F05-2383-2402 was chosen for this analysis due to high presence of uniformly precipitated circumferential hydrides in the LT-Zirc4 cladding. The uniform distribution means that the hydride density at one quadrant could be scaled for the entire sample with some

certainty. Figure B-67 shows the WEKA segmented MET image from a quadrant of sample 3A1F05-2383-2402. The segmentation was performed using the same techniques.

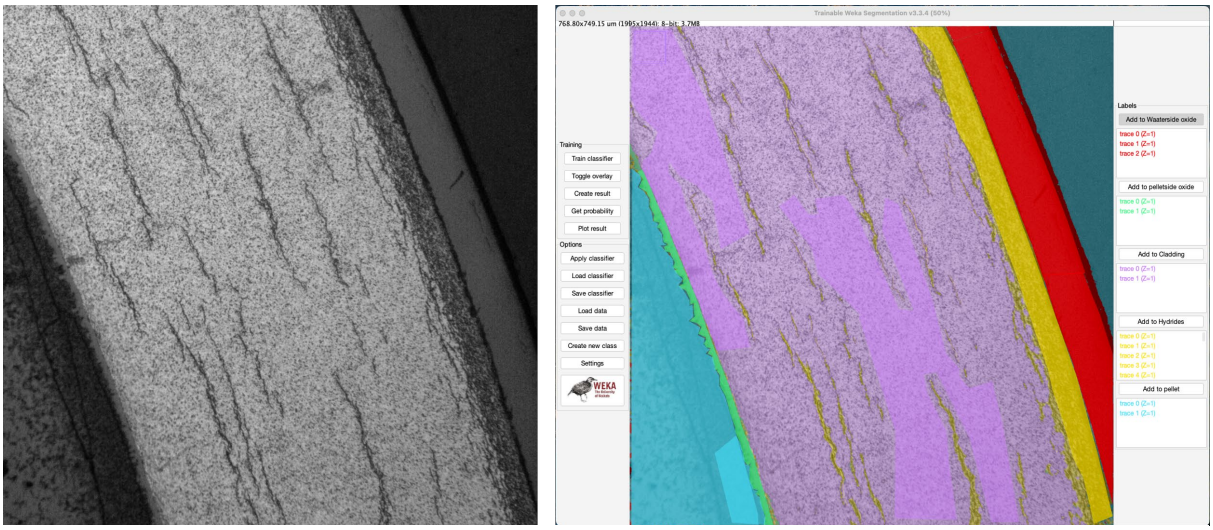

Figure B-67. WEKA segmented MET image of sample 3A1F05-2383-2402 showing different features identified in the (trained) model.

Once the image was segmented to identify the hydrides in the cladding, a probability map of the hydrides and the cladding area were isolated (as seen in Figure B-68 and Figure B-69). These maps were processed (by thresholding and other operations subject to image performance) to calculate the total area of hydrides and the total area of cladding (without the hydrides).

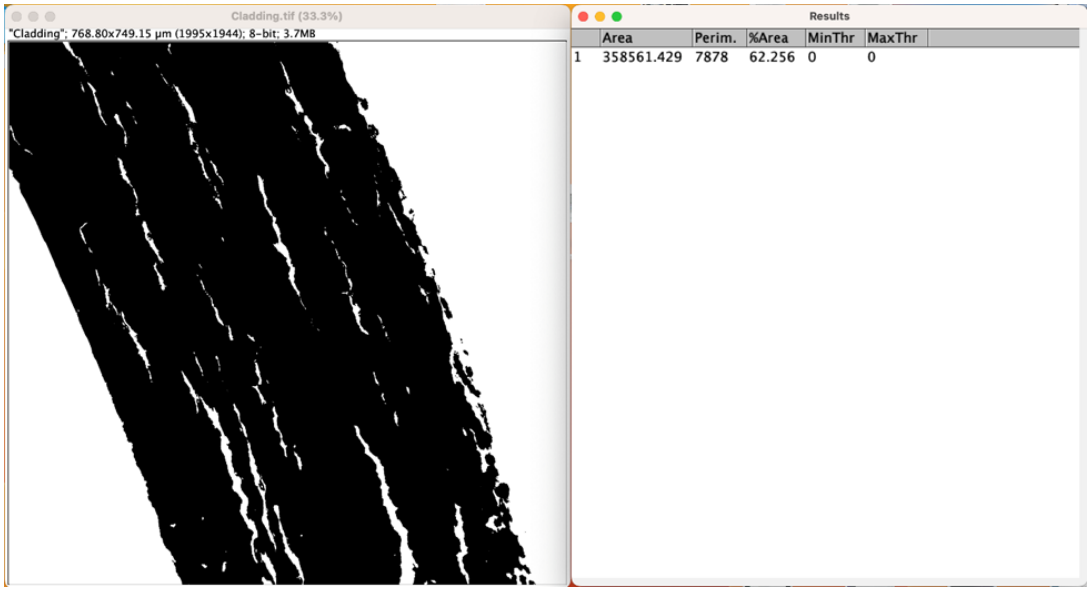

Figure B-68. Post-processed probability map of the cladding (without hydrides) in the MET image of sample 3A1F05-2383-2402 shown in Figure 21.

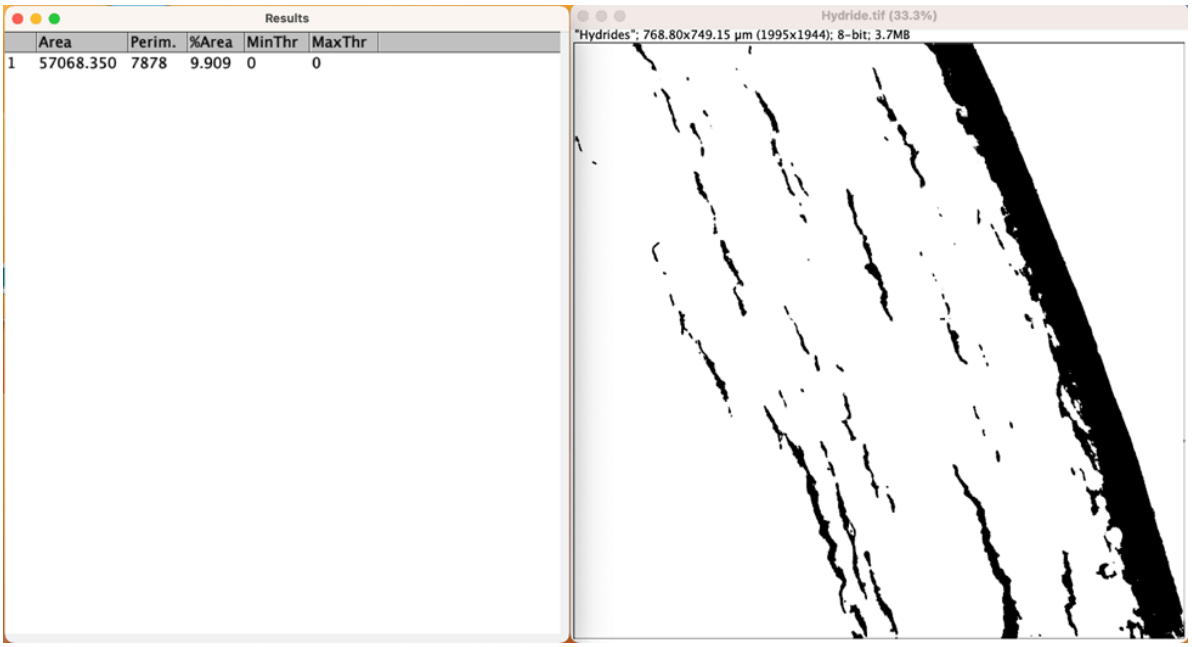

Figure B-69. Post-processed probability map of the hydrides in the MET image of sample 3A1F05-2383-2402 shown in Figure B-68.

The hydride density per cladding area can then be calculated as:

$$Hydride\ areal\ density = \frac{Total\ area\ of\ hydrides}{Total\ area\ of\ cladding\ (along\ with\ the\ hydrides)}\ x\ 100$$

Thus, the hydride areal density for the MET image in Figure B-69 was calculated as 14%. Better accuracies can be expected from better model training in FIJI. Future work will also expand on this approach to characterize larger MET image areas and full-size mosaics for calculating the hydride densities in samples with non-uniformly distributed hydrides.

Lastly, as discussed previously, certain assumptions were made during the manual measurements taken on the MET images. This includes simple errors like measuring through or missing a pixel while measuring/scaling a MET image to more complex errors such as the researcher's perception of certain features like the HBU rim and being more conventional in the measurements. Such errors can be avoided by bringing in intelligent measurement techniques using artificial intelligence/machine learning models to statistically identify features from a raw image. Such an approach will also quicken the analysis time while characterizing multiple images and samples.

It should be noted that there are also sources of error associated with the processing of the metallographic specimen and the specimen imaging. The apparent width of hydrides depends on the imaging technique (optical microscopy vs. SEM), the composition of the etchant, the etching time, and, to some extent, the total hydrogen content. Optical microscopy tends to exaggerate the width of hydrides. Over-etching also exaggerates the hydride width. Given these variables, it is likely that these estimates are an upper bound of the hydride width.

B-4. CLADDING HYDROGEN MEASUREMENTS (DE.03)

Table B-3 lists the segments that are planned to be used as cladding total hydrogen specimens. All planned phase 1 tests have been completed.

B-4.1 Specimen Processing

As shown in Figure B-70, each specimen was cut from the parent segment using a slow speed saw; then each specimen was subsectioned to provide an azimuthal sample for each quadrant (0, 90, 180, and 270°). Although the quadrants are not traceable to the position in the reactor, the azimuthal measurements can provide some indications of variations in cladding hydrogen content resulting from in-reactor temperature differences around the rod's circumference. The oxide layers are not removed from the cladding prior to oxygen nitrogen hydrogen (ONH) measurement.

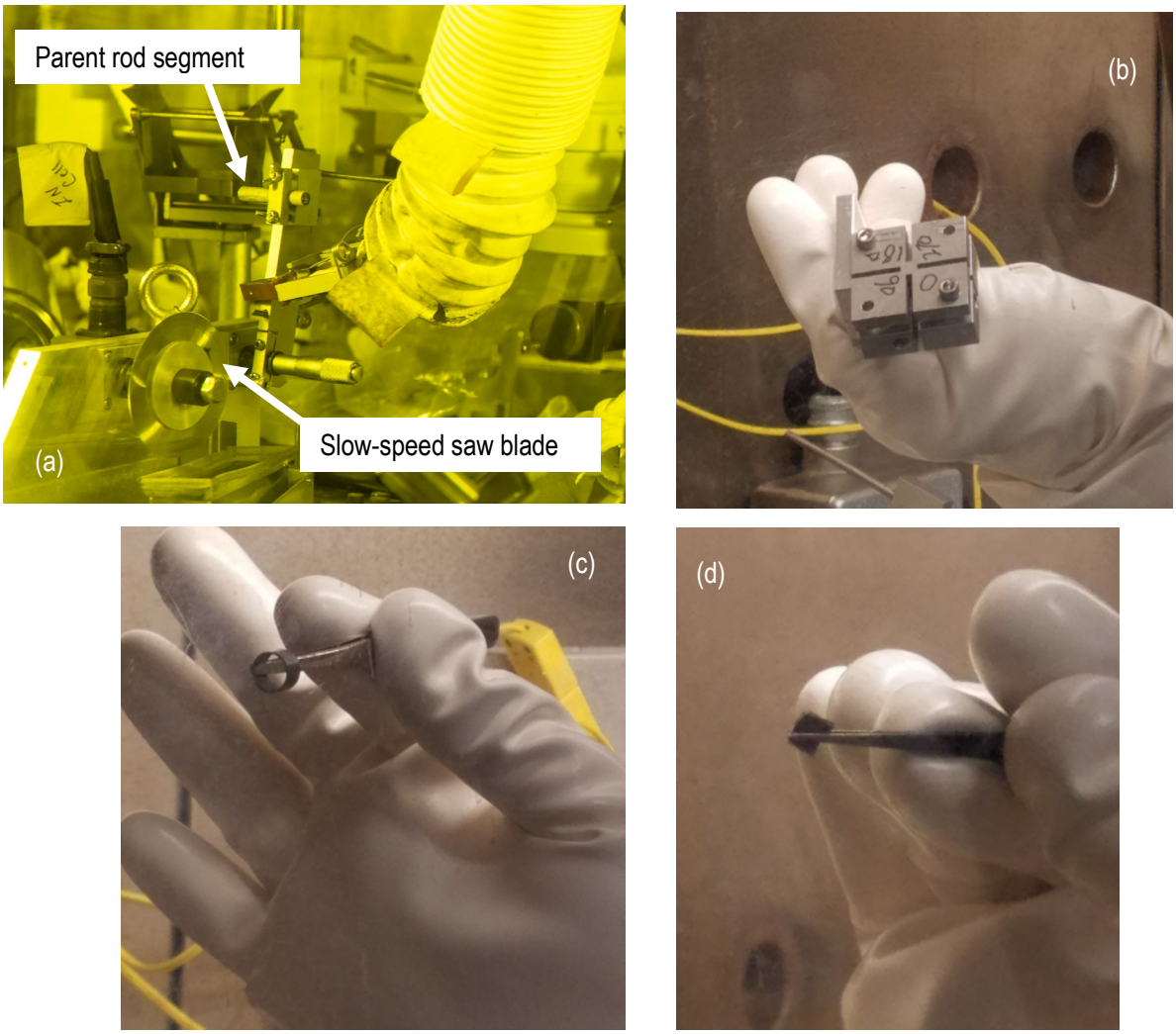

Figure B-70. (a) A parent rod segment mounted in the slow-speed saw in the main hot cell, (b) a bottom view of the fixture used to quarter the 4 mm long defueled cladding specimen, (c) view of the cladding specimen before quartering, and (d) the resulting quadrant sample for LECO ONH measurements.

B-4.2 Analyzer Setup

The LECO Model 836 was placed in a custom enclosure with several glove-ports within the existing IFEL Greenhouse. A second enclosure was placed over the LECO transfer port to reduce the potential for contamination during cleaning. Experience with the system showed that the contamination levels were high enough that these enclosures are necessary for adequate contamination control with periodic decontamination of the equipment. The equipment continues to work well with the added enclosures, and no major equipment issues or events have occurred.

The LECO Model 836 ONH analyzer, shown in Figure B-71, uses a destructive method, the *inert gas fusion technique*, to analyze for elemental O, N, and H content. The specimen is melted, thus liberating the O, N, and H, which are captured in a carrier gas and moved through the LECO system for quantification. An ORNL testing protocol was developed based on the manufacturer's recommendations, and helium was chosen as the carrier gas. The standard LECO refractory metals procedure was modified slightly to reduce the generation of carbon contamination from each test. In this method, a LECO 782-720 high-temperature crucible is filled with approximately 0.050 g of graphite powder. The graphite powder is used to ensure good thermal contact between the Ni capsule and the graphite crucible when the capsule drops into the furnace. The instrument is fitted with a LECO 782-721 lower electrode tip that supplies the current to melt the specimen. Samples are placed in a LECO 502-344 nickel basket or a LECO 502-822 nickel capsule for analysis, and the remaining metallic slag is disposed of following the test.

The target cladding quadrant sample size is 0.1 g. Instrument tests confirm that variations of specimen mass within the range of the sister rod samples do not influence the results of the tests, as illustrated in Figure B-72. The measurements include hydrogen in the cladding alloy and in the waterside and pellet-side oxide layers.

Another consideration for the cladding's hydrogen measurements is the potential influence of room humidity or other sources of hydrogen contamination being introduced into the defueling/cleaning processes. To determine the potential impact, a study was performed that examined the effect of water, ethanol, and acetone exposure on the reported hydrogen in prepared standards. The standards were immersed in the liquid overnight, and then the standards were allowed to air dry. The results, shown in Figure B-73, indicate that a rigorous drying process is not necessary to achieve accurate results for the cladding samples, even at very low hydrogen content.

Before each batch of cladding specimens is tested, the system is calibrated with four standards as having a certified hydrogen content ranging from 9 to 290 ppm. Unfortunately, appropriate calibration standards beyond 290 ppm are not available; a higher hydrogen content calibration can be obtained by using multiple calibration standards for a single calibration measurement, as limited by the system's ability to completely melt the specimens. Typically, industrial users of the machine cite a measurement uncertainty based on the standard deviation of multiple samples from the same specimen, and the quadrant samples for the sister rod specimens are grouped as duplicate samples, with the standard deviation calculated from the four. However, it is known that waterside cladding oxidation and the resulting associated hydrogen content can vary azimuthally; consequently, estimating uncertainty based on the quadrant variation may be overly conservative, and based on the data in hand, the measurement uncertainty is likely ~6.5% (see further discussion in Section B-3.4). Alternatively, the estimated uncertainty can be based on the deviation of the calibration standard measurements from their certified content. The maximum relative error associated with the mass differential study, as shown in Figure B-72, is ±0.5%. The standard deviation associated with the immersion study (shown in Figure B-73) is on the order of ±4 ppm, which is as much a 33% uncertainty at the low hydrogen content (~10 ppm) of the standards used in the study. However, this high level of uncertainty is more likely associated with the lower detection limit of the machine and is not expected to carry through to the higher hydrogen samples. None of these approaches to define the uncertainty are considered particularly accurate. Given the lack of a good basis for assessing uncertainty, the standard

deviation calculated for the 4 azimuthal samples is selected as the most reasonable value pending the acquisition of additional sister rod data.

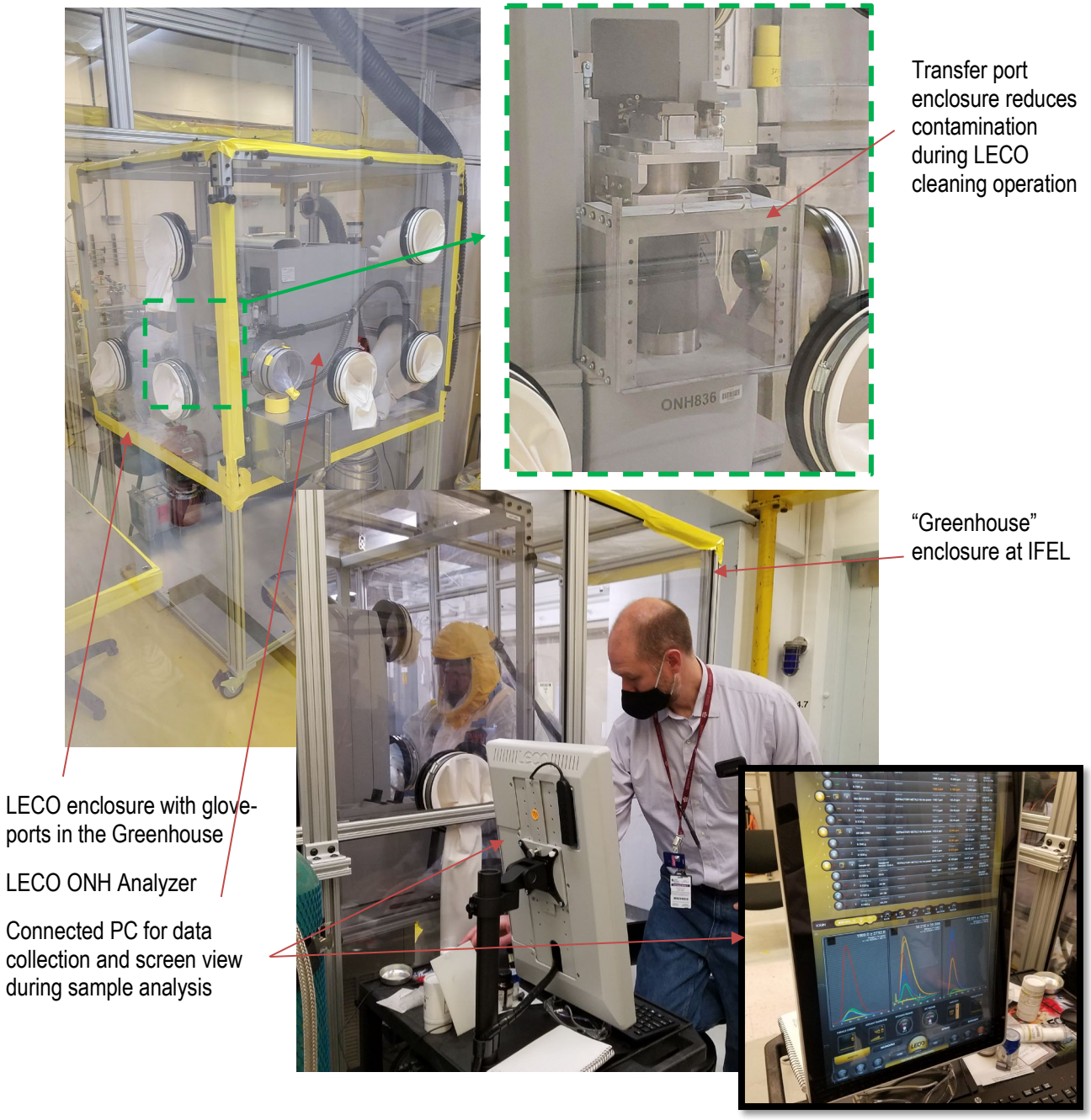

Figure B-71. (a) The LECO ONH Analyzer set up at ORNL's IFEL with (b) a view of the analysis screen.

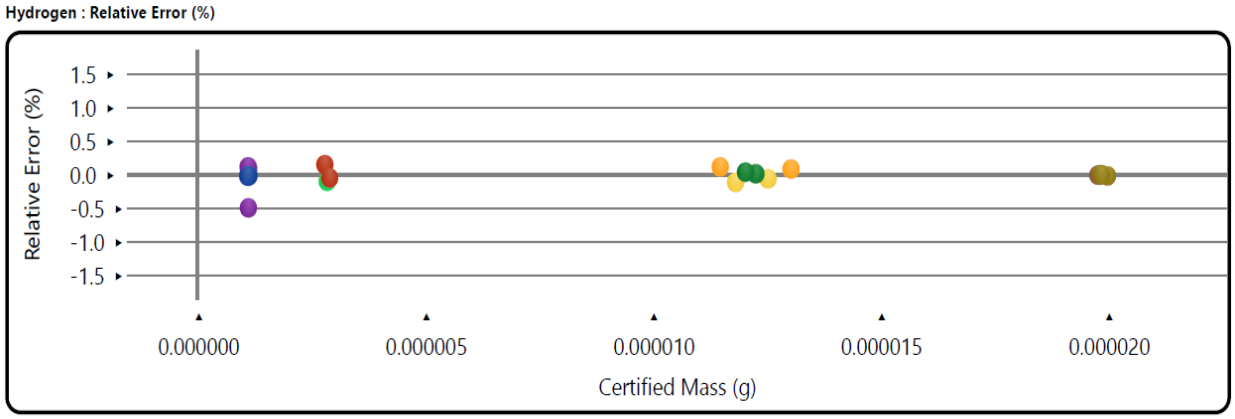

Figure B-72. Reported relative error as a function of standard mass for the calibrated LECO 836 at ORNL, as reported on 5/5/2021.

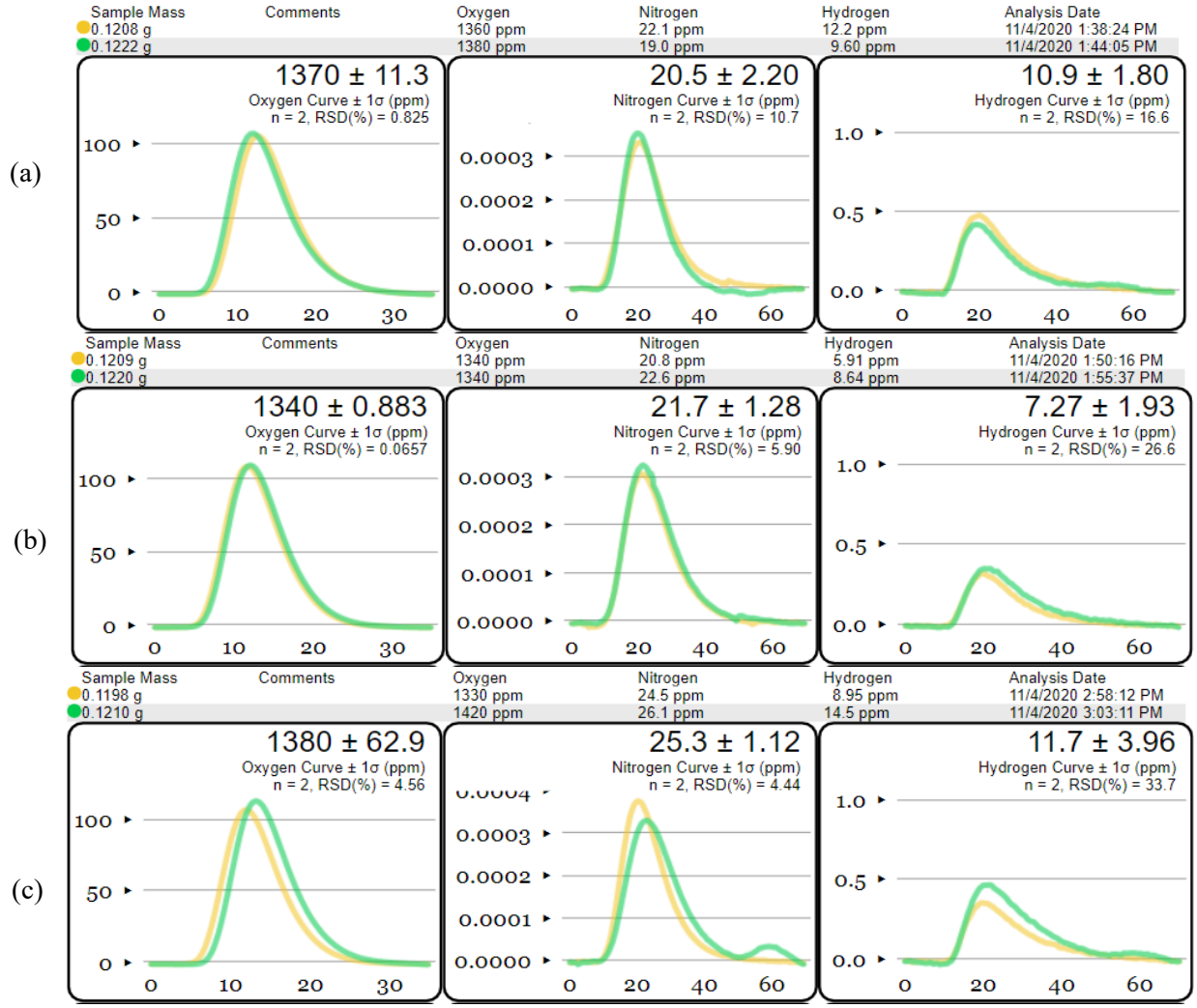

Figure B-73. Results for test standards exposed overnight to (a) water, (b) ethanol, and (c) acetone and then air dried, yielding the same results within uncertainty.

B-4.3 Measurement Results

Through August 2021, 20 segments from the phase 1 rods have been analyzed, and the average measured hydrogen content is provided in Table B-8. The specimens used for total hydrogen analysis were cut from the parent rod segment into lengths of ~4 mm and were defueled in room temperature nitric acid. Each specimen was then subsectioned into quarters, as listed in Table B-9, to provide replicate measurements at each elevation and to provide some information on the azimuthal variation in hydrogen content. Figure B-74 plots the sample mass vs. the measured hydrogen content for all samples; no trends were observed with mass, indicating there is no bias related to mass. Table B-9 provides the O and H content measured for each sample and the sample mass.

Table B-8. Average hydrogen content for samples measured to date.

Parent segment ID	Specimen ID	Cladding Alloy	Estimated local burnup (GWd/MTU)	Average measured hydrogen content (wppm)
30AD05-1280-1299	OH2	M5	59	34
30AD05-2410-2429	LH	M5	59	61
30AD05-3240-3259	AH	M5	55	142
30AE14-1677-1696	PH	M5	60	42
30AE14-2675-2699	JH2	M5	61	94
30AE14-3399-3418	BH	M5	50	152
3A1F05-1260-1279	SH	LT Zirc-4	56	130
3A1F05-1585-1604	UH	LT Zirc-4	56	278
3A1F05-2006-2025	QH	LT Zirc-4	56	572
3A1F05-2383-2402	NH	LT Zirc-4	55	680
3A1F05-2735-2754	GH	LT Zirc-4	54	1,293
3A1F05-3105-3124	EH2	LT Zirc-4	53	667
3D8E14-1375-1450 [a]	See Table B-9	ZIRLO	64	155
3D8E14-2655-2674	HH	ZIRLO	63	495
3D8E14-3206-3225	CH	ZIRLO	59	616
3F9N05-1425-1444	MH	ZIRLO	59	130
3F9N05-2863-2882	DH	ZIRLO	58	395
3F9N05-3331-3350	IH [b]	ZIRLO	51	594
F35P17-1300-1319	RH	Zirc-4	65	449
F35P17-2735-2754	FH	Zirc-4	66	870
F35P17-3050-3069	KH	Zirc-4	65	1,440

[a] This segment was identified as containing a pellet-pellet gap. After longitudinal sectioning, the exact location of the gap was revealed and specimens were cut in the gap, below the gap, and above the gap. These specimens were analyzed individually; the average is presented in this table.

[b] The specimen was low in weight and therefore was divided into two quadrants instead of four.

Table B-9. Complete listing of data collected from O and H measurements.

Segment ID	Alloy type	Specimen ID	Specimen Mass (g)	O (ppm)	H (ppm)
30AD05-3240-3259	M5	AH-0	0.1320	9,230	136
		AH-90	0.1325	8,980	132
		AH-180	0.1325	9,080	146
		AH-270	0.1204	9,340	152
30AE14-3399-3418	M5 (FHT)	BH-0	0.1401	8,590	152
		BH-90	0.1430	8,330	148
		BH-180	0.1481	8,290	143
		BH-270	0.1509	8,510	166
3D8E14-3206-3225	ZIRLO	CH-0	0.1230	21,900	678
		CH-90	0.1264	20,700	654
		CH-180	0.1375	20,400	567
		CH-270	0.1177	20,300	564
3F9N05-2863-2882	ZIRLO (FHT)	DH-0	0.1202	13,400	394
		DH-90	0.1127	15,100	403
		DH-180	0.1039	23,600	410
		DH-270	0.1090	12,800	371
3A1F05-3105-3124	LT Zirc-4	EH-0	0.1070	27,200	482
		EH-90	0.1674	19,200	531
		EH-180	specimen contaminated		
		EH-270	0.1951	20,000	989
F35P17-2735-2754	Zirc-4 (FHT)	FH-0	0.1186	31,300	1,180
		FH-90	0.1230	32,800	879
		FH-180	0.1157	32,200	590
		FH-270	0.1111	31,500	831
3A1F05-2735-2754	LT Zirc-4	GH-0	0.1253	32,700	1,390
		GH-90	0.1475	35,000	1,340
		GH-180	0.1148	39,200	1,340
		GH-270	0.1417	34,000	1,110
3D8E14-2655-2674	ZIRLO	HH-0	0.1245	14,600	363
		HH-90	0.1200	14,500	323
		HH-180	0.1276	16,600	587
		HH-270	0.1186	17,600	708
3F9N05-3331-3350	ZIRLO (FHT)	IH-0,90[a]	0.1169	16,300	629
		IH-180,270[a]	0.1397	18,000	558
30AE14-2675-2694	M5 (FHT)	JH2-0	0.0901	9,440	specimen contaminated
		JH2-90	0.0929	9,640	91
		JH2-180	0.1326	9,760	99
		JH2-270	0.0882	9,470	91
F35P17-3050-3069	Zirc-4 (FHT)	KH-0	0.1069	44,500	1,350
		KH-90	0.1189	41,300	1,450
		KH-180	0.1213	37,400	1,190
		KH-270	0.1182	46,100	1,770

Table B-8. Complete listing of O and H measurements (continued).

Segment ID	Alloy type	Specimen ID	Specimen Mass (g)	O (ppm)	H (ppm)
30AD05-2410-2429	M5	LH-0	0.1659	7,210	59
		LH-90	0.1543	7,990	58
		LH-180	0.1504	7,880	64
		LH-270	0.1796	7,420	63
3F9N05-1425-1444	ZIRLO (FHT)	MH-0	0.1128	9,970	130
		MH-90	0.1072	9,560	133
		MH-180	0.1187	9,770	128
		MH-270	0.1229	9,680	129
3A1F05-2383-2402	LT Zirc-4	NH-0	0.0678	24,000	665
		NH-90	0.0781	25,200	627
		NH-180	0.0829	23,500	469
		NH-270	0.0855	23,000	959
30AD05-1280-1299	M5	OH2-0	0.0814	8,050	33
		OH2-90	0.1552	8,110	38
		OH2-180	0.1464	7,540	30
		OH2-270	0.1722	8,270	36
30AE14-653-672	M5 (FHT)	PH-0	0.0907	6,630	27
		PH-90	0.1133	6,450	45
		PH-180	0.1021	6,620	61
		PH-270	0.0999	6,460	33
3A1F05-2006-2025	LT Zirc-4	QH-0	0.0787	20,900	803
		QH-90	0.0871	21,400	377
		QH-180	0.1004	20,300	462
		QH-270	0.0893	24,100	646
F35P17-1300-1319	Zirc-4 (FHT)	RH-0	0.0925	14,600	392
		RH-90	0.1073	16,500	301
		RH-180	0.1143	16,200	732
		RH-270	0.1135	15,000	372
3A1F05-1260-1279	LT Zirc-4	SH-0	0.0748	11,400	132
		SH-90	0.0977	11,300	134
		SH-180	0.0680	10,800	127
		SH-270	0.0701	11,400	127
3A1F05-1585-1604	LT Zirc-4	UH-0	0.1169	15,500	216
		UH-90	0.1270	14,400	439
		UH-180	0.1220	16,200	235
		UH-270	0.1312	15,300	222
3D8E14-1375-1450 [b]	ZIRLO	1396-1399	0.1126	11,000	157
		1400-1403	0.0752	15,600	216
		1403-1406 (gap)	0.1101	4,850	115
		1406-1409	0.1227	9,750	131

[a] The specimen was low in weight and therefore was divided into two quadrants instead of four.

[b] This segment was identified as containing a pellet-pellet gap. After longitudinal sectioning, the exact location of the gap was revealed and specimens were cut in the gap, below the gap, and above the gap. These specimens were analyzed individually.

B-4.4 Results Discussion

Figure B-75 plots the measured cladding hydrogen concentration as a function of the measured oxygen content and the average specimen measured hydrogen concentration as a function measured local average waterside oxide thickness [B-4], and as expected, both oxygen and waterside oxide thickness are highly correlated to the measured hydrogen concentration.

Based on an analysis of the data in Table B-9, the largest variation in hydrogen content by quadrant was observed for the Zirc-4 and LT Zirc-4 specimens, but one ZIRLO specimen (3D8E14-2655-2674) also had a large difference in waterside oxide thickness around its circumference. The best example of azimuthal hydrogen variation is from Zirc-4 Sample FH, in which the 0° sample had 1,180 ppm H, the 180° sample had 590 ppm H, and the 90 and 270° samples had H contents between these values, at 879 and 831, ppm H respectively. One cladding population (M5) has a very thin oxide layer, and there is very little azimuthal variation in the hydrogen measurements; therefore, the azimuthal variation of the M5 rods is likely fully attributable to measurement uncertainty at a magnitude of ~6.5%.

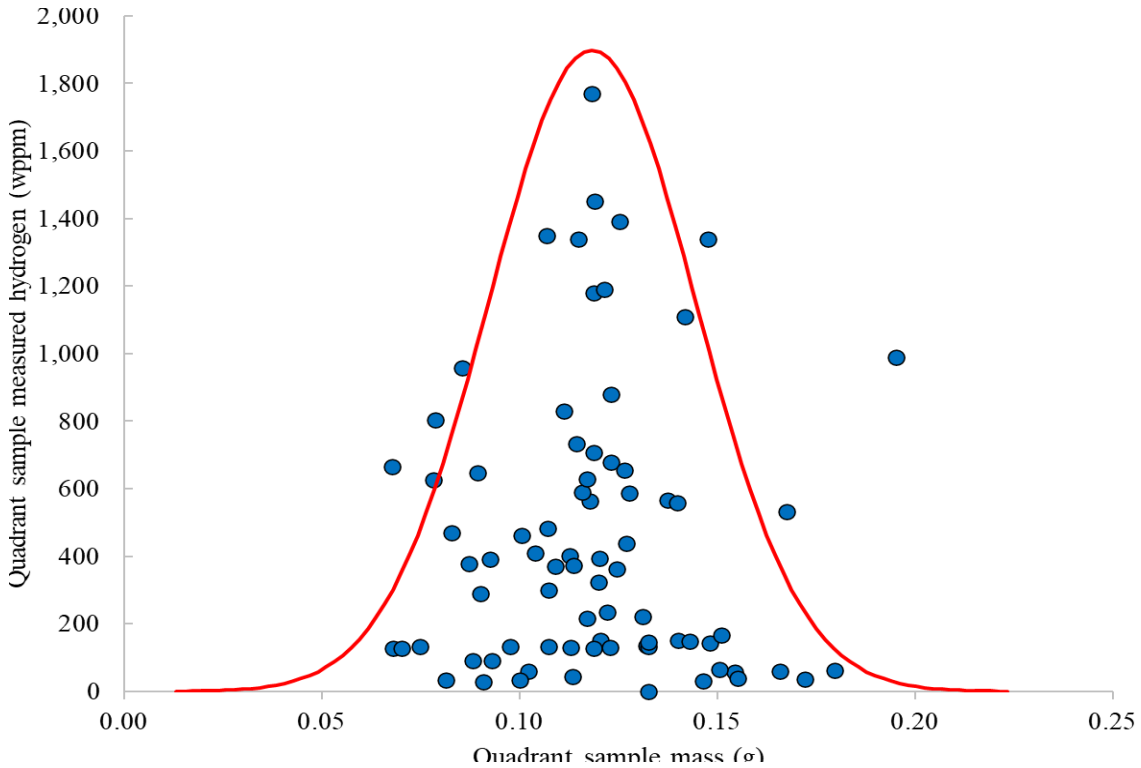

Figure B-74. Measured hydrogen as a function of specimen mass: no trends were observed.

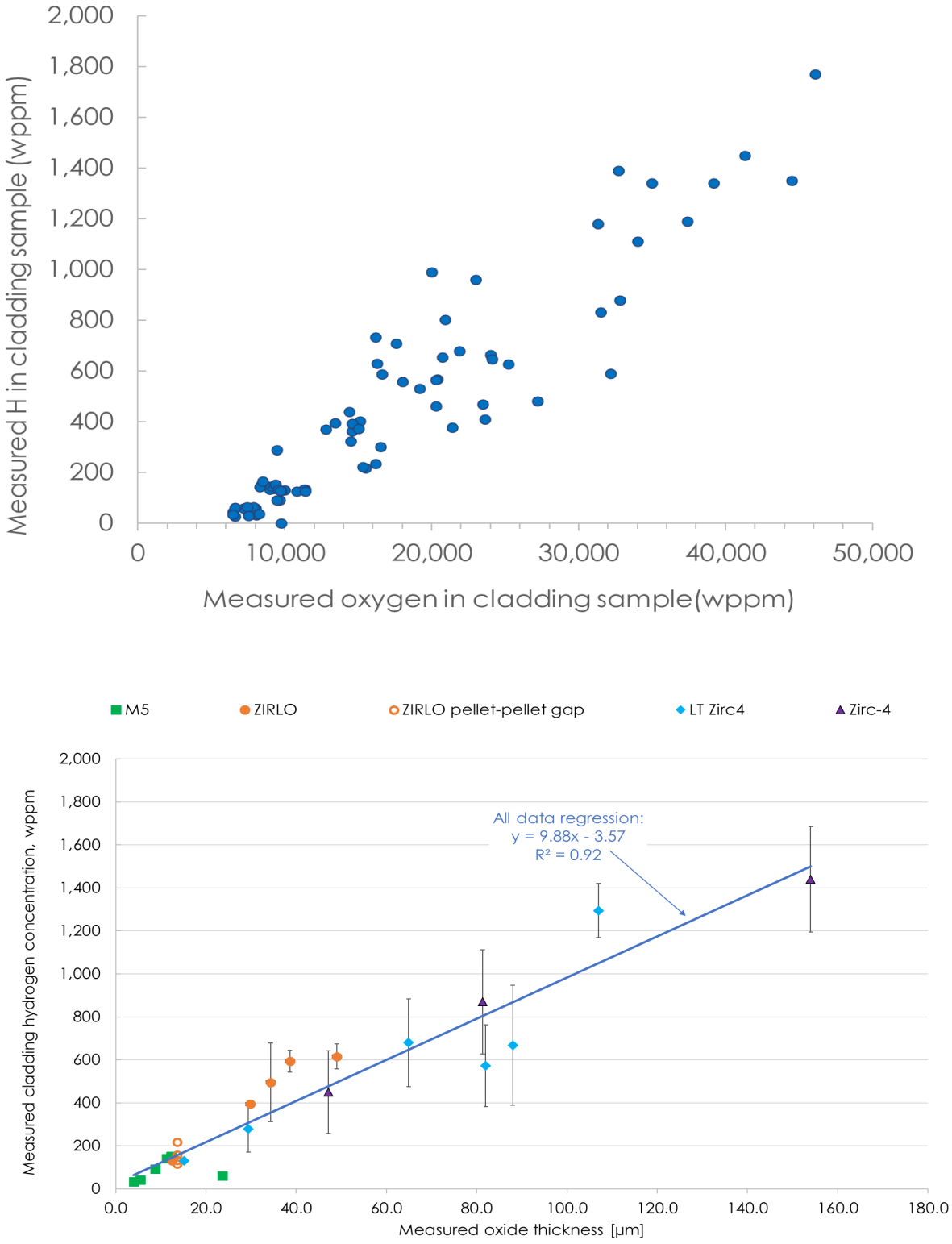

Figure B-75. Specimen measured cladding hydrogen content as a function of measured oxygen content (top) and average specimen measured cladding hydrogen as a function of measured average local waterside oxide thickness (bottom).

Figure B-76 plots the average specimen measured hydrogen concentration as a function of burnup with available previous measurements [B-7]. Except for M5, the data are higher than previously reported within the literature; however, the measured hydrogen reported includes both the metal and the oxide layers. The oxide layer includes hydrogen that was not picked up by the cladding. Figure B-77 plots the measured average cladding hydrogen measurements and the nondestructively-measured waterside oxide layer thickness [B-4] with the rod axial elevation as measured from the bottom of the rod. The relative magnitude of the measured hydrogen concentration trends well with the relative magnitude of the oxide thickness.

B-4.5 Hydrogen Pickup Fraction

The *hydrogen pickup* (HPU) is defined as the fraction of the hydrogen generated by the corrosion ($H_{generated}$) that is retained by the cladding ($H_{absorbed}$):

$$HPU = \frac{H_{absorbed}}{H_{generated}}. \quad \text{(B-1)}$$

The hydrogen is generated from the waterside oxidation of the zirconium-based cladding alloy with the coolant in reactor:

$$Zr + 2H_2O \Leftrightarrow ZrO_2 + 4H. \quad \text{(B-2)}$$

Thus, for every mole of ZrO_2 created, 4 moles of H are generated. Multiplying the molar ratio by the molar mass, 4 g H/mole H and 123.22 g ZrO_2/mole ZrO_2 = 4 g H/ 123.22 g ZrO_2, the total hydrogen generated is the product of this ratio and the mass of oxide created,

$$\frac{4\ g\ H}{123.22\ g\ ZrO_2} t_{ox}\ \rho_{ZrO2}, \quad \text{(B-3)}$$

Where t_{ox} is the measured thickness of the waterside oxide layer, and ρ_{ox} is the density of ZrO_2 (5.6 g/cc).

Given the measured hydrogen concentration in the cladding sample, H in wppm, the mass of hydrogen that was absorbed by the cladding is calculated as

$$H_{absorbed} = H(in\ wppm)\rho_{Zr} t_m, \quad \text{(B-4)}$$

where t_m is the remaining cladding wall (metal) thickness, and ρ_{Zr} is the density of zirconium (6.5 g/cc).

Combining Eqs. (B-3) and (B-4) and applying units of μm for oxide thickness, g/cc for density, and mm for remaining metal thickness, the hydrogen pickup (HPU) is

$$HPU\ (\%) = \frac{3.08\ H\ \ \rho_{Zr} t_m}{t_{ox}\ \rho_{ZrO_2}}.$$

The calculated HPU is presented in Table B-10. Because metallographic measurement results are not yet available for all specimens, several were estimated using the nondestructive measurement data of the oxide thickness and the remaining metal thickness, and typical values were applied for the pellet-side oxide layer thickness. These values will be updated as the MET measurement data become available. The uncertainty was evaluated using the same approach discussed in Appendix H, Section H-3 and Equation H-1. Using that approach, the evaluated total uncertainty of the calculated HPU is ~8% for the specimens measured and is provided in Table B-10.

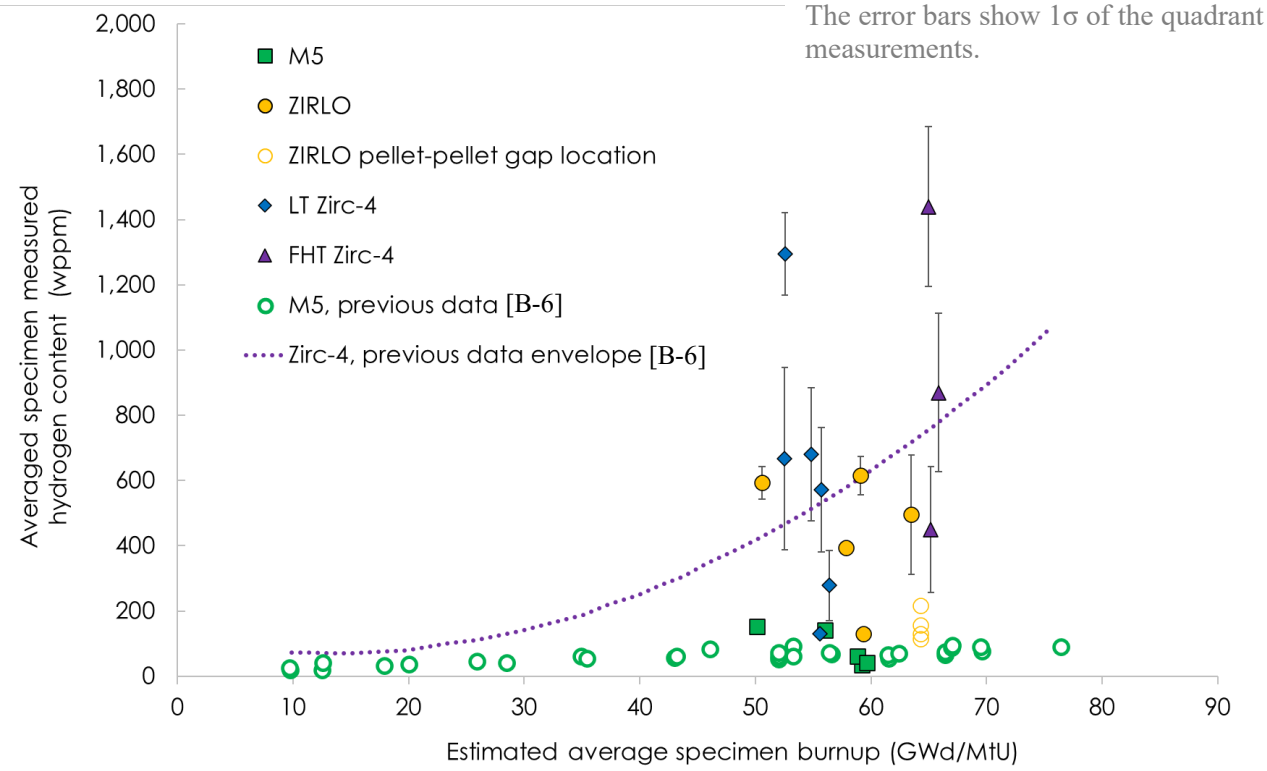

Figure B-76. Average specimen measured hydrogen content as a function of estimated local burnup by alloy and with available previous data.

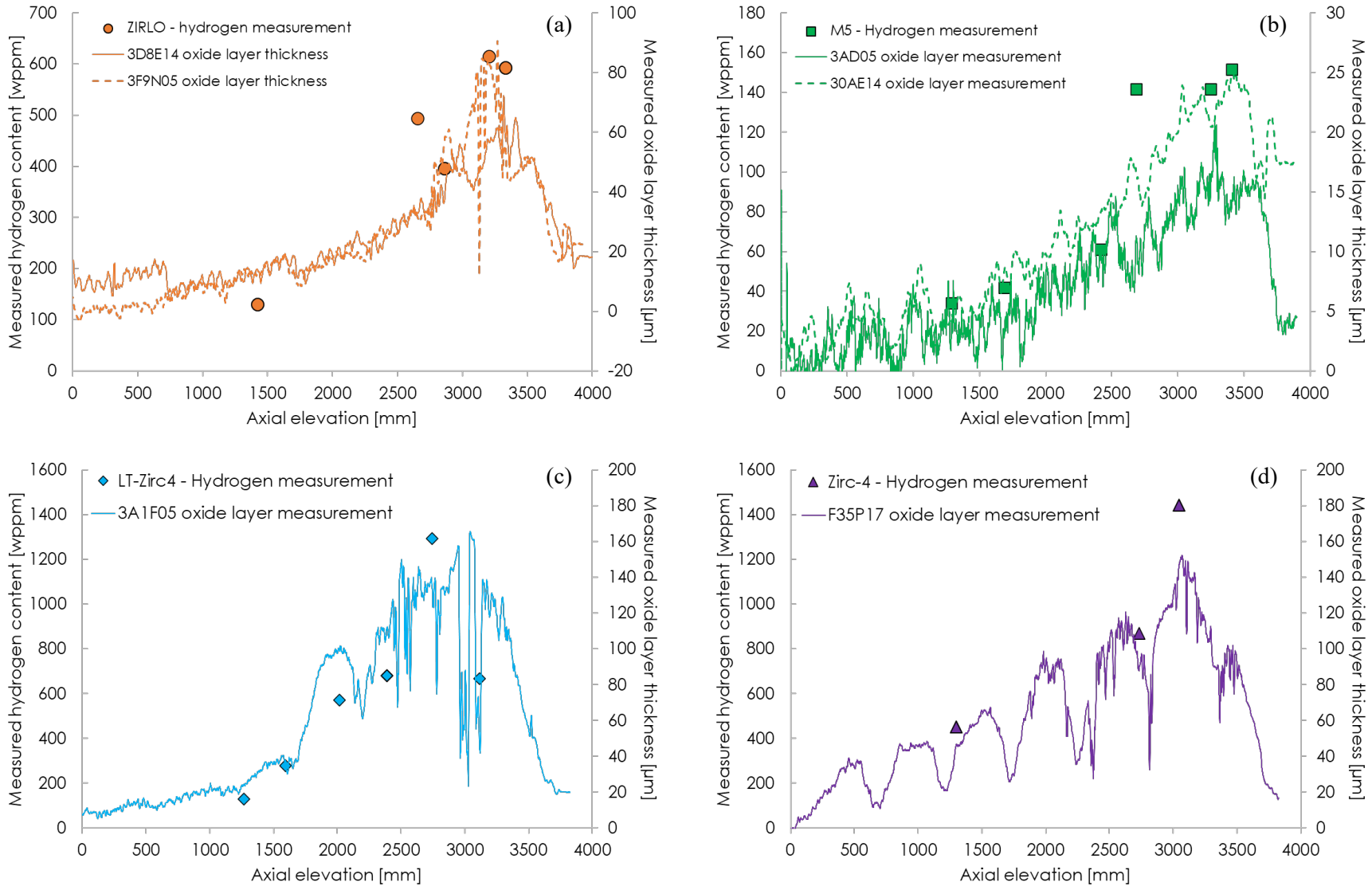

Figure B-77. Measured hydrogen content plotted with rod axial elevation and compared with nondestructively-measured oxide thickness profile [B-4] (a) ZIRLO, (b) M5, (c) LT-Zirc-4, and (d) Zirc-4.

Table B-10. Calculated %HPU based on measured cladding hydrogen concentration.

Parent segment ID	Specimen ID	Cladding Alloy	Estimated local burnup (GWd/MTU)	4-quadrant average measured oxide thickness (μm)[a]	4-quadrant average measured hydrogen content (wppm)[b]	Average HPUF (%)[c]
30AD05-1280-1299	OH2	M5	59	4	34 ± 3	16.8 ± 9.3
30AD05-2410-2429	LH	M5	59	28	61 ± 3	4.4 ± 1.7
30AD05-3240-3259	AH	M5	55	12	142 ± 9	24.3 ± 13.6
30AE14-1677-1696	PH	M5	60	6	42 ± 15	15.5 ± 9.2
30AE14-2675-2694	JH2	M5	61	9	94 ± 5	21.4 ± 2.7
30AE14-3399-3418	BH	M5	50	12	152 ± 10	24.9 ± 4.6
3D8E14-2655-2674	HH	ZIRLO	63	34	495 ± 183	23.4 ± 8.4
3D8E14-3206-3225	CH	ZIRLO	59	47 / 49[d]	616 ± 59	32.2 ± 9.7[e]
3F9N05-1425-1444	MH	ZIRLO	59	13	130 ± 2	17.1 ± 7.6
3F9N05-2863-2882	DH	ZIRLO	58	30	395 ± 17	19.5 ± 7.9
3F9N05-3331-3350	IH	ZIRLO	51	39	594 ± 50	28.3 ± 11.2
3A1F05-1260-1279	SH	LT Zirc-4	56	15	130 ± 4	24.5 ± 4.9
3A1F05-1585-1604	UH	LT Zirc-4	56	29	278 ± 108	20.9 ± 0.5
3A1F05-2006-2025	QH	LT Zirc-4	56	64	572 ± 191	26.2 ± 6.4
3A1F05-2383-2402	NH	LT Zirc-4	55	70	680 ± 204	30.4 ± 13.2
3A1F05-2735-2754	GH	LT Zirc-4	54	90 / 107[d]	1,293 ± 126	17.2 ± 2.5[e]
3A1F05-3105-3124	EH2	LT Zirc-4	53	75 / 88[d]	667 ± 280	18.6 ± 7.5[e]
F35P17-1300-1319	RH	Zirc-4	65	47	449 ± 193	16.6 ± 5.6
F35P17-2735-2754	FH	Zirc-4	66	81	870 ± 242	19.8 ± 6.4
F35P17-3050-3069	KH	Zirc-4	65	93 / 154[d]	1,440 ± 245	25.6 ± 11.9[e]
3D8E14-1375-1450[f]	1396-1399 (below gap)	ZIRLO	64	15	157 ± 10	16.5 ± 10.5
3D8E14-1375-1450[f]	1400-1403 (below gap)	ZIRLO	64	14	216 ± 14	18.4 ± 11.3
3D8E14-1375-1450[f]	1403-1406 (gap)	ZIRLO	64	12	115 ± 7	20.0 ± 5.8
3D8E14-1375-1450[f]	1406-1409 (above gap)	ZIRLO	64	15	131 ± 9	26.8 ± 24.2

a. See Section B-3 for more information on the oxide thickness measurements and variance.

b. The uncertainty shown is the standard deviation of the 4 quadrant measurements as discussed in Section B-4.2 and may reflect expected variations in oxidation and hydrogen content around the circumference of the fuel rod.

c. The average HPUF is based on the average remaining cladding wall thickness and the average measured waterside oxide layer thickness, excluding measurements of spalled or peeled regions of the oxide. The uncertainty shown is based on the uncertainty of the parameters used in the average HPUF calculation. See Appendix H, Section H-3 for the uncertainty calculational approach.

d. Average / average excluding measurements where spalling occurred.

e. Calculation of the HPUF is based upon the average measurement of waterside oxide layer excluding spalled or peeled regions of the oxide.

f. This segment was identified as containing a pellet-pellet gap. After longitudinal sectioning, the exact location of the gap was revealed and specimens were cut in the gap (1,403 to 1,406 mm in elevation from rod bottom), below the gap (1,396 to 1,403 mm in elevation), and above the gap (1,406 to 1,409 mm in elevation). These specimens were analyzed individually. Specimens above and below the gap were in contact with a pellet during operation, while the gap region was not. The uncertainty of the hydrogen content measurement is assessed as the standard deviation of the measurements at the 4 elevations.

The measurements of the hydrogen concentration reported in Table B-8 and used to calculate the HPU include hydrogen within the waterside oxide layer in addition to the hydrogen in the metal; therefore, the hydrogen pickup of the alloy is overestimated. However, Eq. (B-3) assumes that the oxide layer is 100% dense monoclinic oxide. As the oxide layer grows, its density decreases to about 90%, mainly due to cracking; Eq. (B-3) tends to overestimate the amount of oxidation and corresponding available hydrogen, thus underestimating the actual hydrogen pickup. These effects offset each other, and direct measurement of the oxide layer density and hydrogen content are impractical. Although the difference is likely small, in future, the calculation may be repeated using the measured oxygen content (as corrected for oxygen in the as-fabricated cladding) as an additional point for comparison.

The HPU is plotted with oxide thickness in Figure B-78, with the specimen elevation on the rod in Figure B-79, and with estimated local burnup in Figure B-80. A strong trend is not evident for any of these parameters, which is not surprising, because hydrogen pickup is generally regarded as an alloy-dependent phenomenon that is more dependent on alloying elements, microstructure, and microchemistry as influenced by operating conditions (time at temperature).

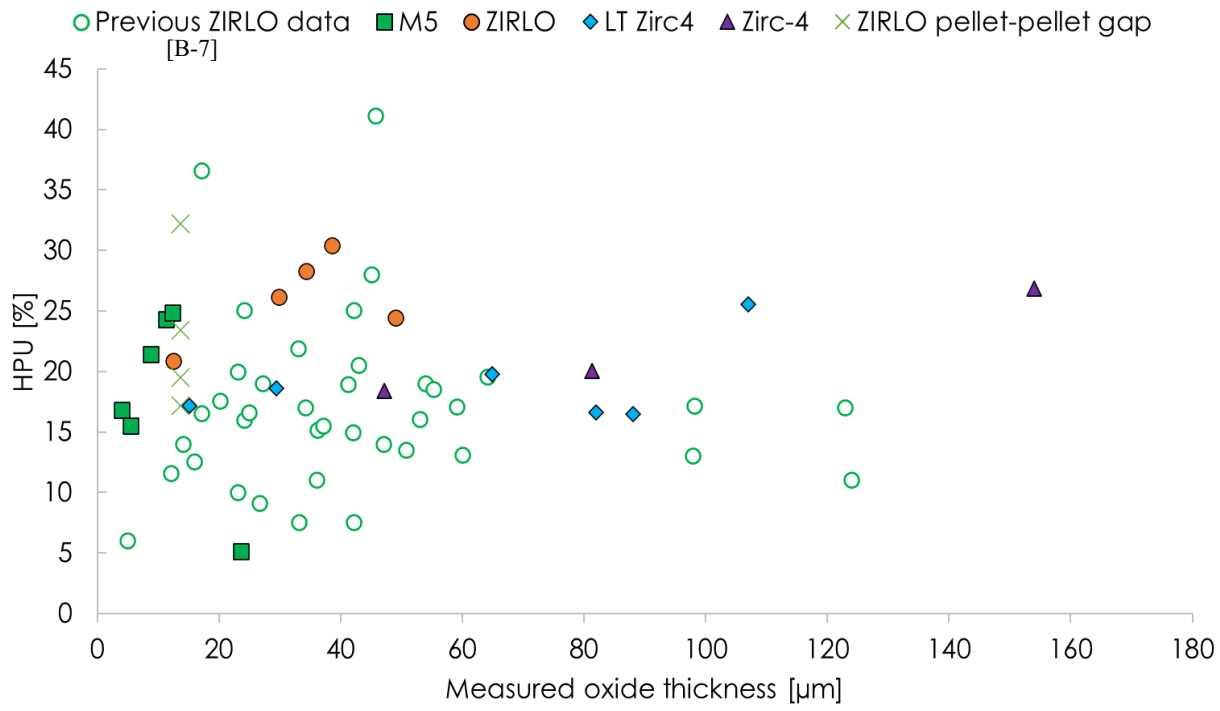

Figure B-78. HPU as a function of local measured oxide thickness, including publicly available data for ZIRLO [B-7].

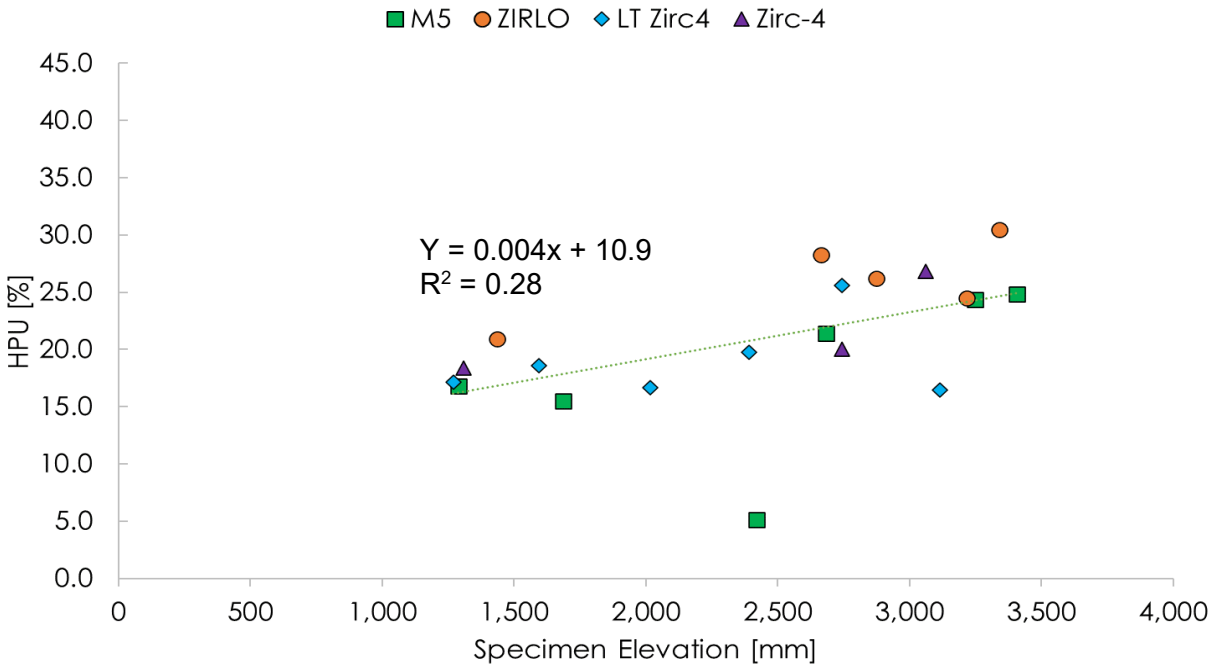

Figure B-79. HPU as a function of specimen elevation on the fuel rod (multiple rods represented).

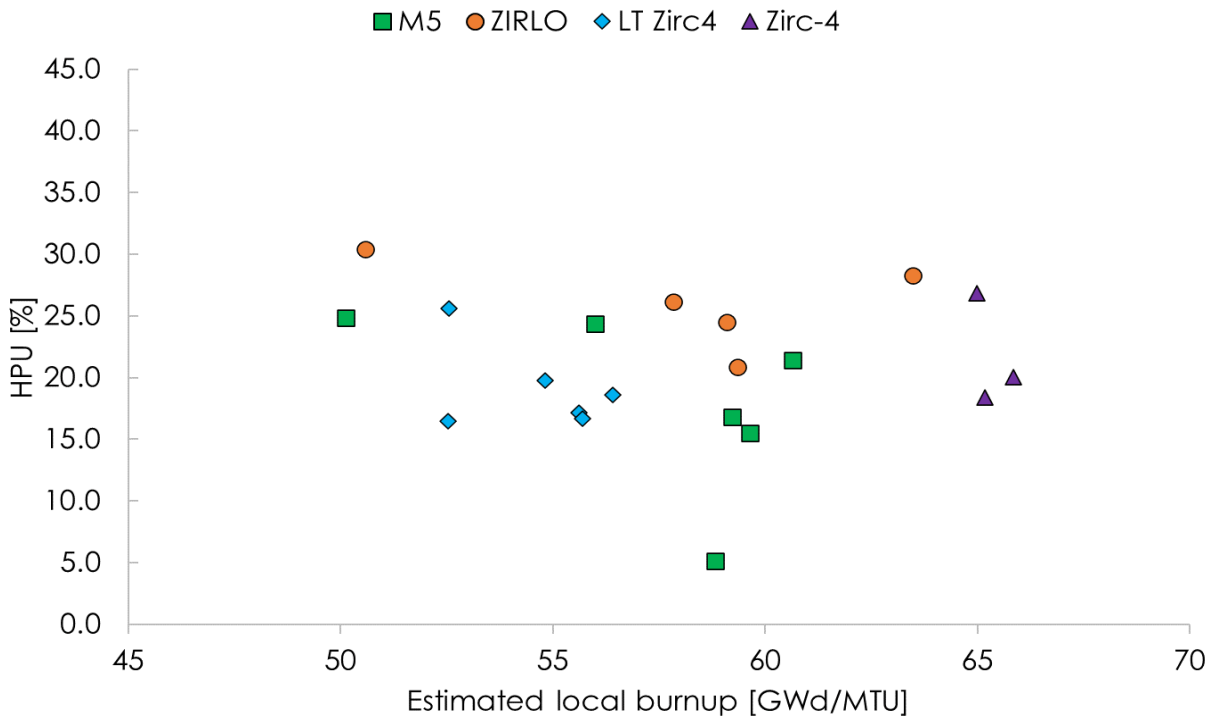

Figure B-80. HPU as a function of estimated local burnup.

REFERENCES

[B-1.] *High Burnup Dry Storage Cask Research and Development Project: Final Test Plan*, Contract No. DE-NE-0000593, Electric Power Research Institute, Palo Alto, California (2014).

[B-2.] Saltzstein, Sylvia et al., *Visualization of the High Burnup Spent Fuel Rod Phase 1 Test Plan*, SAND2018-8042-O (2018).

[B-3.] Montgomery, R. A. et al., *Post-Irradiation Examination Plan for High Burnup Demonstration Project Sister Rods*, SFWD-SFWST-2017-000090 ORNL/SR-2016/708, Oak Ridge National Laboratory (2016).

[B-4.] Montgomery, R. A. et al., *Sister Rod Nondestructive Examination Final Report*, SFWD-SFWST-2017-000003 Rev. 1 (M2SF-17OR010201021) / ORNL/SPR-2017/484 Rev. 1 (ORNL/SPR-2018/801), Oak Ridge National Laboratory (2019).

[B-5.] Balfour, M. G. et al. *Corrosion of Zircaloy-Clad Fuel Rods in High-Temperature PWRs: Measurement of Waterside Corrosion in North Anna Unit 1, Interim Report, March 1992*, prepared by Westinghouse Electric Corporation for Electric Power Research Institute, TR-1004008, Tier 2 Research Project 2757-1, 1992.

[B-6.] Cole, S. E. C. Delafoy, R.F. Graebert, P-H. Louf, and N. Teboul. "AREVA Optimized Fuel Rods for LWRs," *TopFuel 2012*.

[B-7.] Garde A.M., Slagle W.H., Mitchell D.B., "Hydrogen Pick-Up Fraction for ZIRLO™ Cladding Corrosion and Resulting Impact on the Cladding Integrity," Paper 2136, *Proceedings of Top Fuel 2009* Paris, France, September 6–10, 2009.

[B-8.] M.C. Billone, Ductility of High-Burnup-Fuel ZIRLO™ Following Drying and Storage, ANL-19/14, M2SF-19AN010201011 Rev. 3, Argonne National Laboratory, June 2019.

[B-9.] M.C. Billone, T. A. Burtseva, and M. A. Martin-Rengel. Effects of Lower Drying -Storage Temperatures on the DBTT of High-Burnup PWR Cladding, Argonne National Laboratory, FCRD-UFD-2015-000008, 2015.

[B-10.] Kese, Kwadwo, Hydride Re-Orientation in Zircaloy and Its Effect on the Tensile Properties (Revised Edition), Royal Institute of Technology, Stockholm, Sweden, SKI report 98:32, 1998.

[B-11.] Billone, M. C., et al., Phase I Ring Compression Testing of High-Burnup Cladding, Argonne National Laboratory, FCRD-USED-2012-000039, 2012.

[B-12.] Billone, M. C., T. A. Burtseva and R. E. Einzinger, Ductile-to-Brittle Transition Temperature for High-Burnup Cladding Alloys Exposed to Simulated Drying-Storage Conditions, Journal of Nuclear Materials, Vol. 433, pp. 431-448, 2013.

[B-13.] Billone, Michael C., Tatiana A. Burtseva, and Yung Y. Liu, Characterization and Effects of Hydrides in High-Burnup PWR Cladding Alloys, International High Level Radioactive Waste Conference Proceedings, American Nuclear Society, Charlotte, NC, 2015.

[B-14.] Burtseva, T. A., Y. Yan, and M. C. Billone, Radial-Hydride-Induced Embrittlement of High-Burnup ZIRLO Cladding Exposed to Simulated Drying Conditions, 2010.

[B-15.] Billone, M. C., et al., Effects of Multiple Drying Cycles on High-Burnup PWR Cladding Alloys, FCRD-UFD-2014-000052 ANL-14/11, Argonne National Laboratory, 2014.

[B-16.] Schindelin, J., Arganda-Carreras, I., Frise, E., Kaynig, V., Longair, M., Pietzsch, T., Cardona, A. (2012). Fiji: an open-source platform for biological-image analysis. Nature Methods, 9(7), 676–682. doi:10.1038/nmeth.2019

[B-17.] Arganda-Carreras, I., Kaynig, V., Rueden, C., Eliceiri, K. W., Schindelin, J., Cardona, A., & Sebastian Seung, H. (2017). Trainable Weka Segmentation: a machine learning tool for microscopy pixel classification. Bioinformatics, 33(15), 2424–2426. doi:10.1093/bioinformatics/btx180

[B-18.] Eibe Frank, Mark A. Hall, and Ian H. Witten (2016). The WEKA Workbench. Online Appendix for "Data Mining: Practical Machine Learning Tools and Techniques", Morgan Kaufmann, Fourth Edition, 2016. https://books.google.com/books?id=4-FZuwEACAAJ